INVESTIGATION OF DYNAMIC SUBGRID-SCALE AND WALL MODELS FOR TURBULENT BOUNDARY LAYERS

A DISSERTATION
SUBMITTED TO THE INSTITUTE FOR COMPUTATIONAL AND
MATHEMATICAL ENGINEERING
AND THE COMMITTEE ON GRADUATE STUDIES
OF STANFORD UNIVERSITY
IN PARTIAL FULFILLMENT OF THE REQUIREMENTS
FOR THE DEGREE OF
DOCTOR OF PHILOSOPHY

Hyunji Jane Bae

September 2019

I certify that I have read this dissertation and that, in my opinion, it is fully adequate in scope and quality as a dissertation for the degree of Doctor of Philosophy.

(Parviz Moin) Principal Adviser

I certify that I have read this dissertation and that, in my opinion, it is fully adequate in scope and quality as a dissertation for the degree of Doctor of Philosophy.

(Sanjiva K. Lele)

I certify that I have read this dissertation and that, in my opinion, it is fully adequate in scope and quality as a dissertation for the degree of Doctor of Philosophy.

(Sanjeeb T. Bose)

Approved for the Stanford University Committee on Graduate Studies

Abstract

Most turbulent flows cannot be calculated by direct numerical simulation (DNS) of the Navier-Stokes equations because the range of scales of motions is so large that the computational cost becomes prohibitive. In large-eddy simulation (LES), only the large eddies are resolved and the effect of the small scales on the larger ones is modeled through a subgrid-scale (SGS) model. Given that accurate representation and prediction of turbulence is needed in many engineering and scientific applications, development of accurate yet computationally efficient SGS models is an important task. Additionally, wall models are necessary to overcome the prohibitive near-wall resolution requirements for the large scales in high-Reynolds-number turbulent flows.

This study investigates a new SGS model, the anisotropic minimum-dissipation (AMD) model, which is constructed to provide the minimum eddy viscosity required to avoid energy pile-up in the smallest resolved scales. The AMD model is successfully applied in simulations of decaying grid turbulence for isotropic grids, and temporal mixing layer and turbulent channel flow for anisotropic grids. This model is more cost-effective than the dynamic Smagorinsky model (DSM) and appropriately switches off in laminar and transitional flows. The formulation of the AMD model is extended to the transport equation for scalar concentration to model the subfilter scalar flux. The performance of the model is tested in the simulation of high-Reynolds-number rough-wall boundary-layer flow with a constant and uniform surface scalar flux. The simulation results obtained from the scalar model show good agreement with well-established empirical correlations and theoretical predictions of the resolved flow statistics.

The accuracy of the SGS models is tested by studying the convergence properties in the outer region of a channel flow at moderate to high Reynolds numbers. As LES requires scale separation of the resolved and subgrid scales, the convergence study must be conducted in high-Reynolds-number flows. However, the analysis shows that the errors from the near-wall region are dominant for SGS models in usual LES grid resolutions, where the grid is not refined in the wall-parallel directions. For evaluation of SGS models, in order to overcome the grid requirements imposed by the near-wall turbulent eddies as well as the errors accumulated near the wall, a possible solution is to isolate the outer region of wall-bounded flows. This is made possible by one of two ways: suppressing the near-wall dynamics through a modified wall, or supplying the correct mean stress at the wall with a wall model. Theoretical analysis of the error scaling of SGS models for the mean velocity profile, turbulence intensities, and energy spectra is performed. The numerical convergence studies of the DSM and AMD models show that both models are first-order accurate in terms of the mean velocity profile, which is consistent with the theoretical assessments.

Lastly, a new dynamic wall model based on the slip boundary condition is proposed. The use of the slip boundary condition for wall-modeled LES is motivated through theoretical analysis and *a priori* study of DNS data. The effect of the slip boundary condition on the one-point statistics of the flow is investigated in LES of turbulent channel and flat-plate turbulent boundary layer. The slip boundary condition provides a framework to compensate for the deficit or excess of mean momentum at the wall. The requirements for the slip lengths to be used in conjunction with wall models are discussed, and the equation that connects the slip boundary condition with the stress at the wall is derived. A dynamic procedure based on the invariance of wall stress under test filtering is formulated for the slip condition, providing a dynamic slip wall model free of any *a priori* specified coefficients. The performance of the proposed dynamic wall model is tested in a series of LES of turbulent channel flow at varying Reynolds numbers, non-equilibrium three-dimensional transient channel flow, and zero-pressure-gradient flat-plate turbulent boundary layer. The results show that the dynamic wall model is able to accurately predict mean and turbulence intensities for various flow configurations, Reynolds numbers, and grid resolutions.

Acknowledgments

First of all, I would like to thank my advisor, Prof. Parviz Moin for his encouragement and inspiration throughout my graduate studies. He taught me how to ask the right questions and to focus on the bigger picture, which is a lesson I will cherish as an academic. I am also grateful to my committee members, Prof. Sanjiva Lele and Dr. Sanjeeb Bose for their helpful comments and discussions on this dissertation. I would especially like to acknowledge Dr. Sanjeeb Bose for the invaluable feedback regarding dynamic wall modeling, among other topics.

This work would not have been possible without the help from many collaborators and colleagues who have assisted me with each step of my research. I am deeply indebted to Dr. Adrián Lozano-Durán, from whom I take away many lessons including his work ethic. His knowledge of the fundamental physics of turbulent flows was instrumental in my understanding of the topic. I would also like to thank Prof. Verstappen and Drs. Wybe Rozema and Maurits Silvis for their collaboration on the development and analysis of subgrid-scale models during and after the Center for Turbulence Research Summer Program. I am grateful to Dr. Mahdi Abkar for introducing me to the topic of atmospheric boundary layers and scalar modeling. I also would like to acknowledge the camaraderie of the Moin group members, both past and present (George Park, Ik Jang, Chris Ivey, Jeff O'Brien, Curtis Hamman, Maxime Bassenne, Ron Chan, Connor Hwang, Shaun Harris, Kevin Griffin, Suhas Jain, and Tim Flint).

I am grateful to my family, my parents Chong Ok and Hyung, and my little brother Hyungkwon, for their emotional support. I would also like to thank all my friends that have

stuck by my side during this journey. This work would not have been the same without their unwavering encouragement and moral support.

Finally, I would like to thank the generous financial support from the Stanford Graduate Fellowship and the National Aeronautics and Space Administration.

Nomenclature

Acronyms

AMD	Anisotropic minimum-dissipation
DES	Detached eddy simulation
DNS	Direct numerical simulation
DSM	Dynamic Smagorinsky model
EQWM	Equilibrium wall model
EWS	Exact wall stress
LES	Large-eddy simulation
MD	Minimum-dissipation
NE	Neumann boundary condition
NEQWM	Non-equilibrium wall model
NM	No (subgrid-scale) model
NS	No-slip
PDE	Partial differential equation
PDF	Probability density function

RANS	Reynolds-averaged Navier-Stokes
rms	Root-mean-square
SGS	Subgrid scale
SL	Slip boundary condition
SLW	Slip-wall
SM	Smagorinsky model
TBLE	Thin boundary layer equations
WSIM	Wall-stress invariant model

Mathematical operators

$(\cdot)'$	Fluctuating values of $(\cdot)$
$(\cdot)\|_w$	Values of $(\cdot)$ evaluated at the wall
$(\cdot)^*$	Complex conjugate of $(\cdot)$
$(\cdot)^+$	Variable in wall-units, normalized using u_τ and ν
$\bar{(\cdot)}$	Grid resolved values of $(\cdot)$
$\hat{(\cdot)}$	Fourier transformed values of $(\cdot)$
$\langle(\cdot)\rangle$	Average value of $(\cdot)$ in homogeneous spatial directions and, if flow is stationary, in time
$\langle(\cdot)\rangle_t$	Average value of $(\cdot)$ in time
$\langle(\cdot)\rangle_w$	Average value of $(\cdot)$ along the wall
$\mathbb{R}[(\cdot)]$	Real part of $(\cdot)$
$\mathcal{F}^{-1}(\cdot)$	Inverse Fourier transformed values of $(\cdot)$

$\tilde{(\cdot)}$	Explicit or test filtered values of $(\cdot)$
$\partial_s(\cdot)/\partial x_i$	Scaled differentiation operator on $(\cdot)$ in the x_i direction

Greek symbols

α_f	Turbulence intensity error scaling exponent for grid resolution
α_m	Mean velocity profile error scaling exponent for grid resolution
α_s	Kinetic energy spectra error scaling exponent for grid resolution
β	Power law constant
γ	Heat capacity ratio
γ_f	Turbulence intensity error scaling exponent for Reynolds number
γ_m	Mean velocity profile error scaling exponent for Reynolds number
γ_s	Kinetic energy spectra error scaling exponent for Reynolds number
δ	Boundary layer thickness or channel half height
Δ	Grid size
$\tilde{\Delta}$	Second moment of the filter operator
Δ_i	Grid size along the x_i direction
$\tilde{\Delta}_i$	Second moment of the filter operator along the x_i direction
δ_{ij}	Kronecker delta
Δ_R	Ratio of test filter size to grid filter size
Δ_t	Time step
ϵ	Error

ε	Dissipation rate
ε_τ	Subfilter dissipation rate
ε_{SGS}	Subgrid-scale dissipation rate
η	Kolmogorov scale
θ	Momentum thickness
θ_0	Momentum thickness at inlet
θ_{avg}	Average momentum thickness
κ	von Kármán constant
λ_i	Wavelength in the x_i direction
ν	Kinematic viscosity
ν_e	Eddy viscosity
Π	Pressure diffusion
ρ	Fluid density
ς	Subgrid-scale activity parameter
τ_w	Wall shear stress
τ_{ij}	Exact subgrid-scale stress tensor
τ_{ij}^{SGS}	Modeled subgrid-scale stress tensor
ϕ	Scalar concentration
ϕ_*	Surface potential scalar
Φ_ϕ	Averaged scalar concentration gradient

Φ_M	Averaged streamwise velocity gradient
Ω_Δ	Box filter domain

Roman symbols

A_i, B_i	Logarithmic law constants for $u_i'^2$ for turbulent channel flow
B	Intercept constant for the logarithmic law
C	Anisotropic minimum-dissipation model constant
C_Δ	Poincaré constant
$\tilde{C}_\Delta$	Modified Poincaré constant
C_f	Friction coefficient
C_i	Anisotropic minimum-dissipation model constant in the x_i direction
C_s	Smagorinsky coefficient
D	Scalar diffusivity
D_e	Eddy diffusivity
E_ϕ	Spectral density of the scalar concentration
E_i	Spectral density of the velocity u_i
E_K	Spectral density of the turbulent kinetic energy
G	Isotropic velocity gradient
H	Wall-normal height of the computational domain for high-Reynolds-number boundary layer flow
II	Second invariant of the rate-of-strain tensor
III	Third invariant of the rate-of-strain tensor

k, k_i	Wavenumber
$\tilde{k}, \tilde{k}_i$	Modified wavenumber
K	Turbulent kinetic energy
K_{res}	Ratio of resolved turbulent kinetic energy
k_p	$(k_1^2 + k_3^2)^{1/2}$
l, l_i	Slip lengths
$\tilde{l}$	Slip length at test filter level
L_ε	Integral length-scale
L_λ	Taylor micro-scale
L_i	Length of computational domain in the x_i direction
L_s	Shear length-scale
M	Mesh size for the decaying isotropic turbulence experiment by Comte-Bellot and Corrsin
$M_{\mathcal{G}}^{(m)}$	The m-th moment of the filter kernel $\mathcal{G}$
Ma	Mach number
n	Wall-normal direction
N	Number of grid points
N_i	Number of grid points in the x_i direction
p	Pressure field
Q	Mass flux
Q_*	Surface scalar flux

q_i	Subgrid scalar flux
R_{ij}	Reynolds stress tensor
Re	Reynolds number
Re_θ	Reynolds number based on momentum thickness
Re_τ	Reynolds number based on friction velocity
Re_b	Reynolds number based on bulk velocity
S_{ij}	Rate-of-strain tensor
Sc_e	Subgrid Schmidt number
t	Time
t_c	Characteristic time
T_{ij}	Subgrid-scale stress at test filter level
$\mathbf{u}$	Velocity vector
U_0	Mean velocity for the decaying isotropic turbulence experiment by Comte-Bellot and Corrsin
u_τ,u_*	Friction velocity
u_b	Bulk velocity
u_i	Velocity component in the x_i direction
U_∞	Free-stream streamwise convective velocity
V	Volume of computational domain
v_i	Slip velocities
x_i	Position vector

x_o	Aerodynamics surface roughness
x_{ref}	Reference downstream plan for inlet recycling scheme

Other symbols

$\mathcal{D}$	Viscous diffusion
$\mathcal{D}_\tau$	Subfilter turbulent transport
$\mathcal{D}_{\text{SGS}}$	Subgrid turbulent transport
$\mathcal{E}_f, \mathcal{E}_{f,i}$	Error in the turbulence intensities
$\mathcal{E}_{K,l}$	Local error in the turbulent kinetic energy
$\mathcal{E}_m$	Error in the mean velocity profile
$\mathcal{E}_{m,l}$	Local error in the mean velocity profile
$\mathcal{E}_s$	Error in the kinetic energy spectra
$\mathcal{G}, \mathcal{G}^*$	Filter kernel
$\mathcal{P}$	Production rate of the turbulent kinetic energy
$\mathcal{T}$	Turbulent transport
$\mathcal{T}_{ij}^k$	Wall stress tensor at different filter levels

Contents

List of Tables

List of Figures

Chapter 1

Introduction

Wall-bounded turbulence is ubiquitous in both scientific research and industrial applications. The presence of a wall introduces additional length scales that impart further complexity to turbulent motions that already exhibit a large range of scales and non-linear dynamics. This produces further challenges in the fundamental understanding and modeling of wall-bounded turbulence, which has been the subject of many reviews and monographs for decades [64, 158, 160, 131, 125, 112, 51].

Prediction of turbulent flows based on first principles can be accomplished by using direct numerical simulation (DNS), in which the Navier-Stokes equations are solved numerically on a grid that resolves the smallest dissipative eddies. DNS has no modeling assumptions other than the commonly accepted continuum hypothesis and the constitutive equations or the viscous stress tensor. However, for simulations of practical flows at high Reynolds numbers, the grid resolution required to resolve the large scale-separation is excessive for current state-of-the-art computers, even without the additional complexity of a wall [132].

As a result, large-eddy simulation (LES) has emerged as a viable high-fidelity tool for computational fluid dynamics. In LES, the large eddies containing most of the turbulent energy are directly resolved while the effect of the small scales on the larger ones is modeled through a subgrid-scale (SGS) model. Hence, the approach enables a reduction of the computational cost by several orders of magnitude when compared with DNS [25, 26].

Accurate predictions of the statistical quantities of interest require development of accurate yet computationally efficient SGS models. Moreover, for LES to be used as a predictive tool, the parameters involved in the SGS model should not rely on *a priori* tunable coefficients. In SGS modeling, this has been addressed with the use of the dynamic procedure [42, 106].

Although the use of SGS models improves the computational efficiency in the outer region, in the near-wall region, the energy-containing eddies become small compared to the physical dimensions of the flow device, causing the near-wall grid requirement to become computationally prohibitive [25, 147, 26]. In wall-resolved LES, where the grid must be refined in all spatial directions, over 90% of the grid points are used to capture an inner-layer whose thickness is less than 10% of the boundary layer [120]. Additionally, commonly used SGS models are not equipped to represent the stress producing near-wall structures and are known to be deficient in the near-wall region [54]. This calls for reduced order modeling of the near-wall region. Wall modeling is intended to relax the near-wall grid requirements and to compensate for the shortcomings of SGS models in the near-wall region by supplying accurate predictions of the wall stress.

There have been many wall-modeling attempts in LES, starting with the channel flow simulations by Deardorff [34]. Schumann [139] used an algebraic relation between the wall shear stress and the LES velocity based on the law-of-the-wall. Piomelli et al. [123] modified the model by taking into account the inclination angle of vortical structures in the near-wall region. Balaras et al. [10] modeled the near-wall region by the thin boundary layer equations (TBLE). The wall-model, in this case, is no longer a simple algebraic relation, and the wall stress is obtained by solving simplified Navier-Stokes equations defined on an embedded layer in the vicinity of the wall. Typically, the TBLE is solved with a Reynolds-averaged Navier-Stokes (RANS) mixing-length model [10, 19, 171, 29, 61, 113]. Other methods for wall-modeling include the detached-eddy simulation (DES) [149] and hybrid LES/RANS variants that combine RANS and LES equations with the interface enforced implicitly through a change in the turbulence model. However, an important limitation of the models above is that they depend on pre-computed parameters from the RANS model and/or assume explicitly or implicitly a particular law for the mean velocity profile close to

the wall. The shortcomings of current models call for development of new dynamic models that do not depend on *a priori* tunable parameters.

In addition, an important aspect of developing models is to assess their performance. In particular, due to the intimate relationship between the grid resolution and the LES equations, it is necessary to characterize the errors as a function of grid resolution and Reynolds number. There have been efforts to assess the accuracy of SGS models in numerical studies of isotropic turbulence [32, 94, 97], rotating homogeneous turbulence [65], and spatial or temporal mixing layers [167, 168], as well as low-Reynolds-number plane channel flows [122, 42, 28]. However, due to the grid resolution requirement of the near-wall region, there is limited literature on the effectiveness of SGS models in high-Reynolds-number turbulent boundary layers. Developing benchmark cases where the errors of SGS models can be quantified for high-Reynolds-number turbulent boundary layers without the prohibitive near-wall grid resolution is necessary to evaluate the SGS model separately from the errors due to the missing structures near the wall.

The following three chapters explore the above topics. In Chapter 2, a new SGS model based on the minimum dissipation requirement of the smallest resolved scales is introduced. These models are accurate, computationally efficient, and are evaluated locally without the necessity of *ad hoc* measures for stability. Chapter 3 provides two novel benchmark cases to test the performance of SGS models without error contamination from the unresolved turbulence near the walls. This allows for assessment of SGS models in high-Reynolds-number wall-bounded flows in the outer region without the grid resolution requirement of typical wall-bounded flow simulations. In Chapter 4, a new dynamic wall model free of *a priori* tunable parameters based on the invariance of wall stress under test filtering is introduced. Additional motivation and survey of prior studies for each of these objectives is provided at the beginning of each chapter and intermediate summaries will be given at the end of the chapters. Finally, in Chapter 5, concluding remarks are given.

1.1 Accomplishments

Key contributions of the present study are listed below.

- Developed the minimum-dissipation SGS model and extended the model to anisotropic grids. (Collaboration with W. Rozema and R. W. C. P. Verstappen)
- Provided theoretical framework to estimate the discrete Poincaré constant for different numerical discretizations.
- Extended anisotropic minimum-dissipation SGS model to the scalar transport equation.
- Developed two benchmark cases to study the error convergence of SGS models in LES of wall-bounded flows without the limitation of the wall.
- Demonstrated the error scaling in the mean velocity profile, turbulence intensities, and energy spectra in the outer region of wall-bounded flows for the dynamic Smagorinsky model and anisotropic minimum-dissipation model
- Provided a relevant physical length-scale to collapse the SGS model errors
- Motivated the use of the slip boundary condition with transpiration for wall-modeled LES through theoretical and empirical methods.
- Provided a physical explanation of the well-known streamwise turbulence intensity over-prediction in coarse LES and demonstrated the alleviation of the problem using the slip boundary condition.
- Provided a framework to develop dynamic wall models using the balance of wall stress tensors at different grid- and test-filter levels.
- Developed a dynamic slip wall model for equilibrium and non-equilibrium canonical flows.

Chapter 2

Minimum dissipation subgrid-scale models*

2.1 Motivation

The LES equations are formally derived by applying a low-pass spatial filter to the Navier-Stokes equations [76]. The filtered incompressible Navier-Stokes equations can be written as

$$\frac{\partial \tilde{u}_i}{\partial t} + \frac{\partial \tilde{u}_i \tilde{u}_j}{\partial x_j} = -\frac{1}{\rho}\frac{\partial \tilde{p}}{\partial x_i} + \nu \frac{\partial^2 \tilde{u}_i}{\partial x_j \partial x_j} - \frac{\partial \tau_{ij}}{\partial x_j}, \quad \frac{\partial \tilde{u}_i}{\partial x_i} = 0, \tag{2.1}$$

where u_i are the velocity components, ρ is the fluid density, ν is the kinematic viscosity, and p is the pressure. The filter operator, denoted by $\tilde{(\cdot)}$, is assumed to commute with the spatial differentiation operator, and $\tau_{ij} = \widetilde{u_i u_j} - \tilde{u}_i \tilde{u}_j$ is the subgrid-scale (SGS) stress tensor. The SGS stress tensor represents the effect of the unresolved scales on the resolved eddies. The objective of LES modeling is to approximate τ_{ij} by τ_{ij}^{SGS} in terms of the resolved velocity field $\bar{u}_i$, which is obtained by solving the LES equations

$$\frac{\partial \bar{u}_i}{\partial t} + \frac{\partial \bar{u}_i \bar{u}_j}{\partial x_j} = -\frac{1}{\rho}\frac{\partial \bar{p}}{\partial x_i} + \nu \frac{\partial^2 \bar{u}_i}{\partial x_j \partial x_j} - \frac{\partial \tau_{ij}^{\mathrm{SGS}}}{\partial x_j}, \quad \frac{\partial \bar{u}_i}{\partial x_i} = 0, \tag{2.2}$$

*Part of the contents of this chapter have been published in *Physics of Fluids*, volume 27, 085107 (2015) with coauthors Wybe Rozema, Parviz Moin, and Roel Verstappen [135] and in *Physical Review Fluids*, volume 1, 041701(R) (2016) with coauthors Mahdi Abkar and Parviz Moin [1].

where $(\bar{\cdot})$ denotes resolved LES quantities. This approximation of $\bar{u}_i$ is due to the fact that an LES model is not exact, and the solution of the LES equations (2.2) are not identical to the solutions to the filtered Navier-Stokes equations (2.1); however, we expect $\tilde{u}_i \approx \bar{u}_i$ for an accurate model. By modeling the SGS scale terms with the resolved field, the grid requirements to solve the governing equations are reduced significantly. As accurate prediction of turbulence statistics is important in many scientific and engineering applications, the development of accurate yet computationally efficient SGS models for LES is an important task in turbulence research.

Eddy-viscosity SGS models, where the effect of the unresolved eddies is incorporated by locally increasing the viscosity through an eddy viscosity ν_e, are popular since they are robust in practice and principally respect the dissipative character of turbulence. A classical eddy-viscosity model is the Smagorinsky model [146], where the eddy viscosity is given by the Smagorinsky coefficient. With the theoretically estimated Smagorinsky coefficient, the model gives satisfactory results in simulations of decaying homogeneous isotropic turbulence [87, 91, 5]. However, the Smagorinsky model inappropriately produces non-zero eddy dissipation for laminar and transitional flows [104, 121, 166]. This causes erroneous predictions of the shear stress at solid walls and delays transition to turbulence. In simulations of specific laminar or transitional flows, acceptable results can sometimes be obtained by decreasing the Smagorinsky coefficient [35, 165], but no single value of the Smagorinsky coefficient gives satisfactory results for general laminar, transitional, and turbulent flow. Therefore, the Smagorinsky model often fails in LES of practical flows.

The Smagorinsky model can be improved by computing the value of the Smagorinsky coefficient with the dynamic procedure [42, 77]. The dynamic procedure determines the Smagorinsky coefficient dynamically by comparing the eddy dissipation at two filter levels. The dynamic Smagorinsky model (DSM) gives the correct level of eddy dissipation, and appropriately switches off for laminar and transitional flow [119, 92]. However, the DSM requires increased computational complexity compared to the Smagorinsky model and needs averaging in homogeneous directions and clipping of negative values to zero to attain numerical stability.

The eddy viscosity model can also be improved by modifying the functional dependence of the eddy viscosity on the LES solution. For example, the WALE model is designed to switch off at a desired rate near solid walls, and the Vreman model takes a fundamental approach to appropriately switch off for laminar flow. The analysis by Vreman locally characterizes a flow algebraically by the resolved velocity gradient tensor and rigorously derives the classification of flows for which the exact SGS tensor gives no turbulence dissipation. The eddy viscosity is then set to a function of the LES solution which vanishes for these flows. The resulting Vreman model show similar performance to DSM in simulations of a temporal mixing layer and turbulent channel flow. However, the WALE and Vreman models still gives eddy dissipation for solid body rotation. Additionally, they share the drawback that the model constant must be adapted to the mesh refinement so that the proper amount of energy is drained from the resolved scales.

This chapter introduces a new eddy-viscosity SGS model first introduced in Verstappen et al. [163] and improved in Rozema et al. [136], which gives the minimum eddy dissipation required to remove energy pile-up in the smallest resolved scales of the LES solution. The MD model appropriately switches off for laminar and transitional flow, has low computational complexity, and it is proportional to the exact SGS tensor on isotropic grids. The model produces good results on isotropic grids for various flow configurations. However, it is also demonstrated that on anisotropic grids the MD model is not proportional to the exact SGS tensor and that its results are primarily determined by an approximated length scale for the grid size. A correction for anisotropic grids is presented in the form of the anisotropic minimum-dissipation (AMD) model. A new method to numerically estimate the discrete Poincaré constant for the MD and AMD model is introduced. The MD and AMD models are applied to simulation of decaying isotropic turbulence, temporal mixing layer, and turbulent channel flow. Finally, an extension of the AMD model to the scalar transport equation with applications to the atmospheric boundary layer is proposed.

2.2 Minimum-dissipation subgrid-scale models

2.2.1 Formulation

Let us consider the continuous solution of the LES equations (2.2), $\bar{u}_i$, and define the box filtered LES velocity field with domain Ω_Δ as

$$\tilde{\bar{u}}_i = \frac{1}{|\Omega_\Delta|}\int_{\Omega_\Delta} \bar{u}_i \,\mathrm{d}\Omega_\Delta, \tag{2.3}$$

where the filter size of both the box filter and the underlying filter operator associated with the LES equations is Δ. Then, the subfilter scales of the LES solution corresponding to the filter box Ω_Δ are given by the residual field $(\bar{u}_i - \tilde{\bar{u}}_i)$, and the SGS model must keep them from becoming dynamically significant. The evolution equation of the LES subfilter energy, $(\bar{u}_i - \tilde{\bar{u}}_i)(\bar{u}_i - \tilde{\bar{u}}_i)/2$, cannot be expressed exclusively in terms of the resolved LES solution, and thus it is impossible to directly derive a practical SGS model from the evolution of the LES subfilter energy. However, if the subfilter scales are assumed to be periodic on the filter box Ω_Δ, an upper bound for the LES subfilter energy can be obtained from the Poincaré inequality [162, 164]

$$\int_{\Omega_\Delta} \frac{1}{2}(\bar{u}_i - \tilde{\bar{u}}_i)(\bar{u}_i - \tilde{\bar{u}}_i)\,\mathrm{d}\Omega_\Delta \leq C_\Delta \int_{\Omega_\Delta} \frac{1}{2}\frac{\partial \bar{u}_i}{\partial x_j}\frac{\partial \bar{u}_i}{\partial x_j}\,\mathrm{d}\Omega_\Delta, \tag{2.4}$$

where the Poincaré constant C_Δ is equal to the inverse of the smallest non-zero eigenvalue of the negative Laplace operator $-\nabla^2$ for a smooth, bounded domain Ω_Δ. The equality sign holds if $\bar{u}_i$ is fully aligned with the eigenfunction of $-\nabla^2$ associated with the smallest non-zero eigenvalue. The Poincaré inequality suggests that the subfilter energy of the LES solution can be confined by imposing an upper bound on the velocity gradient energy, $(\partial \bar{u}_i/\partial x_j)\,(\partial \bar{u}_i/\partial x_j)\,/2$.

The evolution of the velocity gradient energy density can be expressed as

$$\frac{\partial}{\partial t}\left(\frac{1}{2}\frac{\partial \bar{u}_i}{\partial x_j}\frac{\partial \bar{u}_i}{\partial x_j}\right) = -\frac{\partial \bar{u}_i}{\partial x_k}\frac{\partial \bar{u}_j}{\partial x_k}\bar{S}_{ij} - 2\nu\frac{\partial \bar{S}_{ij}}{\partial x_k}\frac{\partial \bar{S}_{ij}}{\partial x_k} - 2\frac{\partial \bar{S}_{ij}}{\partial x_k}\frac{\partial \nu_e \bar{S}_{ij}}{\partial x_k} + \frac{\partial f_i}{\partial x_i}\,, \tag{2.5}$$

where the right-hand-side terms are the production, viscous dissipation, SGS dissipation, and flux of velocity gradient energy, respectively [162], $\bar{S}_{ij}$ is the resolved rate-of-strain tensor, and $\tau_{ij}^{\mathrm{SGS}} - 1/3\delta_{ij}\tau_{kk}^{\mathrm{SGS}} = -2\nu_e\bar{S}_{ij}$ with δ_{ij} being the Kronecker delta. Upon spatial integration of Eq. (2.5) over the filter box Ω_Δ, the divergence $\partial f_i/\partial x_i$ leads to boundary terms. Boundary terms express transport of velocity gradient energy instead of production or dissipation, and are ignored in the derivation of the minimum-dissipation model. For the LES subfilter scales to stay bounded at the natural rate of dissipation given by ν, the production term must be balanced by the SGS dissipation term. Approximating the eddy viscosity to be constant over the filter box and ignoring boundary terms, this constraint can be rewritten as

$$\int_{\Omega_\Delta} -\frac{\partial \bar{u}_i}{\partial x_k}\frac{\partial \bar{u}_j}{\partial x_k}\bar{S}_{ij}\,\mathrm{d}\Omega_\Delta = 2\nu_e\int_{\Omega_\Delta}\frac{\partial \bar{S}_{ij}}{\partial x_k}\frac{\partial \bar{S}_{ij}}{\partial x_k}\,d\Omega_\Delta. \tag{2.6}$$

or equivalently,

$$\int_{\Omega_\Delta} -\frac{4}{3}\bar{S}_{ij}\bar{S}_{jk}\bar{S}_{ki}\,\mathrm{d}\Omega_\Delta = 2\nu_e\int_{\Omega_\Delta}\frac{\partial \bar{S}_{ij}}{\partial x_k}\frac{\partial \bar{S}_{ij}}{\partial x_k}\,d\Omega_\Delta. \tag{2.7}$$

The SGS dissipation term is bounded by the Poincaré inequality

$$\int_{\Omega_\Delta}\bar{S}_{ij}\bar{S}_{ij}\,\mathrm{d}\Omega_\Delta \le C_\Delta\int_{\Omega_\Delta}\frac{\partial \bar{S}_{ij}}{\partial x_k}\frac{\partial \bar{S}_{ij}}{\partial x_k}\,\mathrm{d}\Omega_\Delta. \tag{2.8}$$

Thus, an eddy-viscosity model gives sufficient eddy dissipation to cancel the production of velocity gradient energy if the inequality

$$4\int_{\Omega_\Delta} III(\bar{\boldsymbol{u}})\,\mathrm{d}\Omega_\Delta \le 4\frac{\nu_e}{C_\Delta}\int_{\Omega_\Delta} II(\bar{\boldsymbol{u}})\,\mathrm{d}\Omega_\Delta \tag{2.9}$$

holds, where $II(\bar{\boldsymbol{u}}) = 1/2(\bar{S}_{ij}\bar{S}_{ij})$ and $III(\bar{\boldsymbol{u}}) = -1/3(\bar{S}_{ij}\bar{S}_{jk}\bar{S}_{ki})$ are the second and third invariants of the resolved rate-of-strain tensor, respectively. The minimum eddy dissipation that satisfies this condition is

$$\nu_e = C_\Delta\frac{\max\left\{\int_{\Omega_\Delta} III(\bar{\boldsymbol{u}})\,\mathrm{d}\Omega_\Delta, 0\right\}}{\int_{\Omega_\Delta} II(\bar{\boldsymbol{u}})\,\mathrm{d}\Omega_\Delta}. \tag{2.10}$$

Using an approximation of the integrals given by the mid-point rule and a numerical approximation of the Poincaré constant $C_\Delta = C\Delta^2$, the MD model [136, 134] is given as

$$\nu_e = C\Delta^2 \frac{\max\{III(\bar{\boldsymbol{u}}), 0\}}{II(\bar{\boldsymbol{u}})}, \tag{2.11}$$

where C is a model constant and Δ is the LES filter size or grid resolution.

The MD model has desirable practical and theoretical properties. The third invariant of the rate-of-strain tensor vanishes in flows that are laminar or 2-dimensional [166]. Thus, the MD model is proportional to the exact SGS tensor and gives zero SGS dissipation for these flows. The model also switches off for two-dimensional flow [162, 108]. Also, the computational complexity of the model is low. Compared to the constant-coefficient Smagorinsky model, the MD model needs only additional computation of the third invariant of a tensor which is readily available. Moreover, the eddy viscosity is evaluated locally without the need for averaging in homogeneous directions. Finally, the production term in Eq. (2.5) is proportional to the dissipation of the leading-order term of a Taylor expansion of the exact SGS tensor on isotropic grids [165, 166]. This dissipation is proportional to $III(\bar{\boldsymbol{u}})$, and thus on isotropic grids, the MD model is consistent with the eddy dissipation of the exact SGS tensor.

2.2.2 A correction for anisotropic grids

The derivation of the MD model applies the box filter to the LES solution, and confines the energy of LES subfilter scales by application of the Poincaré inequality. This gives a model constant C_Δ which depends on the size of the filter box Δ. On isotropic grids, the LES filter size Δ of the MD model is set equal to the grid spacing

$$\Delta = \Delta_1 = \Delta_2 = \Delta_3, \tag{2.12}$$

where Δ_i denotes the grid spacing in the three spatial directions. However, on anisotropic grids, the MD model requires approximation of the filter size Δ. In the literature, the filter

size has been set according to a numerical counterpart of the Poincaré constant [162]

$$\frac{3}{\Delta^2} = \frac{1}{\Delta_1^2} + \frac{1}{\Delta_2^2} + \frac{1}{\Delta_3^2}. \tag{2.13}$$

However, for grid cells with a large aspect ratio, this filter size approximation is dominated by the grid spacing in the finest grid direction. A more conventional approximation of the filter size on anisotropic grids is given by the cube root of the cell volume [34]

$$\Delta = (\Delta_1 \Delta_2 \Delta_3)^{1/3}. \tag{2.14}$$

On anisotropic grids the above approximations give different filter sizes. It will be demonstrated in Section 2.3 that on anisotropic grids the results of the MD model are primarily determined by the form of the approximation of the filter size and that neither approximation gives satisfactory results.

Moreover, whereas the MD model is proportional to the exact SGS stress tensor on isotropic grids, this desirable property does not hold for anisotropic grids. This motivates the derivation of an MD model which does not require an approximation of the filter size and is consistent with the exact SGS tensor on both isotropic and anisotropic grids.

Rozema et al. [136], Rozema [134] showed that the dependence of the model constant on the size of the filter box can be sidestepped by using a modified Poincaré inequality. For simplicity, it is assumed that the filter box Ω_Δ is rectangular with dimensions Δ_i. The energy of the subfilter scales can then be confined using a modified Poincaré inequality

$$\int_{\Omega_\Delta} \frac{1}{2}(\bar{u}_i - \tilde{\bar{u}}_i)(\bar{u}_i - \tilde{\bar{u}}_i)\,\mathrm{d}\Omega_\Delta \leq \int_{\Omega_\Delta} \frac{1}{2} C \frac{\partial_s \bar{u}_i}{\partial x_j} \frac{\partial_s \bar{u}_i}{\partial x_j}\,\mathrm{d}\Omega_\Delta, \tag{2.15}$$

where $\partial_s/\partial x_j = \Delta_j \partial/\partial x_j$ (repeated indices do not imply summation) is the scaled gradient operator. The model constant C is now equal to the inverse of the smallest non-zero eigenvalue of $-(\partial_s/\partial x_j)(\partial_s/\partial x_j)$ integrated over the filter box Ω_Δ, which is independent of the size of the filter box. Thus, whereas the Poincaré inequality in Eq. (2.4) incorporates the dependence on the size of the filter box in the Poincaré constant C_Δ, the modified

Poincaré inequality incorporates the dependence on the size of the filter box by scaling the velocity gradient.

The modified Poincaré inequality demonstrates that the subfilter energy can be confined by imposing a bound on the scaled velocity gradient energy. If the eddy viscosity and the filter sizes are assumed to be constant on the filter box Ω_Δ, then the equivalent derivation as the MD model gives

$$\nu_e = \frac{\max\left\{\int_{\Omega_\Delta} -C(\partial_s\bar{u}_i/\partial x_k)(\partial_s\bar{u}_j/\partial x_k)\bar{S}_{ij}\,\mathrm{d}\Omega_\Delta, 0\right\}}{\int_{\Omega_\Delta}\left(\partial\bar{u}_m/\partial x_l\right)\left(\partial\bar{u}_m/\partial x_l\right)\,\mathrm{d}\Omega_\Delta}. \tag{2.16}$$

In practical applications of this model, the integrals over the filter box are approximated as

$$\nu_e = \frac{\max\left\{-C(\partial_s\bar{u}_i/\partial x_k)(\partial_s\bar{u}_j/\partial x_k)\bar{S}_{ij}, 0\right\}}{\left(\partial\bar{u}_m/\partial x_l\right)\left(\partial\bar{u}_m/\partial x_l\right)}. \tag{2.17}$$

The AMD model is consistent with the exact SGS stress tensor on anisotropic grids. Taylor expansion of the SGS tensor gives [32]

$$\tau_{ij} = \overline{\bar{u}_i\bar{u}_j} - \bar{u}_i\bar{u}_j = \frac{1}{12}\frac{\partial_s\bar{u}_i}{\partial x_k}\frac{\partial_s\bar{u}_j}{\partial x_k} + \mathcal{O}(\Delta^4). \tag{2.18}$$

Thus, the eddy dissipation of the exact SGS stress tensor is

$$-\tau_{ij}\bar{S}_{ij} = -\frac{1}{12}\frac{\partial_s\bar{u}_i}{\partial x_k}\frac{\partial_s\bar{u}_j}{\partial x_k}\bar{S}_{ij} + \mathcal{O}(\Delta^4). \tag{2.19}$$

The leading-order term of this expansion is proportional to the term in the numerator of the eddy viscosity of the AMD model. This demonstrates consistency of the AMD model with the exact SGS dissipation for anisotropic grids. The leading-order term of the Taylor expansion of the exact SGS tensor is also known as the gradient model [165]. Thus, the AMD model gives zero eddy dissipation if the gradient model gives zero eddy dissipation. Consistency with the gradient model is a desirable property, as a priori tests show that the gradient model has good correlation with the exact SGS tensor [32]. Also, the analysis by Vreman restricted to separable filters shows that the gradient model gives zero SGS

dissipation when the exact SGS stress tensor is zero [166]. This confirms that the AMD model switches off for flows with vanishing SGS dissipation. It is important to remark that the AMD model is only proportional to the gradient model and is not identical to it. Indeed, the gradient model is known to produce inadequate dissipation while the AMD model provides better predictions as shown in section 2.3. The AMD model also switches off for two-dimensional flow on anisotropic grids unlike the Vreman model and has low computational complexity compared to the DSM.

2.2.3 The discrete Poincaré constant

Application of the MD and AMD models in a practical LES requires setting of the model constant C. Payne and Weinberger [115] have derived the Poincaré constant $C_\Delta = (\Delta/\pi)^2$ for a convex box of diameter Δ, which yields $C = 1/\pi^2$ for the continuous equations. However, the coefficient of an SGS model should depend on the numerical method and on the nature of the turbulence at the cut-off of the LES filter [93].

The difference in the Poincaré constant for different numerical methods can be explained in terms of the discrete differentiation operator. The Poincaré inequality can be written as

$$\begin{aligned}\int_{\Omega_\Delta} \frac{1}{2}(\bar{u}_i - \tilde{\bar{u}}_i)(\bar{u}_i - \tilde{\bar{u}}_i)\,\mathrm{d}\Omega_\Delta &\leq C_\Delta \int_{\Omega_\Delta} \frac{1}{2}\frac{\partial \bar{u}_i}{\partial x_j}\frac{\partial \bar{u}_i}{\partial x_j}\,\mathrm{d}\Omega_\Delta \\ &= C_\Delta \int_{\Omega_\Delta} \frac{1}{2}\mathcal{F}^{-1}(\mathrm{i}k_j\hat{\bar{u}}_i)\mathcal{F}^{-1}(\mathrm{i}k_j\hat{\bar{u}}_i)\,\mathrm{d}\Omega_\Delta, \end{aligned} \tag{2.20}$$

where $\hat{(\cdot)}$ is the Fourier transformation, $\mathcal{F}^{-1}$ is the inverse transformation, k_j are the wavenumbers and $\mathrm{i}^2 = -1$. The application of the discrete differentiation operator on the Poincaré inequality then requires a discrete Poincaré constant $\tilde{C}_\Delta$ such that

$$C_\Delta \int_{\Omega_\Delta} \frac{1}{2}\mathcal{F}^{-1}(\mathrm{i}k_j\hat{\bar{u}}_i)\mathcal{F}^{-1}(\mathrm{i}k_j\hat{\bar{u}}_i)\,\mathrm{d}\Omega_\Delta \approx \tilde{C}_\Delta \int_{\Omega_\Delta} \frac{1}{2}\mathcal{F}^{-1}(\mathrm{i}\tilde{k}_j\hat{\bar{u}}_i)\mathcal{F}^{-1}(\mathrm{i}\tilde{k}_j\hat{\bar{u}}_i)\,\mathrm{d}\Omega_\Delta, \tag{2.21}$$

since the wavenumbers are replaced by the modified wavenumbers $\tilde{k}_j$. Assuming the flow is

isotropic and in the inertial range, that is $E(k) \propto k^{-5/3}$,

$$\tilde{C}_\Delta \approx C_\Delta \frac{\int_0^\infty k^2 E(k) \mathrm{d}k}{\int_0^\infty \tilde{k}^2 E(k) \mathrm{d}k}. \tag{2.22}$$

This yields $\tilde{C}_\Delta = 0.28\Delta^2$ for the second-order central finite difference, and $\tilde{C}_\Delta = 0.19\Delta^2$ for the fourth-order central finite difference. Note that even for finite difference schemes on staggered grids, the evaluation of the derivative term $\partial \bar{u}_i / \partial x_j$ on the right-hand-side of Eq. (2.20), where the discrete Poincaré constant is derived, must be at the locations of the $\bar{u}_i$ term, and the improvement of the modified wavenumber does not take effect in this case.

The constant C can also be computed empirically by varying its value to obtain satisfactory results for the simulation of decaying isotropic turbulence in terms of decay rate [136]. For the MD model, this results in $C = 0.33$ for second-order finite difference methods and $C = 0.24$ for fourth-order finite difference methods. For the AMD model, this results in $C = 0.30$ for second-order finite difference methods and $C = 0.21$ for fourth-order finite difference methods. In both cases, the values are in fair agreement with the theoretical values given above.

2.3 Performance of minimum-dissipation models

To validate the proposed MD and AMD models, simulations are performed of decaying isotropic turbulence, a temporal mixing layer, and turbulent channel flow. The simulations have been performed with two numerical methods: 1) second- and fourth-order central discretization of the compressible Navier-Stokes equations on a collocated computational grid [66, 135] with a low-storage fourth-order Runge-Kutta time-advancing scheme [134], and 2) a staggered second-order finite difference method [110] with fractional-stepping [62] for the incompressible Navier-Stokes equations with a third-order Runge-Kutta time-advancing scheme [176]. In both cases, the eddy viscosity of the SGS model is computed at the cell centers with the same numerical method as the governing equations.

2.3.1 Decaying isotropic turbulence

To assess the MD and AMD models, simulations of the decaying isotropic turbulence experiment by Comte-Bellot and Corrsin are performed [33]. In these experiments, turbulence is generated by a mesh with size $M = 5.08$ cm in a flow of mean velocity $U_0 = 1000$ cm/s. Energy spectra of the decaying turbulence are recorded at three stations $42M$, $98M$, and $171M$ downstream of the mesh. The simulations are simplified by considering the flow inside a cube of length $11M$ which moves along with the mean flow and passes the physical mesh at $t = 0$ s. Thus, the turbulence in the cube is expected to match the measured energy spectra at $t = 42M/U_0$, $t = 98M/U_0$, and $t = 171M/U_0$, with corresponding $Re_\lambda = \langle u_1^2 \rangle^{1/2} L_\lambda / \nu = 71.6$, 65.3, and 60.7 respectively, where L_λ is the Taylor micro-scale.

The simulations are performed with both the collocated method for compressible flow and the staggered method for incompressible flow. To assess the influence of the numerical discretization, both second-order and fourth-order accuracy were used for the collocated method. Simulations are performed with the DSM [77], the MD model (Eq. 2.11), and the AMD model (Eq. 2.17). The DSM is implemented with a box filter as the test filter with averaging in the homogeneous directions. The computational grid is isotropic with 64 cells in each direction. The Reynolds number based on the size of the computational domain is $Re = 10,129$, and the time step size is set to $\Delta_t = 1.59 \times 10^{-3} M/U_0$. The initial condition is generated by fitting a velocity field with randomized phases to the energy spectrum measured at the first station. The random phases are adjusted by performing a preliminary simulation from $t = 0$ s to $t = 42M/U_0$ and rescaling the adjusted velocity field to the energy spectrum measured at the first station [58]. The resulting field is used as the initial condition for the simulations.

Figure 2.1 shows the total energy K and energy spectra $E_K(k)$ obtained with the staggered second-order accurate simulation method with the DSM, the MD model, and the AMD model, where the energy is non-dimensionalized by the total energy at the first measurement station, and k is the wavenumber nondimensionalized by the length of the cube, $11M$. The data points in the energy decay plot shown in Figure 2.1(a) have been obtained

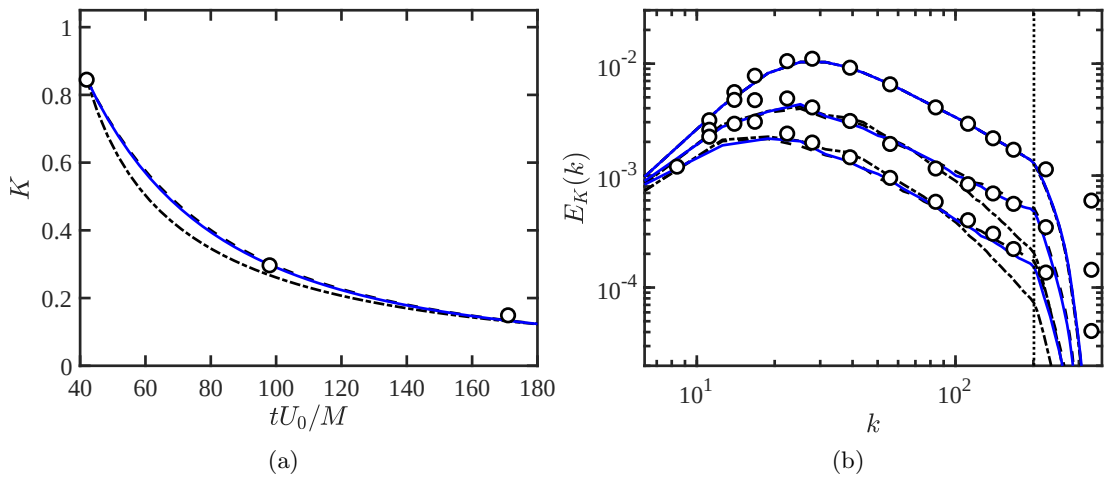

Figure 2.1: (a) Resolved kinetic energy up to the cut-off wavenumber and the (b) energy spectra at the three measurement stations obtained with the second-order accurate simulation method with the DSM (-·-·-), the MD model (- - - -), and the AMD model (——). Experimental data (○) plotted for comparison. Cut-off wavenumber given by the grid resolution (·····).

by fitting the measured energy spectrum to the computational grid and computing the total kinetic energy, effectively only accounting for the energy of the resolved scales of the LES. The energy dissipation obtained with the MD and AMD models accurately agrees with the energy decay from the experiment, whereas the energy decays more rapidly with DSM. Energy spectra obtained with the MD and AMD model are also accurate, as seen in Figure 2.1(b). The energy spectra obtained with the MD and AMD models differ from energy spectra obtained with the DSM at wave numbers near the grid cut-off, where the spectra given by the DSM is shown to be too dissipative. Although not shown, box-filtering the experimental spectra with filter size equivalent to the grid resolution provides better agreement with DSM results. However, in applications of LES, an SGS model that is able to produce the unfiltered results up to grid cut-off is more advantageous as quantities of practical interest are based on unfiltered statistics.

The experiment is repeated using a collocated method for both second order (not shown) and fourth-order accurate methods (shown in Figure 2.2). The energy decay obtained with

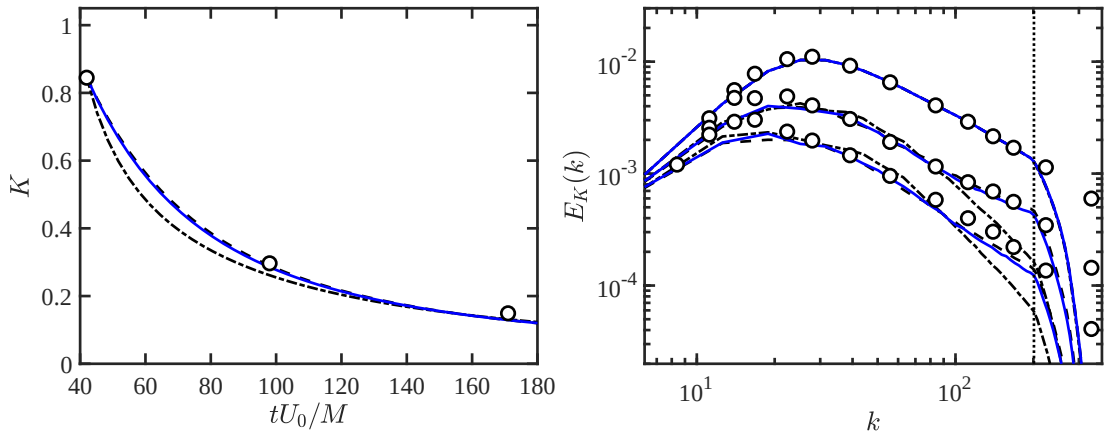

Figure 2.2: (a) Resolved kinetic energy up to the cut-off wavenumber and the (b) energy spectra at the three measurement stations obtained with the fourth-order accurate simulation method with the DSM (-·-·-), the MD model (- - - -), and the AMD model (——). Experimental data (○) plotted for comparison. Cut-off wavenumber given by the grid resolution (·····).

the MD model and the AMD model closely match the experiment in all cases. The computed energy spectra demonstrate that both the MD and AMD models appropriately capture the turbulent energy. In summary, the proposed MD and AMD models have produced accurate simulations of decaying grid turbulence with different orders of accuracy of the spatial discretization, and with the coefficient C estimated as in Section 2.2.3.

2.3.2 Temporal mixing layer

To assess the applicability of MD and AMD models to transitional flow and anisotropic grids, simulations of a temporal mixing layer are performed. A temporal mixing layer consists of two streams with opposite flow velocities. A Kelvin-Helmholtz instability originates at the interface of the two streams, and eventually causes transition to turbulence. The temporal mixing layer is expected to be self-similar in the turbulent regime [133, 46].

The temporal mixing layer studied in this chapter is similar to the weakly compressible mixing layer at a high Reynolds number studied by Vreman [166]. The coordinate x_1 is

aligned with the streamwise direction, the coordinate x_2 with the direction normal to the mixing layer, and the coordinate x_3 with the spanwise direction. All the quantities are nondimensionalized by half the initial vorticity thickness of the mixing layer, the far-field streamwise velocity, and the free-stream temperature and pressure. The initial dimensionless velocity field is given by a hyperbolic tangent

$$u_1 = \tanh(x_2), \quad u_2 = 0, \quad u_3 = 0, \tag{2.23}$$

with random perturbations of small magnitudes added near the center plane $x_2 = 0$ to trigger transition to turbulence. The initial nondimensionalized temperature profile is set to

$$\phi = 1 + \frac{1}{2}(\gamma - 1)Ma^2 (1 - u_1)(1 + u_1), \tag{2.24}$$

where γ is the heat capacity ratio and Ma is the free-stream Mach number. The initial pressure is set equal to the free-stream pressure $p = 1$. The Reynolds number based on half the initial vorticity thickness is $100,000$, and the free-stream Mach number is $Ma = 0.25$. The computational domain spans 90 times half the initial vorticity thickness in each direction. The simulations are performed on anisotropic rectangular grids with constant grid spacing in each direction. The computational grid has 90 cells in the streamwise and spanwise directions, and 180, 360, or 720 grid cells in the direction normal to the mixing layer. Thus, the computational grids have aspect ratios $\Delta_1/\Delta_2 = \Delta_3/\Delta_2$ of 2, 4, and 8, respectively. Periodic boundary conditions are imposed in the streamwise and spanwise directions, and free-slip boundary conditions are imposed at the boundaries in the direction normal to the mixing layer.

The simulations are performed with the fourth-order accurate collocated method for compressible flow, and with the DSM, Vreman, MD, and AMD models. On anisotropic grids, the MD model requires an approximation of the filter size. Simulations are performed with the approximation proposed in the literature in Eq. (2.13), labeled MD1, and with the conventional approximation in Eq. (2.14), labeled MD2. The growth rate of the momentum thickness θ of the mixing layer, the variance of the streamwise velocity, the dissipation rate

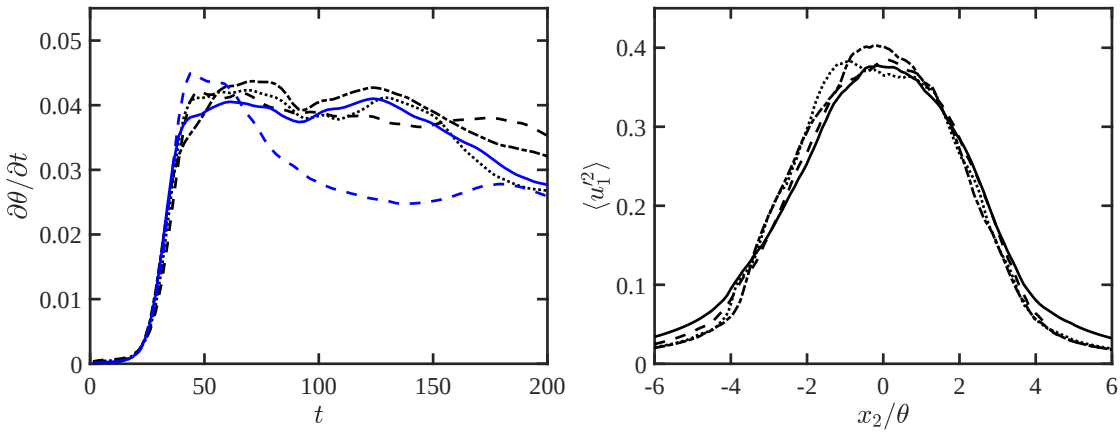

Figure 2.3: (a) Growth rate of the momentum thickness obtained in simulations of the temporal mixing layer on the grid with aspect ratio 4 with the DSM (-·-·-), Vreman (·····), MD1 (- - - ·), MD2 (- - - ·), and AMD (——) models, and the (b) variance of the streamwise velocity as function of x_2 with the AMD model at $t = 80$ (——), 100 (- - - ·), 120 (-·-·-), and 140 (·····).

of total kinetic energy, and streamwise energy spectra $E_1(k_1)$ at the center plane of the mixing layer are presented.

First, the results obtained on the grid with an aspect ratio of 4 are presented. Figure 2.3(a) shows the growth rate of the mixing layer. The DSM and the Vreman model are known to appropriately switch off for laminar and transitional flows [165, 166]. Transition of the mixing layer occurs at approximately the same time for the DSM and the Vreman model. For both models, the growth rate of the mixing layer is approximately constant from $t = 50$ to $t = 140$, which indicates self-similarity of the mixing layer in the turbulent regime. The MD and AMD models predict transition to turbulence at approximately the same time, suggesting that the MD and AMD models appropriately switch off for transitional flow.

The behavior of the MD model in the turbulent regime is sensitive to the approximation of the filter size, Δ. For the MD2 model the growth rate of the mixing layer is approximately equal to the growth rate predicted by the DSM, but for the MD1 model, the growth rate is considerably smaller. The AMD model does not require an approximation of the filter size

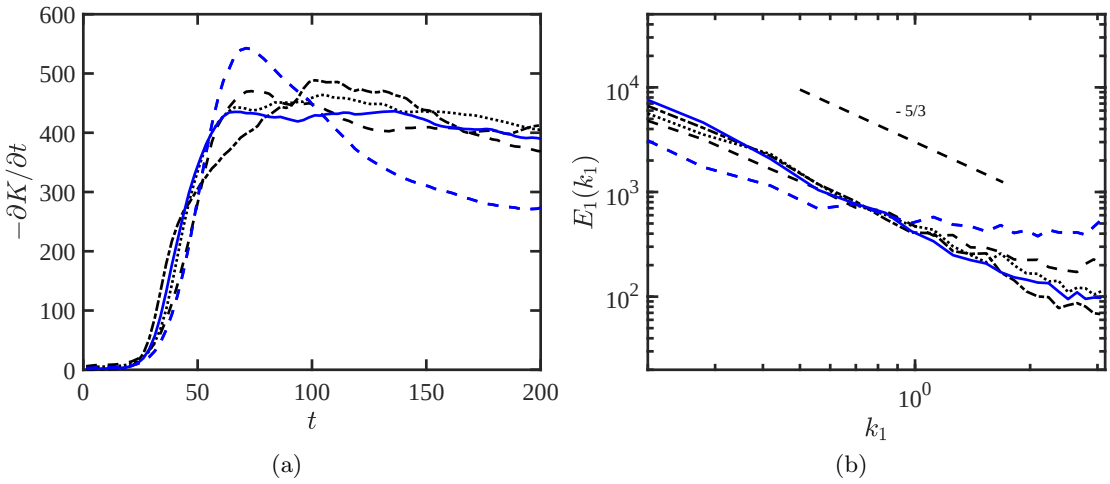

Figure 2.4: (a) Decay rate of the total energy and the (b) streamwise energy spectra as a function of streamwise wavenumber k_1 at the center plane of the mixing layer at $t = 140$ obtained in simulations of the temporal mixing layer on the grid with aspect ratio 4 with the DSM (- · - · -), Vreman (·····), MD1 (- - - ·), MD2 (- - - -), and AMD (——) models.

on anisotropic grids and predicts a growth rate which closely agrees with the growth rate obtained with the DSM and the Vreman model.

Figure 2.3(b) shows the streamwise velocity variance $\langle \bar{u}_1'^2 \rangle$ obtained with the AMD model at different times in the turbulent regime approximately collapse. Here $\langle \cdot \rangle$ denotes averaging in the homogeneous directions (and time if flow is stationary), and $(\cdot)'$ denotes fluctuating quantities. This indicates that the AMD model appropriately captures the self-similar character of the mixing layer in the turbulent regime.

Figure 2.4 shows the temporal rate of change of the total kinetic energy and the streamwise energy spectra at $t = 140$. The kinetic energy is practically constant for the DSM, Vreman, MD1, MD2, and AMD models up to $t = 25$, which confirms that all models considered appropriately switch off for transitional flow. The DSM, Vreman model, MD2, the AMD models predict approximately equal $\partial K/\partial t$ in the turbulent regime. However, the MD1 model predicts significantly higher energy decay rate in the turbulent regime. The energy spectra show a marked quantitative difference between the results obtained with the MD1 model, and the other models. The DSM, Vreman, MD2, and AMD models give

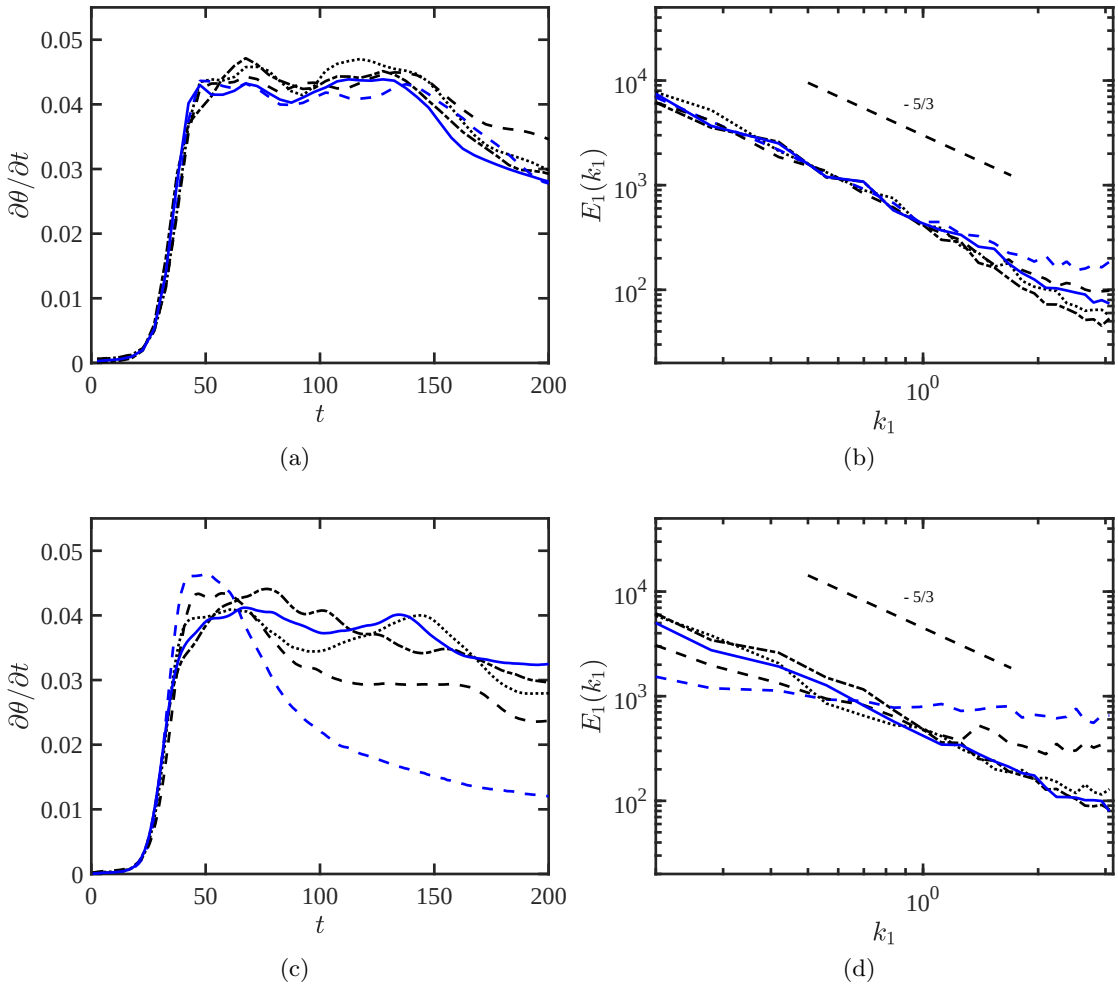

Figure 2.5: Growth rate of the momentum thickness and the streamwise energy spectra at the center plane of the mixing layer at $t = 140$ obtained in simulations of the temporal mixing layer on the grids with aspect ratio 2 (a and b, respectively) and 8 (c and d, respectively) with the DSM (-·-·-), Vreman (·····), MD1 (- - - ·), MD2 (- - - ·), and AMD (——) models.

energy spectra with the desirable $E_1(k_1) \sim k_1^{-5/3}$ power law. However, the MD1 model gives accumulation of energy at scales near the grid cut-off, indicating insufficient energy dissipation on anisotropic grids for the particular filter size approximation (Eq. 2.13).

Figure 2.5 shows the growth rate of the momentum thickness and the streamwise energy spectra for grids with aspect ratios 2 and 8. The results confirm that on grids with considerable anisotropy, the behavior of the MD model is primarily determined by the filter size approximation. At the smaller aspect ratios, results obtained with both filter size approximations closely agree with results obtained with the DSM and the Vreman model. However, at the larger aspect ratios, the MD model behaves differently for the two considered filter size approximations, where both approximations deviate from the $k^{-5/3}$ power law and result in accumulation of kinetic energy near the grid cut-off.

At both aspect ratios, results obtained with the AMD model closely agree with results obtained with the DSM and the Vreman model. The AMD model appropriately switches off for transitional flow, and successfully captures the constant growth rate of the mixing layer in the turbulent regime. Also, the AMD model gives energy spectra with $k^{-5/3}$ power law.

2.3.3 Turbulent channel flow

To assess the applicability of the proposed AMD model to wall-bounded flows, simulations of turbulent channel flow at a friction Reynolds number of $Re_\tau \approx 550$ are performed. The coordinates x_1, x_2, and x_3 are the streamwise, wall-normal, and spanwise directions, respectively. The size of the channel is $2\pi\delta \times 2\delta \times \pi\delta$, where δ is the channel half-height. The simulations were run for at least 100 eddy-turnover times, defined as δ/u_τ, after transients, where u_τ is the friction velocity. The channel flow is driven by a constant streamwise pressure gradient.

Large-eddy simulations are performed with the staggered second-order finite difference method. The simulations are performed on a coarse grid with 64 cells in each direction. The grid spacing is uniform in the streamwise and spanwise directions. In the wall-normal direction the grid stretches towards the wall according to a hyperbolic tangent function.

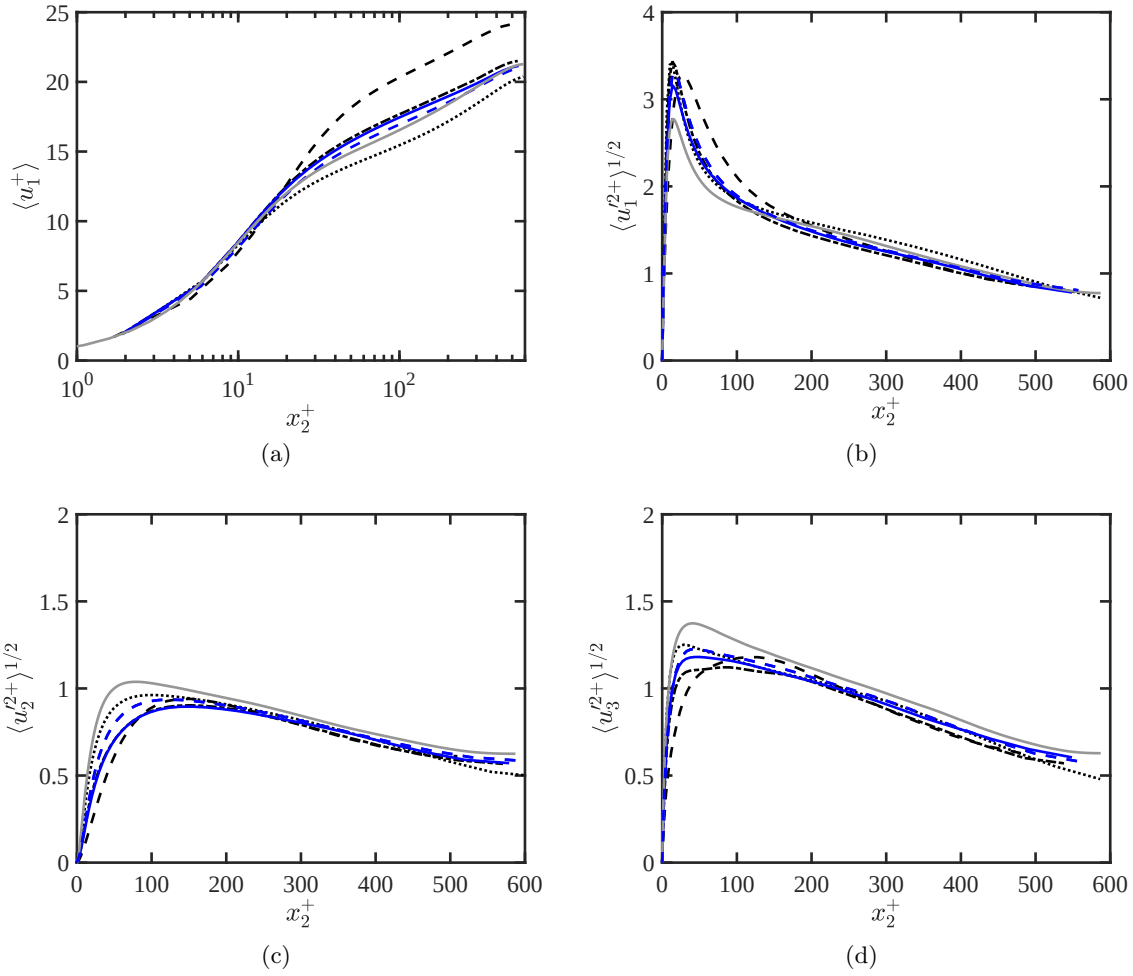

Figure 2.6: (a) Mean streamwise velocity and the (b) streamwise, (c) spanwise, and (d) wall-normal turbulence intensities for no SGS model (·····), DSM (-·-·-), MD1 (- - - ·), MD2 (- - - ·), and AMD (——) models. DNS (——) plotted for comparison.

The height of the first grid cell at the wall is ${\Delta_2}^+ \approx 3.5$, where the superscript + denotes viscous units defined by u_τ and ν. Simulations are performed both without an SGS model and with the DSM and AMD models. The results of the simulations are compared with results of DNS by Hoyas and Jiménez [48].

Figure 2.6 shows the mean streamwise velocity and the turbulence intensities. A simulation without an SGS model predicts a lower mass flow than DNS. Both the DSM and the AMD model give satisfactory predictions. Just as in simulations of the temporal mixing layer, results obtained with the two MD models are primarily determined by the used filter size approximation. Results obtained with the MD1 closely agree with the DNS, but the filter size approximation for MD2 is too dissipative. This is in contrast with the simulations of the temporal mixing layer, which suggests that neither of the two filter size definitions discussed are robust.

It is well known that the accuracy of channel flow simulations with eddy-viscosity models is mainly influenced by the behavior of the SGS model near the wall [104]. The near-wall behavior of the two considered filter size approximations is different due to the stretching of the grid in the wall-normal direction while maintaining constant grid sizes in the wall-parallel directions. Further analysis of the near-wall behavior of the AMD model and its performance in the outer region of wall-bounded flows will be discussed in Chapter 3.

2.4 Extension to the scalar transport equation

The AMD model formulation can be extended to the transport equations for scalar concentration. Applying a box filter, as in the derivation of the filtered Navier-Stokes equations, to the scalar-transport equation gives

$$\frac{\partial \tilde{\phi}}{\partial t} + \frac{\partial \tilde{u}_i \tilde{\phi}}{\partial x_i} = D \frac{\partial^2 \tilde{\phi}}{\partial x_i \partial x_i} - \frac{\partial q_i}{\partial x_i}, \tag{2.25}$$

where D is the scalar diffusivity, and $q_i = \widetilde{u_i\phi} - \tilde{u}_i\tilde{\phi}$ is the LES subfilter scalar flux. The subfilter scalar flux is commonly approximated with an eddy-diffusivity model

$$q_i \approx q_i^{\mathrm{SGS}} = -\frac{\partial D_e \bar{\phi}}{\partial x_i}, \tag{2.26}$$

where D_e is the eddy diffusivity. D_e is related to ν_e by the SGS Schmidt number Sc_e, such that $D_e = \nu_e Sc_e^{-1}$. Since, the turbulent scalar transport is a key component of many environmental and engineering turbulent flows, an extension of the AMD approach to modeling the SGS scalar flux is valuable.

2.4.1 Formulation

The modified Poincaré inequality applied to the scalar concentration is given by

$$\int_{\Omega_\Delta} \frac{1}{2}(\bar{\phi} - \tilde{\bar{\phi}})(\bar{\phi} - \tilde{\bar{\phi}})\,\mathrm{d}\Omega_\Delta \leq C \int_{\Omega_\Delta} \frac{1}{2}\frac{\partial_s \bar{\phi}}{\partial x_i}\frac{\partial_s \bar{\phi}}{\partial x_i}\,\mathrm{d}\Omega_\Delta. \tag{2.27}$$

If the eddy diffusivity is assumed to be constant in the filter box Ω_Δ, then the evolution equations for scaled scalar-concentration gradient energy density, $(\partial_s\bar{\phi}/\partial x_i)(\partial_s\bar{\phi}/\partial x_i)/2$, can be expressed as

$$\frac{\partial}{\partial t}\left(\frac{1}{2}\frac{\partial\bar{\phi}}{\partial x_i}\frac{\partial\bar{\phi}}{\partial x_i}\right) = -\frac{\partial\bar{u}_i}{\partial x_j}\frac{\partial\bar{\phi}}{\partial x_j}\frac{\partial\bar{\phi}}{\partial x_i} - (D + D_e)\frac{\partial^2\bar{\phi}}{\partial x_i\partial x_j}\frac{\partial^2\bar{\phi}}{\partial x_i\partial x_j} + \frac{\partial g_i}{\partial x_i}, \tag{2.28}$$

where g_i are the fluxes of scaled scalar-concentration gradient energy. Upon spatial integration over the filter box Ω_Δ, the divergence terms $\partial g_i/\partial x_i$, can be rewritten as a boundary integral and can be ignored as in the derivation of the AMD model.

Following the same argument as the SGS eddy-viscosity model, the AMD eddy diffusivity is given by

$$D_e = \frac{\max\left\{\int_{\Omega_\Delta} -C_j(\partial_s\bar{u}_i/\partial x_j)(\partial_s\bar{\phi}/\partial x_j)(\partial\bar{\phi}/\partial x_i)\,\mathrm{d}\Omega_\Delta, 0\right\}}{\int_{\Omega_\Delta}(\partial\bar{\phi}/\partial x_k)(\partial\bar{\phi}/\partial x_k)\,\mathrm{d}\Omega_\Delta}. \tag{2.29}$$

By approximating the integrals over the filter box with the mid-point rule, the practical

form of the AMD eddy-diffusivity model can be written as

$$D_e = \frac{\max\left\{-(\partial_s \bar{u}_i/\partial x_j)(\partial_s \bar{\phi}/\partial x_j)(\partial \bar{\phi}/\partial x_i), 0\right\}}{(\partial \bar{\phi}/\partial x_k)(\partial \bar{\phi}/\partial x_k)}. \tag{2.30}$$

Similar to the eddy viscosity model, the computational complexity of the AMD eddy-diffusivity model is comparable to that of the constant coefficient Smagorinsky model, and the AMD SGS scalar flux is consistent with the exact SGS scalar flux on both isotropic and anisotropic grids.

2.4.2 Numerical experiments

To test the performance of the AMD model, a high-Reynolds-number boundary layer flow ($\nu = 0$) with a constant surface scalar flux $Q_* = u_* \phi_*$ is simulated, where u_* is the friction velocity and ϕ_* is the surface potential scalar [1]. The coordinates x_1, x_2, and x_3 are the streamwise, spanwise, and wall-normal directions, respectively. The wall-normal height of the computational domain is set to $H = 1000$m, and the horizontal domain spans are $2\pi H$. The boundary layer is driven by an imposed uniform pressure gradient $-u_*^2/H$ in the streamwise direction. Friction velocity u_* and aerodynamic surface roughness x_o are set to 0.45m/s and 0.1m, respectively, which is similar to the setup in previous studies [127, 153, 82]. The simulations are carried out with resolutions of $48 \times 48 \times 48$, $72 \times 72 \times 72$ and $96 \times 96 \times 96$.

The streamwise and spanwise directions are discretized pseudo-spectrally, while the wall-normal direction is discretized with staggered second-order finite difference. Hence, in the AMD model, we adopt $C_1 = C_2 = 1/12$ and $C_3 = 0.30$ for the modified Poincaré constant (see section 2.2.3). The nonlinear terms are de-aliased in Fourier space using the 3/2 rule [21]. The time advancement is based on a second-order-accurate Adams-Bashforth scheme. In the streamwise and spanwise directions, periodic boundary conditions are applied. The upper boundary conditions are zero stress, zero flux, and zero vertical velocity. For the bottom surface, the standard wall-stress formulation based on the Monin-Obukhov similarity theory is employed [103].

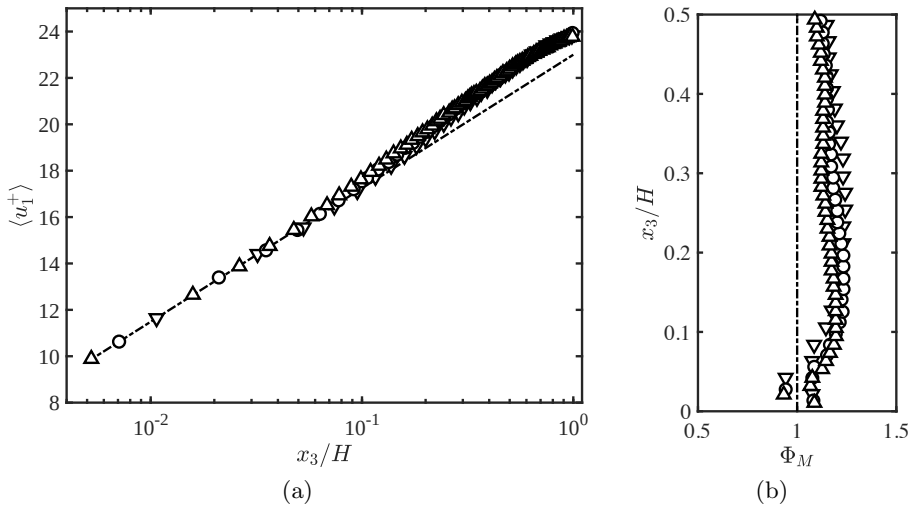

Figure 2.7: (a) Streamwise mean velocity profile and (b) Φ_M for grid resolutions $N_i = 48$ ($\triangledown$), 72 ($\bigcirc$), and 96 ($\triangle$). The logarithmic law profile and $\Phi_M = 1$ (·····) are plotted for comparison.

2.4.3 Results

Figure 2.7(a) shows the mean velocity profile obtained from the AMD model with different grid resolutions. The mean streamwise velocity gradient $\Phi_M = (\kappa x_3/u_*)(\partial\langle\bar{u}_1\rangle/\partial x_3)$, where κ is the von Kármán constant, is also plotted in Figure 2.7(b) as a function of height. For the homogeneous surface, the mean velocity is expected to be logarithmic in the surface layer, following $\langle u_1\rangle/u_* = (1/\kappa)\log(x_3/x_o)$, which occupies the bottom $10\% - 20\%$ of the simulation domain. The Φ_M predicted by the similarity theory is expected to have a constant value in the surface layer [18]. The AMD model accurately predicts the logarithmic profile for the mean streamwise velocity.

For the scalar concentration, since a constant surface flux is imposed as the boundary condition, it is more common to evaluate the mean scalar concentration gradient Φ_ϕ, defined as $(\kappa x_3/\phi_*)(d\langle\bar{\phi}\rangle/dx_3)$, instead of the actual value of the scalar concentration. For a passive scalar under neutral stratification, the value of Φ_ϕ has been reported to be 0.74 [18, 154] in the surface layer. The vertical profile of Φ_ϕ is presented in Figure 2.8(a). The values obtained from the AMD model show the expected behavior, and are comparable

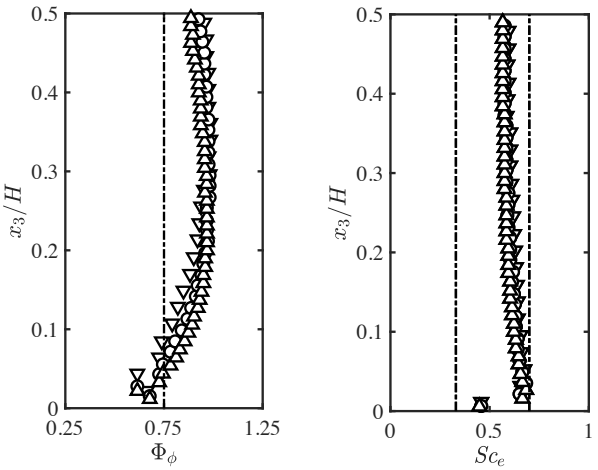

Figure 2.8: (a) Profiles of Φ_ϕ and (b) SGS Schmidt number for grid resolutions $N_i = 48$ ($\triangledown$), 72 ($\circ$), and 96 ($\triangle$). $\Phi_\phi = 0.74$ and $Sc_e = 0.33, 0.7$ (-·-·-).

to the reported trends using the scale-dependent DSM implementation [127, 153, 20] (not shown). The vertical distribution of the subgrid Schmidt number Sc_e is also shown in Figure 2.8(b). This is obtained by averaging the ratio of the eddy viscosity and eddy diffusivity in homogeneous directions and in time. In most LES with a passive scalar, the subgrid Schmidt number is chosen to be a fixed constant value between 0.33 and 0.7 [90, 156, 3]. As seen in this figure, the obtained value for the subgrid Schmidt number is consistent with those reported in previous studies. In addition, the results show very little sensitivity to the grid resolution.

Figure 2.9 depicts the resolved and subgrid profiles of the shear stress and wall-normal scalar flux, respectively. In the absence of viscous effects and under quasi-steady state conditions, the divergence of the total shear stress must balance the imposed pressure gradient. Also, the divergence of the total scalar flux must balance the rate of change in the scalar concentration. In this study, the boundary layer flow is driven by a constant streamwise pressure gradient, and a constant scalar flux is imposed at the surface. Therefore, the total shear stress and wall-normal scalar flux are both expected to have linear mean profiles [128, 127, 153]. As shown in these figures, the LES calculations with the AMD

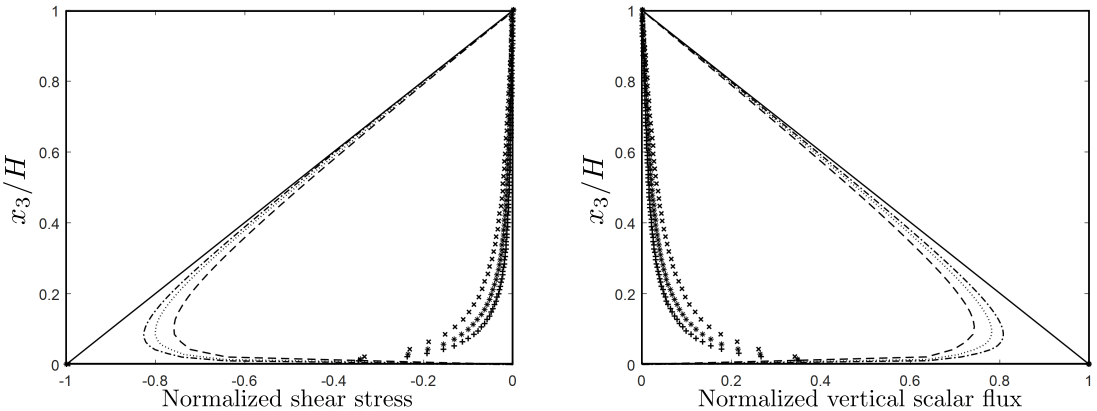

Figure 2.9: (a) Total and partial shear stress normalized by u_*^2, and the (a) total and partial wall-normal scalar flux normalized by Q_s. Total quantities given by solid line. The resolved and SGS quantities for $N_i = 48$ (- - -; $\times$), 72 (·····; $*$), and 96 (-·-·-; $+$).

model reproduces the linear profiles of the total turbulent fluxes which can serve as a confirmation of stationarity, and momentum and scalar flux conservation of the scheme [82]. The influence of spatial resolution is also depicted in these figures. As expected, the contribution of the resolved turbulent fluxes increases as the spatial resolution increases.

In a high-Reynolds-number turbulent boundary layer flow, it is well-known that the velocity and scalar spectra follow the Kolmogorov $-5/3$ power law in the inertial subrange ($k_1 x_3 > 1$, where k_1 is the streamwise wave number and x_3 is the distance to the wall) [137, 150]. In addition, in the energy-production range ($k_1 x_3 < 1$), the velocity spectrum is expected to follow a slope of -1 [118, 57, 59]. Figure 2.10 shows the spectra of the simulated streamwise velocity and scalar concentration, respectively. As demonstrated in these figures, for the small scales ($k_1 x_3 > 1$), the normalized spectra shows the expected collapse and follows the theoretical inertial subrange scaling with a slope of $-5/3$. For the scales larger than the distance to the wall ($k_1 x_3 < 1$), the slope of the velocity spectra is smaller and close to the expected value of -1. It is worth mentioning that, as reported in several studies, the Smagorinsky model yields spectra that decay faster and with higher slopes at the smallest resolved scale [3, 128, 17, 82]. In contrast, the slopes of the power spectra obtained from the DSM are too flat with an unrealistic pile-up for the scalar fluctuations at high wave

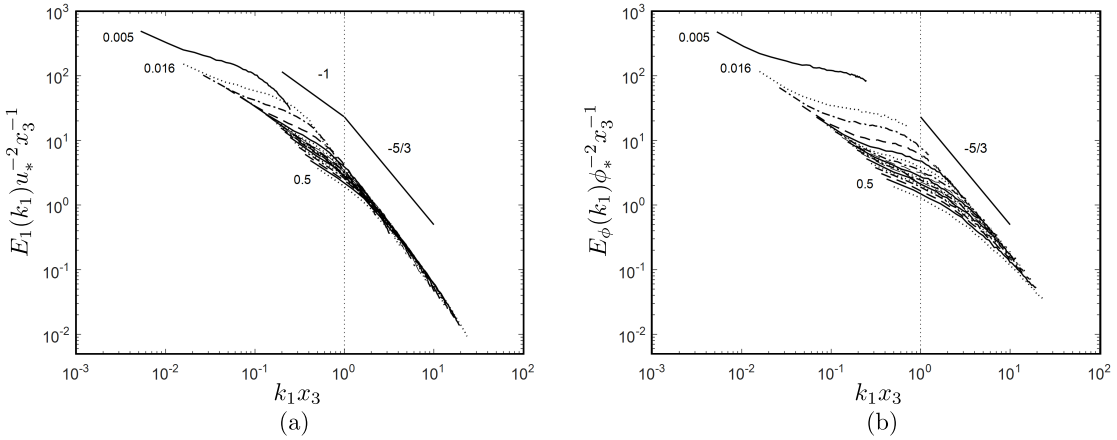

Figure 2.10: (a) Resolved streamwise velocity spectra and (b) resolved scalar concentration spectra obtained with $N_i = 96$ for different heights x_3/H from 0.005 to 0.5. The line $k_1x_3 = 1$ (·····) is plotted for reference.

numbers [127, 153]. The obtained results demonstrate that the AMD model accurately predicts the transfer of energy from the resolved scales to the subgrid scales at the proper rate.

2.5 Summary

The minimum-dissipation (MD) SGS model is investigated. The MD model gives the minimum eddy dissipation required to remove energy pile-up in the smallest resolved scales of the LES, and appropriately switches off for laminar and transitional flow. The model has low computational complexity and is consistent with the exact subgrid tensor on isotropic grids. The MD model gives satisfactory results in simulation of decaying grid turbulence on an isotropic grid. On anisotropic grids, however, the model is not consistent with the exact SGS tensor, and requires an approximation of the filter size. Results obtained with the MD model on anisotropic grids are highly sensitive to the filter size approximation, and neither of the two approximation tested give acceptable results in simulations of a temporal mixing layer and turbulent channel flow.

To address the shortcoming of the MD model, a modification for anisotropic grids was

proposed. The anisotropic minimum-dissipation (AMD) model appropriately switches off in laminar and transitional flow, and has low computational complexity. The model is consistent with the exact SGS tensor on both isotropic and anisotropic grids and does not require an approximation of the filter size. The AMD model gives accurate results in simulations of decaying grid turbulence on an isotropic grid and in simulations of a temporal mixing layer and turbulent channel flow with anisotropic grids. Thus, unlike the MD model, the AMD model is suitable for practical LES on anisotropic grids.

Additionally, the AMD model was extended to subgrid scalar flux for scalar transport equations. The AMD model for the SGS stress tensor and scalar flux was implemented in the simulation of a high-Reynolds-number boundary layer flow with a constant surface scalar flux. Simulation results obtained from the AMD model reveal good agreement with well-established empirical formulations and theoretical predictions of different flow statistics in a neutral boundary layer flow. Specifically, the AMD model produces mean velocity and scalar concentration profiles that are in good agreement with similarity theory in the surface layer. In addition, LES with the AMD model reproduces the expected power-law spectra for both velocity and scalar concentration.

Chapter 3

Error convergence of subgrid-scale models for large-eddy simulation in the outer region of wall-bounded flows*

3.1 Motivation

While LES enables a reduction of computational cost compared to DNS, the solutions provided by most LES approaches are grid-dependent, and multiple computations are required in order to faithfully assess the quality of the LES results. This brings the fundamental question of what is the expected LES error as a function of Reynolds number and grid resolution. The necessity of assessing the impact of grid resolution on both the accuracy and convergence properties of SGS models and flow statistics has been highlighted in the NASA Vision 2030 [145] as a pacing item for the computational fluid mechanics. The issue was also remarked by Pope [126] as a central problem concerning the foundations of LES.

*Part of the contents of this chapter have been submitted to *Journal of Computational Physics* with coauthor Adrián Lozano-Durán [79].

Therefore, LES must be framed in the context of a convergence study, and the associated grid requirements for different flow configurations must be determined for LES to be deemed as a cost-saving approach when compared with DNS. In the present work, we analyze the LES error scaling of the mean velocity profile, turbulence intensities, and energy spectra in the outer region of wall-bounded flows without the influence of the wall.

The equations for LES are formally derived by applying a low-pass filter to the Navier-Stokes equations [76]. The common procedure is then to solve these filtered equations together with a model for the SGS stresses, but no explicit filter form is usually specified. Instead, the discrete differentiation operators and limited grid resolution used to compute the LES solution are assumed to act as an effective implicit filter. The approach, usually referred to as implicitly-filtered LES, yields a velocity field that is considered representative of the actual filtered velocity with filter size proportional to the grid resolution. This lack of explicit filtering is responsible for the aforementioned intimate relation between the grid resolution and the LES equations [84, 15]. Grid convergence is only guaranteed in the limit of DNS-like resolution, and the LES predictions may be sensitive in an intricate manner to the grid size above such limit. This is a distinctive feature of implicitly-filtered LES which entails important difficulties for evaluating the quality of the solutions.

First studies aiming to assess the accuracy of SGS models include the pioneering investigation by Clark et al. [32], who established the numerical study of decaying isotropic turbulence as a reference benchmark, although the grid resolutions and Reynolds numbers tested were highly constrained by the computational resources of the time. Since then, common benchmarks for LES have broadened to include simple hydrodynamic cases such as forced or decaying isotropic turbulence [94], rotating homogeneous turbulence [65], spatial or temporal mixing layers [167, 168] and plane turbulent channel flow [122, 42, 28], among others. See Bonnet et al. [11] for an overview of cases for LES validation.

Analysis of numerical errors in LES by Ghosal [44], Kravchenko and Moin [69] and Chow and Moin [27] revealed that the magnitude of the numerical errors can be comparable to that of modeling errors, and Meyers et al. [97] showed that the partial cancellation of modeling and numerical errors can lead to coincidentally accurate results in isotropic turbulence.

Along the same line, Meyers et al. [98] studied the combined effect of discretization and model errors, and a further series of works resulted in the error-landscape-methodology framework reviewed by Meyers [95], where it is stressed that the determination of LES quality based on one single metric alone may provide misleading results. The performance of SGS models in the presence of walls has been found to be even more erratic. Meyers and Sagaut [96] presented the grid-convergence behavior of channel-flow DNS at resolutions typically encountered in subgrid-model testing. They observed a non-monotonous convergence of the skin friction and turbulence intensities with grid-refinements, suggesting that the robustness of SGS models should be tested for a range of Reynolds numbers and resolutions in order to avoid incidental coincidences with DNS results. At much higher Reynolds numbers, Sullivan and Patton [155] examined the numerical convergence of LES in time-dependent weakly sheared planetary boundary layers. They considered the convergence of the second-order statistics, energy spectra, and entrainment statistics and concluded that LES solutions are grid-independent provided that there is adequate scale separation between the energy-containing eddies and those near the filter cut-off scale. Stevens et al. [151] showed the ability of LES to reproduce accurately second and higher-order velocity moments for grid resolutions fine enough to resolve 99% of the LES kinetic energy. The convergence of SGS models in complex geometries has been explored in a lesser degree, but some noteworthy efforts are the pulsatile impinging jet in turbulent cross-flow by Toda et al. [159] and the full plane calculations by Lehmkuhl et al. [74, 75].

A central matter among the convergence studies above is the search for the most meaningful flow quantity to collapse the LES errors when the grid size, Reynolds number, and model parameters are systematically varied. Geurts and Fröhlich [43] characterized the simulation errors in terms of the subgrid-activity, defined as the relative subgrid-model dissipation rate with respect to the total dissipation rate. Klein [63] studied the accuracy of single-grid estimators for the unresolved turbulent kinetic energy to assess the quality of LES, and evaluated the sensitivity of the LES results on the modeling and numerical errors. Similarly, Freitag and Klein [41] presented a method to evaluate error contributions by assuming that the numerical and modeling errors scale like a power of the grid spacing

and filter size, respectively. Other indices to estimate the quality of the LES solution are the fraction of the total turbulent kinetic energy in the resolved motions [126], the relative grid size with respect to Kolmogorov or Taylor scales, or the effective eddy viscosity compared to the molecular viscosity [23]. Alternative and more sophisticated metrics are still emerging, such as the Lyapunov exponent measurement proposed by Nastac et al. [107] for assessing the dynamic content and predictability of LES among others, but there is a lack of consensus regarding which should be the most meaningful metric to quantify errors in a general set-up, if any.

We assess the error scaling of two SGS models based on the eddy viscosity assumption in the outer region of wall-bounded turbulence at moderately high Reynolds numbers. Our goal is to characterize the errors as a function of grid resolution and Reynolds number, and to find the physical length-scale dictating the relative size of the grid that is relevant for error quantification. For that purpose, we perform a theoretical estimation of the error scaling for the mean velocity profile, turbulence intensities, and kinetic energy spectra. Our results are corroborated by LES of turbulent channel flows using either a modified boundary condition or a wall model that acts as a surrogate of the near-wall dynamics by supplying the exact mean wall stress. It is important to remark that turbulent free shear flows such as mixing layers, jets, and wakes are also tenable candidates for studying shear-dominated flows away from walls. However, their large scales are dynamically different than the large scale motions of turbulent boundary layer flows typically relevant for external aerodynamics, which is the focus of this chapter.

The chapter is organized as follows. In section 3.2, we illustrate the near-wall behavior of SGS models in LES. We discuss the methodology and the numerical setup to assess the convergence of SGS models in section 3.3 without the physical constraint imposed by the wall. The results for the errors in the mean velocity profile are presented in section 3.4, for the turbulence intensities in section 3.5, and for the energy spectra in section 3.6. A relevant length-scale for local error quantification are discussed in section 3.7. Finally, a summary is offered in section 3.8.

3.2 The near-wall behavior of SGS models in LES

Most SGS models assume that a considerable fraction of the turbulent kinetic energy (i.e., 80-90% [126]) is resolved by the grid, and the Reynolds number and grid resolutions must comply with this requirement in order to faithfully assess the performance of the models. In unbounded flows like isotropic turbulence, LES can be performed at relatively coarse grid resolutions while still meeting this condition. On the contrary, this condition is not as favorable for wall-bounded flows. The number of grid points N to compute a turbulent boundary layer of thickness δ spanning a wall-parallel area of $L_1 \times L_3$ is

$$N = \int_0^{L_1} \int_0^{\delta} \int_0^{L_3} \frac{\mathrm{d}x_1 \mathrm{d}x_2 \mathrm{d}x_3}{\Delta_1 \Delta_2 \Delta_3}, \tag{3.1}$$

where x_1, x_2 and x_3 are the streamwise, wall-normal and spanwise directions, respectively, and Δ_1, Δ_2 and Δ_3 are the target grid resolutions in each direction that may be a function of space. Usually, the required number of grid points N can be expressed as a power of Reynolds number, where the exponent depends on the sizes of the eddies expected to be accurately represented by the grid. Estimations of the scaling can be found in Chapman [25] and Choi and Moin [26]. DNS aims to capture eddies in the dissipative range, and hence $\Delta_i \sim \eta$ and $N \sim Re^{37/14}$, where η is the Kolmogorov length-scale. To resolve the energy-containing eddies as in wall-resolved LES, it is necessary that $\Delta_i \sim L_\varepsilon$ which yields $N \sim Re^{13/7}$, where L_ε is the integral length-scale. In the logarithmic region of wall-bounded flows, L_ε grows linearly with x_2 and the energy-containing eddies have sizes proportional to the distance to the wall [51, 71]. Consequently, the LES grid must be accordingly reduced in all spatial directions to resolve a constant fraction of the turbulent kinetic energy, increasing the computational cost. Wall-resolved LES can be properly performed through nested grids [157, 70] such as the one depicted in Figure 3.1. Otherwise, the near-wall grid resolution does not suffice to capture the energy-containing eddies, and most SGS models perform poorly [54]. Finally, if we target to model only the outer motions as in wall-modeled LES, the grid requirements are such that $\Delta_i \sim \delta$, and N is at most linear with Reynolds number, depending on the wall model approach.

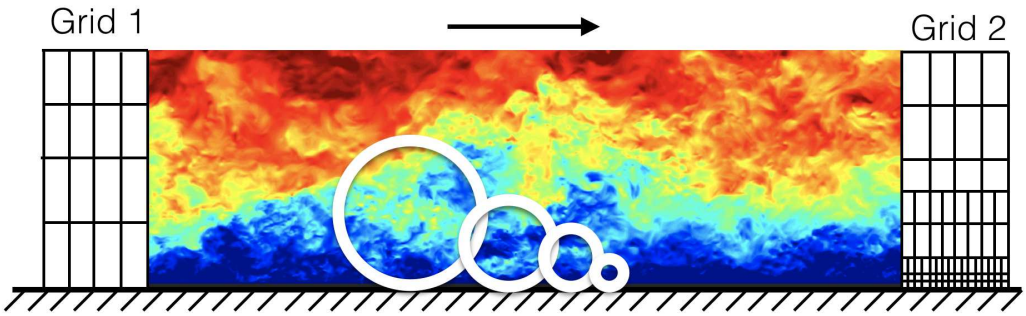

Figure 3.1: Instantaneous streamwise velocity contours of a turbulent channel flow and sketch of wall-attached eddies of different sizes. Grid 1 (left) depicts a uniform grid typical of wall-modeled LES. Grid 2 (right) is a nested grid necessary for wall-resolved LES.

Although wall-resolved LES has been practiced for a long time, actual wall-resolved LES is scarce. Typically, only the wall-normal resolution is properly refined according to the size of the energy-containing eddies, while the wall-parallel directions remain under-resolved. Most of the grid convergence studies in wall-bounded LES mentioned in Section 3.1 fall within this category as is the case of the channel flow simulation in Section 2.3.3. The consequence is that the majority of the validation studies in turbulent channel flows are at relatively low Reynolds numbers to make the computational cost of wall-resolved LES affordable [26]. However, it is questionable whether the SGS models are active enough in these conditions to adequately measure their performance, and even then it is unclear whether the near-wall region is sufficiently resolved in the wall-parallel directions.

Figure 3.2(a) shows the modeled SGS shear stress, τ_{12}^{SGS} for the dynamic Smagorinsky model (DSM) [42, 77] and anisotropic minimum dissipation (AMD) model [136] for the turbulent channel simulation in Section 2.3.3. It is clear that despite the satisfactory results in predicting the mean velocity profile (Figure 2.6a), the two SGS models show considerable differences in the prediction of SGS shear stress near the wall. This difference in the near-wall behavior can be neglected in relatively well-resolved low Reynolds number simulations, where the SGS contribution is small. However, with increasing Reynolds number and coarser grids, the discrepancy will become more significant, resulting in different statistics as shown

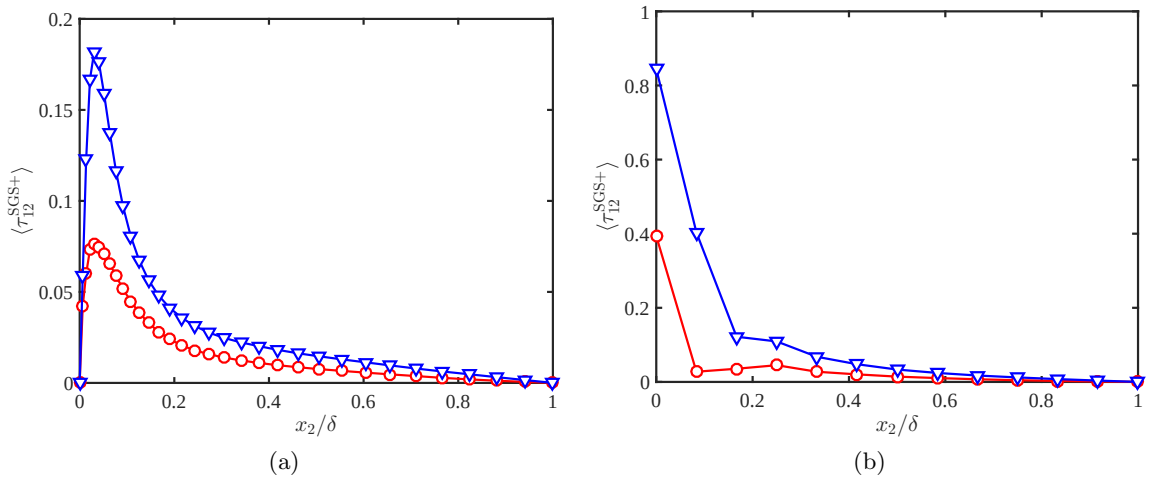

Figure 3.2: Subgrid-scale shear stress for the DSM (○) and AMD model (▽) for channel flow at (a) $Re_\tau \approx 550$, where the near-wall region is relatively well-resolved (Section 2.3.3), and (b) $Re_\tau \approx 950$, where the near-wall region is not resolved (Table 3.1).

in Figure 3.2(b) and Figure 3.3.

To illustrate the poor performance of SGS models when the near-wall region is under-resolved, Figure 3.3 shows the mean streamwise velocity profile, $\langle \bar{u}_1 \rangle$, for a turbulent channel flow as a function of the wall-normal distance x_2, where $\bar{(\cdot)}$ is the resolved LES field and $\langle \cdot \rangle$ denotes average in homogeneous directions and time. The fluctuating quantities will be denoted by $(\cdot)'$. The details of the simulations are discussed in Section 3.3.2 (see Table 3.1), but for now, it is only important to remark that all cases were computed using identical grids (with 13 points per channel half height, δ) and friction Reynolds number, $Re_\tau \approx 950$. Coarse DNS (no SGS model and no wall model) provides the worst prediction. Ideally, a perfect SGS model will supply the missing stresses at all distances from the wall. Indeed, Figure 3.3 shows that the solution improves by introducing SGS models (○ and ▽); however, the performance is still poor and the LES mean velocity profile is far from the reference DNS velocity profile. In contrast, the agreement with DNS is excellent when the correct mean wall stress is provided using a Neumann boundary condition (◇), despite the fact that there is no explicit SGS model in this case.

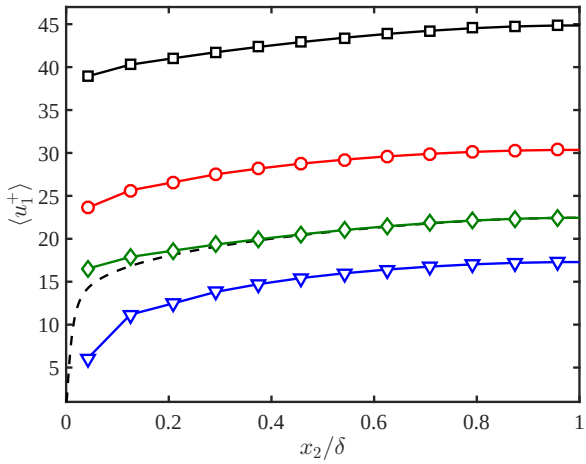

Figure 3.3: Mean streamwise velocity profile for NM950-NS (□), DSM950-NS (○), AMD950-NS (▽), and NM950-EWS (◇). DNS is given by (- - - ·).

Note that for all cases, the shape of $\langle \bar{u}_1 \rangle$ is barely affected in the outer region and always very close to the DNS mean velocity profile even when there is no SGS model due to the low Reynolds number. The main source of error comes from the inaccurate prediction of the wall friction velocity, u_τ, that translates into a vertical shift of $\langle \bar{u}_1 \rangle$. In particular, the two different SGS models applied show contrasting predictions of u_τ with the DSM underestimating and AMD model overestimating the DNS profile. The modeled SGS shear stress for the two different SGS models is given in Figure 3.2(b), which shows large differences near the wall, impacting predictions of wall shear stress. Note that due to the coarse grid resolutions at the wall, $\tau_{12}^{\mathrm{SGS}}|_w \neq 0$, contrary to what is typically assumed in wall-resolved LES. The result highlights the rarely mentioned fact that, for increasing Re or coarsening grid resolutions, wall models are necessary before SGS models, at least for prediction of the mean velocity profile in wall-bounded flows.

The problem would be alleviated by performing wall-resolved LES with three-dimensional refinement as the grid approaches the wall. However, this is not common in practice, and most attempts at wall-resolved LES suffer at some degree from the limitation demonstrated in Figure 3.3. Moreover, true wall-resolved LES is not cost-effective, as the grid requirement

scales as $Re^{13/7}$ [26]. Therefore, it is important to emphasize that in wall-bounded flows, the testing and validation of SGS is contaminated and dominated by the errors accumulated near the wall, and many of the mismatches of mean velocity profiles in DNS and LES reported in the literature are probably caused by the necessity of wall models before an SGS model. It is necessary to remark that we do not advocate for LES without an SGS model, but we only highlight the fact that validation at low Reynolds numbers could be limited due to inactive SGS models far from the wall and the predominance of the near-wall errors. Thus, when assessing an SGS model, it is important to distinguish its performance near the wall and far away from the wall. Provided that a wall model can circumvent the errors in the near-wall region, it becomes more important to assess the behavior of SGS models in the outer-region at high Reynolds numbers without the burden of the wall.

3.3 Benchmark for the outer region of wall-bounded turbulence

3.3.1 Slip-wall and exact-wall-stress turbulent channel flows

We consider a plane turbulent channel flow with periodic boundary conditions in the streamwise and spanwise directions. The incompressible LES equations obtained by applying a spatial filter to the Navier-Stokes equations are

$$\frac{\partial \tilde{u}_i}{\partial t} + \frac{\partial \tilde{u}_i \tilde{u}_j}{\partial x_j} = -\frac{1}{\rho}\frac{\partial \tilde{p}}{\partial x_i} + \nu \frac{\partial^2 \tilde{u}_i}{\partial x_j \partial x_j} - \frac{\partial \tau_{ij}}{\partial x_j}, \quad \frac{\partial \tilde{u}_i}{\partial x_i} = 0, \tag{3.2}$$

where $\tilde{u}_i$ for $i = 1, 2, 3$ are the streamwise, wall-normal and spanwise filtered velocities, respectively, $\tilde{p}$ is the filtered pressure, $\tau_{ij} = \widetilde{u_i u_j} - \tilde{u}_i \tilde{u}_j$ is the effect of the subgrid scales on the resolved eddies, ρ is the flow density, and ν is the kinematic viscosity. The wall units are defined by u_τ and ν, and the outer units by u_τ and δ, where u_τ is the friction velocity. The streamwise, wall-normal and spanwise spatial directions are x_i for $i = 1, 2, 3$, respectively, and the walls are located at $x_2 = 0$ and $x_2 = 2\delta$. The objective of LES modeling is to approximate τ_{ij} via the SGS tensor τ_{ij}^{SGS}. To emphasize that an LES model is not exact,

the resolved LES velocity is denoted by $\bar{u}_i$, and we expect that $\bar{u}_i \approx \tilde{u}_i$ for an accurate SGS model.

We discussed in Section 3.2 the necessity of benchmarks for wall-bounded turbulence that are independent of the strict near-wall resolution requirements. To attain this goal, we discuss two different approaches, namely, slip-wall (SLW) and exact-wall-stress (EWS) turbulent channel flows.

In slip-wall channel flow [78], the no-slip walls are replaced with the slip boundary condition with transpiration

$$u_i|_w = l \left.\frac{\partial u_i}{\partial n}\right|_w, \quad i = 1, 2, 3, \tag{3.3}$$

where the $(\cdot)|_w$ denotes quantities evaluated at the wall, n is the wall-normal direction oriented towards the interior of the channel, and l is the slip length, assumed to be constant. Note that Eq. (3.3) complies with the symmetries of the channel flow and the impermeability constraint of the wall on average.

The incompressible Navier-Stokes equations with boundary conditions in Eq. (3.3) is well-defined and has been solved by DNS for $Re_\tau \approx 550, 950$, and 2000 with $l = 0.1\delta$ [78]. Figure 3.4 compares DNS of the SLW channel and no-slip channel. First, note the contribution of the mean resolved Reynolds shear stress in Figure 3.4(a). The Reynolds shear stress accounts for more than 90% of the total stress for all cases and roughly 98% for $Re_\tau \approx 2000$ due to the ability of the boundary condition given by Eq. (3.3) to generate nonzero $\langle u_1 u_2 \rangle$ at the wall. The viscous stress contribution is less than 10% at all heights, including the near-wall region. Figure 3.4(d) shows the different characteristic flow length-scales for the DNS of the SLW channel and the no-slip channel flow, namely, the Kolmogorov scale $\eta = (\nu^3/\varepsilon)^{1/4}$ [125], the Taylor micro-scale $L_\lambda = (15\langle u_i' u_i' \rangle/\varepsilon)^{1/2}$ [158], the integral length-scale $L_\varepsilon = (\langle u_i' u_i' \rangle/6)^{3/2}/\varepsilon$ [125], and the shear length-scale $L_s = u_\tau(\partial\langle u_1 \rangle/\partial x_2)^{-1}$ [101], where ε is the rate of energy dissipation. The length-scales covered here no longer drop rapidly to zero as $x_2 \to 0$ for the SLW channel. Rather, they remains roughly constant in the near-wall region. Moreover, the integral length scale for the SLW cases collapse for

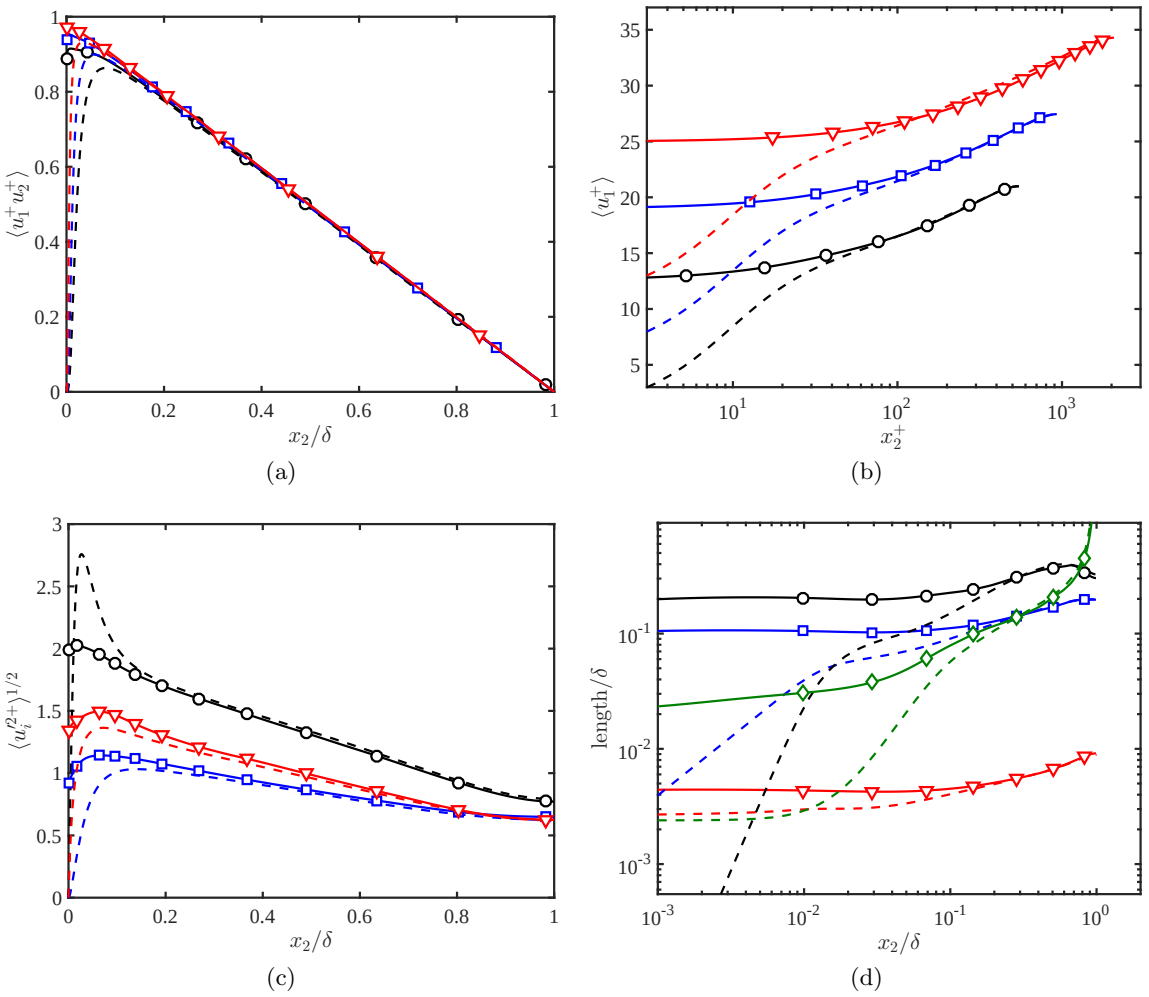

Figure 3.4: (a) Mean tangential Reynolds stress for slip-wall DNS of $Re_\tau \approx 550$ (○), $Re_\tau \approx 950$ (□), and $Re_\tau \approx 2000$ (▽). Corresponding no-slip DNS values (- - - -) are given in the respective colors. (b) Mean streamwise velocity profiles of SLW DNS at $Re_\tau \approx 550$ (○), $Re_\tau \approx 950$ (□), and $Re_\tau \approx 2000$ (▽). The mean velocity profiles for $Re_\tau \approx 950$ and 2000 are shifted 5 and 10 wall units, respectively, in the vertical direction for clarity. The corresponding no-slip DNS values (- - - -) are adjusted to match the center-line velocity of the SLW DNS and plotted in the corresponding color. (c) Streamwise (○), wall-normal (□), and spanwise (▽) rms velocity fluctuations and (d) Kolmogorov scale (▽), Taylor micro-scale (□), integral length-scale (○), and shear length-scale (◇) for slip-wall DNS of $Re_\tau \approx 550$. Corresponding no-slip DNS values (- - - -) are given in respective colors.

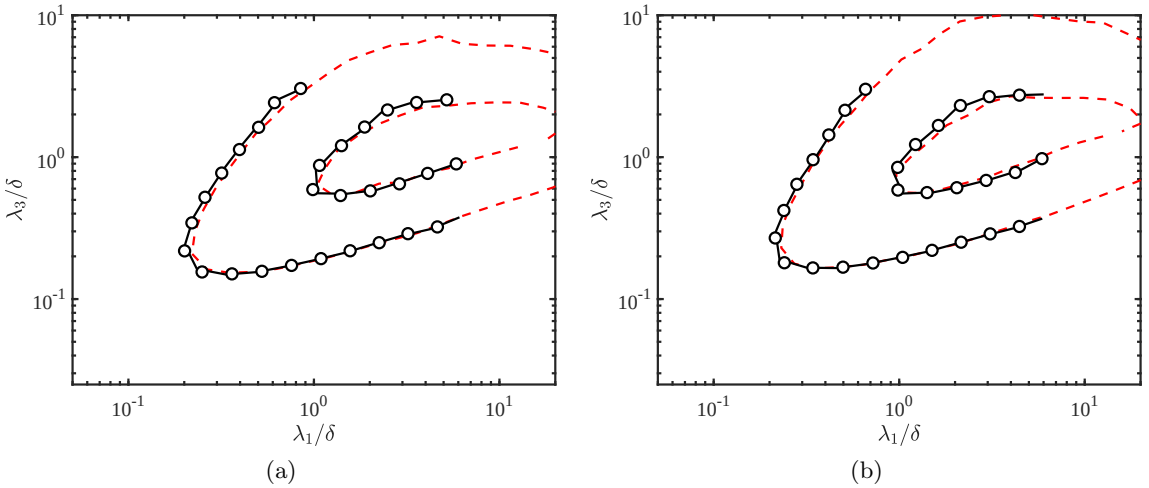

Figure 3.5: Wall-parallel premultiplied streamwise velocity spectra at (a) $x_2 = 0.5\delta$ and (b) $x_2 = 0.75\delta$ for SLW DNS (○) and no-slip DNS (- - - -) at $Re_\tau \approx 550$. Contours are 0.1 and 0.6 of the maximum.

different Reynolds numbers (not shown), demonstrating that it scales in outer-units across the entire boundary layer thickness. Thus, the boundary condition given by Eq. (3.3) suppresses the formation of near-wall viscous layers and breaks the linear scaling of eddies close to the wall. Moreover, it is also shown that in the outer layer, the first-order statistics and spectra of the SLW channel flow match quantitatively those of no-slip DNS simulations, as can be observed in Figures 3.4(b) and (c) and 3.5. Thus, the SLW channel flow is an excellent candidate to test the performance of SGS models in the outer region of the flow.

The second approach is the EWS turbulent channel flow, where the no-slip boundary condition at the wall is replaced by an EWS condition imposed through a Neumann boundary condition

$$\left.\frac{\partial \bar{u}_1}{\partial n}\right|_w = \frac{\tau_w - \tau_{12}^{\mathrm{SGS}}\big|_w}{\nu}, \tag{3.4}$$

where τ_w is the mean wall stress known *a priori* from DNS such that Eq. (3.4) can be thought of as a perfect wall-model. It has been shown before that for wall-modeled LES, imposing the correct mean wall stress is sufficient to predict one-point statistics accurately [72].

Case	SGS model	Wall condition	Re_τ	Δ_1/δ	Δ_2/δ	Δ_3/δ
NM950-NS	NM	NS	934	0.10	0.080	0.050
DSM950-NS	DSM	NS				
AMD950-NS	AMD	NS				
NM950-EWS	NM	EWS				

Table 3.1: List of cases used in section 3.2. The second column contains the SGS model: no explicit SGS model (NM) or dynamic Smagorinsky model (DSM). The third column refers to the wall boundary condition: no-slip (NS) or the exact-wall-stress (EWS) condition. The fourth column indicates the friction Reynolds number. Δ_1, Δ_2 and Δ_3 are the streamwise, wall-normal and spanwise grid resolutions respectively.

The set-up of the two benchmark cases above is not intended to capture the near-wall dynamics, and the small eddies close to the wall are prone to be misrepresented for coarse grid resolutions. However, our focus is on outer flow along the range $0.2\delta < x_2 < \delta$ [125], and previous studies have revealed that this region can survive independently of the particular configuration of the eddies closest to the wall, even if they are partially or completely under-resolved. Some examples are the roughness experiments in channels and boundary layers [117, 50, 9, 39, 40], and the idealized numerical studies by Flores and Jiménez [39], Mizuno and Jiménez [102], Chung et al. [30], Lozano-Durán and Bae [78], among others. In all these cases, the near-wall region was seriously modified or directly bypassed, but the properties of the outer layer remained essentially unaltered. Therefore, the correct representation of the outer layer dynamics remains uncoupled from the inner layer structure, supporting the numerical experiment presented here as a valid framework to assess LES errors far from the wall.

3.3.2 Numerical experiments

We perform two sets of LES of plane turbulent channels for the SLW and EWS approaches.

The simulations are computed with a staggered second-order finite difference [110] and fractional-step method [62] with a third-order Runge-Kutta time-advancing scheme [176]. The flow is either driven by imposing a constant mean pressure gradient for the SLW cases

Grid resolution label	Δ_1/δ	Δ_2/δ	Δ_3/δ
i1	0.20	0.20	0.20
i2	0.10	0.10	0.10
i3	0.050	0.050	0.050
i4	0.025	0.025	0.025
a1	0.20	0.10	0.05
a2	0.10	0.10	0.07
a3	0.20	0.10	0.10

Table 3.2: Tabulated list of resolutions in outer units. The first column contains the label used to name LES cases computed with different grids. Δ_1, Δ_2 and Δ_3 are the streamwise, wall-normal and spanwise grid resolutions, respectively.

or a constant mass flux for the EWS cases. Periodic boundary conditions are imposed in the streamwise and spanwise directions, while for the top and bottom walls we use either the no-slip (NS) boundary condition, SLW boundary condition from Eq. (3.3) with $l = 0.1\delta$ for the SLW cases, or EWS Neumann boundary condition from Eq. (3.4).

Two SGS models are investigated: DSM and AMD, which are regarded as representative eddy viscosity models with and without test filtering, respectively. We will also consider cases without any explicit SGS model (NM).

The size of the channel is $8\pi\delta \times 2\delta \times 3\pi\delta$ in the streamwise, wall-normal and spanwise directions, respectively for both SLW and EWS cases. The grid resolutions are denoted by Δ_1, Δ_2, and Δ_3 for the respective spatial directions. We use a wide range of grid resolutions spanning from $\sim 0.01\delta$ to $\sim 0.2\delta$ that are characteristic of wall-modeled LES and fall within the recommendations by Chapman [25] for resolving the large eddies in the outer portion of the boundary layer. For the SLW cases, three different friction Reynolds numbers $Re_\tau = u_\tau\delta/\nu \approx 550, 950$, and 2000 are considered and compared to DNS from Lozano-Durán and Bae [78]. For the EWS cases, four different friction Reynolds numbers $Re_\tau \approx 950, 2000, 4200$ and 8000 are considered. These are compared with reference DNS data from Hoyas and Jiménez [48], Lozano-Durán and Jiménez [80], and Yamamoto and Tsuji [177]. All the LES channel flow simulations were run for at least 100 eddy-turnover times, defined as δ/u_τ, after transients.

The list of cases used to motivate the need of wall models in section 3.2 is given in Table 3.1. The simulations discussed for the remainder of the chapter are named following the convention [SGS model][Re_τ]-[boundary condition]-[grid resolution], where the grid resolutions are denoted by either by i1, i2, i3 and i4 for isotropic grids, and by a1, a2 and a3 for anisotropic grids. The different grid resolutions are provided in Table 3.2.

3.4 Error scaling of the mean velocity profile

The mean velocity profile is examined first as it is the figure of merit for most LES studies. We will assume that $\langle u_1 \rangle \approx \langle \tilde{u}_1 \rangle$ and, hence, the LES mean velocity can be directly compared with unfiltered DNS data. The approximation is reasonable in most cases where the quantity averaged is dominated by large-scales, as is the case for the mean velocity profile. In particular, the error for the mean velocity profile is systematically quantified as the average difference between the LES solution and the corresponding DNS in the outer region as

$$\mathcal{E}_m = \left[\frac{\int_{0.2\delta}^{\delta} \left(\langle \bar{u}_1 \rangle - \langle u_1 \rangle \right)^2 \mathrm{d}x_2}{\int_{0.2\delta}^{\delta} \langle u_1 \rangle^2 \mathrm{d}x_2} \right]^{1/2}, \tag{3.5}$$

where $\langle u_1 \rangle$ is evaluated from DNS data. This choice excludes the nonphysical/under-resolved range $x_2 < 0.2\delta$ for the LES cases as discussed in section 3.3. For a channel flow driven by constant mass flux and exact mean wall-stress, some reference errors at $Re_\tau \approx 4200$ can be obtained from two extreme cases, i.e., a fully turbulent profile defined by the flat velocity $\langle \bar{u}_1 \rangle = Q/2\delta$, and the laminar solution represented by the parabolic function $\langle \bar{u}_1 \rangle = 3Q/(4\delta)(2 - x_2/\delta)(x_2/\delta)$, whose errors are $\mathcal{E}_{m,\mathrm{turb}} \approx 0.06$ and $\mathcal{E}_{m,\mathrm{lam}} \approx 0.26$, respectively.

In general, the error will depend on the grid resolution and Reynolds number,

$$\mathcal{E}_m = \mathcal{E}_m(\Delta_1, \Delta_2, \Delta_3, Re_\tau), \tag{3.6}$$

and if we further assume that $\mathcal{E}_m \sim \Delta^{\alpha_m} Re_\tau^{\gamma_m}$, where Δ is a (yet to be defined) measure

of the grid size, the exponents α_m and γ_m can be theoretically estimated from the error equation and empirically computed from numerical experiments. Both analyses are performed below. We will conclude that LES is a viable approach for computing the outer flow of wall-bounded flows if the empirical values of the exponents are such that $\alpha_m > 0$ and $\gamma_m \approx 0$.

3.4.1 Theoretical estimations

We estimate the expected error behavior of $\mathcal{E}_m$ for a generic SGS model that will serve as a reference for the numerical observations in the next section. Let us consider the exact relation between the LES and DNS velocities at a location x_2 obtained from the integrated mean momentum equation for $\tilde{u}_1$ and u_1,

$$[\langle\tilde{u}_1\rangle - \langle u_1\rangle](x_2) = \langle\tilde{u}_1\rangle(0) + \frac{1}{\nu}\int_0^{x_2} \langle\tilde{u}_1'\tilde{u}_2' - u_1'u_2' + \tau_{12}\rangle \mathrm{d}x_2''. \tag{3.7}$$

For a symmetric filter with well-defined non-zero second moment in real space, τ_{12} can be written as [174]

$$\tau_{12} \approx \frac{\partial\tilde{u}_1}{\partial x_i}\frac{\partial\tilde{u}_2}{\partial x_i}\tilde{\Delta}_i^2 + \mathcal{O}(\tilde{\Delta}_i^2\tilde{\Delta}_i^2), \tag{3.8}$$

where repeated indices imply summation, and $\tilde{\Delta}_i$ signifies the filter size in the i-th direction defined as the square root of the second moment of the filter operator

$$\tilde{\Delta}_i^2 = \int_{-\infty}^{\infty}\int_{-\infty}^{\infty}\int_{-\infty}^{\infty} x_i^2\mathcal{G}(x_1,x_2,x_3)\mathrm{d}x_1\mathrm{d}x_2\mathrm{d}x_3, \tag{3.9}$$

where $\mathcal{G}$ is the filter kernel. For the rest of the section, we will neglect terms of the order of $\mathcal{O}(\tilde{\Delta}_i^4)$, namely, we assume that traditional SGS models are a fourth order approximation to τ_{ij}. The simplification will be useful for estimating the error scaling independently of any particular SGS model.

Analogously, the difference of the filtered and unfiltered fluctuating tangential stresses

can be approximated by

$$\tilde{u}_1'\tilde{u}_2' - u_1'u_2' \approx \frac{\tilde{\Delta}_i^2}{2}\left(\tilde{u}_1'\frac{\partial^2\tilde{u}_2'}{\partial x_i^2} + \tilde{u}_2'\frac{\partial^2\tilde{u}_1'}{\partial x_i^2}\right). \tag{3.10}$$

From Eqs. (3.7), (3.8) and (3.10), the error in the mean velocity profile can be shown to be

$$\mathcal{E}_m \sim [\langle\tilde{u}_1\rangle - \langle u_1\rangle](x_2) \sim \int_0^{x_2}\left\langle \tilde{\Delta}_i^2\frac{\partial\tilde{u}_1}{\partial x_i}\frac{\partial\tilde{u}_2}{\partial x_i} + \frac{\tilde{\Delta}_i^2}{2}\left(\tilde{u}_1'\frac{\partial^2\tilde{u}_2'}{\partial x_i^2} + \tilde{u}_2'\frac{\partial^2\tilde{u}_1'}{\partial x_i^2}\right)\right\rangle \mathrm{d}x_2''. \tag{3.11}$$

Note that the filter sizes in Eq. (3.11) are arranged such that $\mathcal{E}_m \sim (\tilde{\Delta}_i\tilde{\Delta}_i)^{\alpha_m/2}$, which motivates the use of the L_2-norm of $(\Delta_1, \Delta_2, \Delta_3)$ as the characteristic grid-size, with $\Delta_i \sim \tilde{\Delta}_i$. Eq. (3.11) also shows that Δ_i do not provide a full description of the error, and that a complete characterization will involve an effective grid size that is flow dependent (given by Eq. (3.11)).

Equation (3.11) can be further exploited to determine the scaling of $\mathcal{E}_m$ with Δ by approximating the dependence of $\tilde{u}_i'$, $\partial^2\tilde{u}_j'/(\partial x_i\partial x_i)$ and $\partial\tilde{u}_j/\partial x_i$ on Δ. A rough estimation may be performed by assuming a kinetic energy spectrum $E_K \sim k^\beta$, with the wavenumber $k \sim 1/\Delta$, and the isotropic velocity gradient $G = \partial u/\partial x$ at scale Δ such that

$$\tilde{u}_{1,2}'\frac{\partial^2\tilde{u}_{2,1}'}{\partial x_i\partial x_i}, \frac{\partial\tilde{u}_1}{\partial x_i}\frac{\partial\tilde{u}_2}{\partial x_i} \sim G^2 \sim \frac{u^2}{\Delta^2} \sim \frac{kE_K}{\Delta^2} \sim \Delta^{-(\beta+3)}, \tag{3.12}$$

where the exponent β depends on the regime the SGS models operates; for the shear-dominated range $\beta = -1$ [117] and $G^2 \sim \Delta^{-2}$, whereas for the inertial range $\beta = -5/3$ [67] and $G^2 \sim \Delta^{-4/3}$. Taking into account the scaling above and after integration of the right-hand-side in (3.11), the expected error in the LES mean velocity profile should scale as

$$\mathcal{E}_m^{\mathrm{sh}} \sim \Delta, \quad \mathcal{E}_m^{\mathrm{in}} \sim \Delta^{5/3}, \tag{3.13}$$

for SGS models acting on the shear-dominated or inertial regimes, respectively. The scaling of $\mathcal{E}_m$ with Δ in (3.13) can be estimated from simpler dimensional arguments without going through (3.11), but it was beneficial to write the explicit equation of the error to obtain

more information about its functional form. Nevertheless, it is important to remark that (3.13) should be understood as a rough estimation since the actual errors evolve according to a non-linear equation and, hence, their rigorous mathematical treatment is highly elusive. This consideration is also applicable to the error estimations for the turbulence intensities and energy spectra in the later sections.

3.4.2 Numerical assessment

Figure 3.6(a) contains the mean velocity profiles for three SLW cases at $Re_\tau \approx 2000$ with AMD for different grid resolutions. As expected, $\langle \bar{u}_1 \rangle$ converges to $\langle u_1 \rangle$ as the grid is refined. The quantitative assessment of the $\mathcal{E}_m$ for $Re_\tau \approx 550, 950$, and 2000 of the SLW cases is shown in Figure 3.6(b) as a function of the characteristic grid resolution Δ, taken to be

$$\Delta = \sqrt{\frac{\Delta_1^2 + \Delta_2^2 + \Delta_3^2}{3}}. \tag{3.14}$$

as motivated by Eq. (3.11). The error roughly follows

$$\mathcal{E}_m \sim \left(\frac{\Delta}{\delta}\right)^{\alpha_m} \tag{3.15}$$

with α_m between the values of 1 and 5/3, which is consistent with the scaling given by theoretical assessment in section 3.4.1. The constant prefactor is model and Reynolds number dependent. For a given Δ, the error increases from $Re_\tau \approx 550$ to $Re_\tau \approx 950$, but shows signs of saturation at $Re_\tau \approx 2000$, which may be an indication that the constant prefactor will remain constant for higher Reynolds numbers. Both DSM and AMD model yield comparable errors. Figure 3.6(b) also includes two cases equivalent to AMD550-SLW-i3,i4 but without an explicit SGS model. The error is comparable to, but slightly larger than, the cases with SGS model. Other cases without SGS models for various grid resolutions and Reynolds numbers were computed and their accompanying errors were scattered within the range provided by Eq. (3.15) (not shown). This is a symptom that, despite the desirable properties of the SLW channel flow as a benchmark for LES, the span of Reynolds numbers

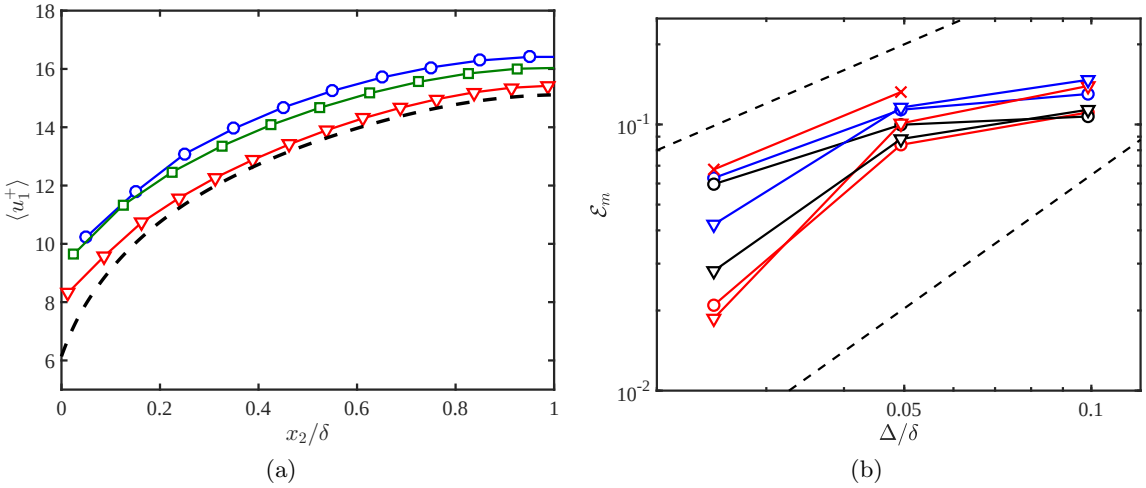

Figure 3.6: (a) Mean streamwise velocity profile for AMD2000-SLW-i2 (○), AMD2000-SLW-i3 (□) and AMD2000-SLW-i4 (▽). The SLW DNS for $Re_\tau \approx 2000$ is given by (- - - ·). (b) Error in the mean velocity profile of the SLW cases given as a function of the characteristic grid resolution for different SGS models (DSM, ○; AMD model, ▽; and no SGS model, ×) and Re_τ (550, ——; 950, ——; and 2000, ——). Reference lines are $\mathcal{E}_m \sim \Delta/\delta$ and $(\Delta/\delta)^{5/3}$ (- - - ·).

examined here is too small to scrutinize the effect of the SGS models and offer unambiguous conclusions. Higher Reynolds number SLW DNS were not available for comparison, so EWS cases are utilized to examine the effect of SGS models at high Reynolds numbers ($Re_\tau \approx 4200, 8000$).

Figure 3.7 shows the mean velocity profiles for a selection of EWS cases at $Re_\tau \approx 4200$ without SGS model (Figure 3.7a) and with DSM (Figure 3.7b) for different grid resolutions. Similar to the SLW cases, $\langle \bar{u}_1 \rangle$ converges to $\langle u_1 \rangle$ as the grid is refined for cases with DSM (equivalently for AMD), while the trend is inconsistent for cases without explicit SGS model. The quantitative assessment of the $\mathcal{E}_m$ is shown in Figure 3.8(a) as a function of the characteristic grid resolution Δ. Other grid definitions were also inspected in Figure 3.8(b) such as the cube root of the cell volume [34, 140], the maximum of the grid sizes [149], or the square root of the harmonic mean of the squares of the grid sizes, among others. However, the best collapse is achieved for Eq. (3.14), in accordance with the discussion in section

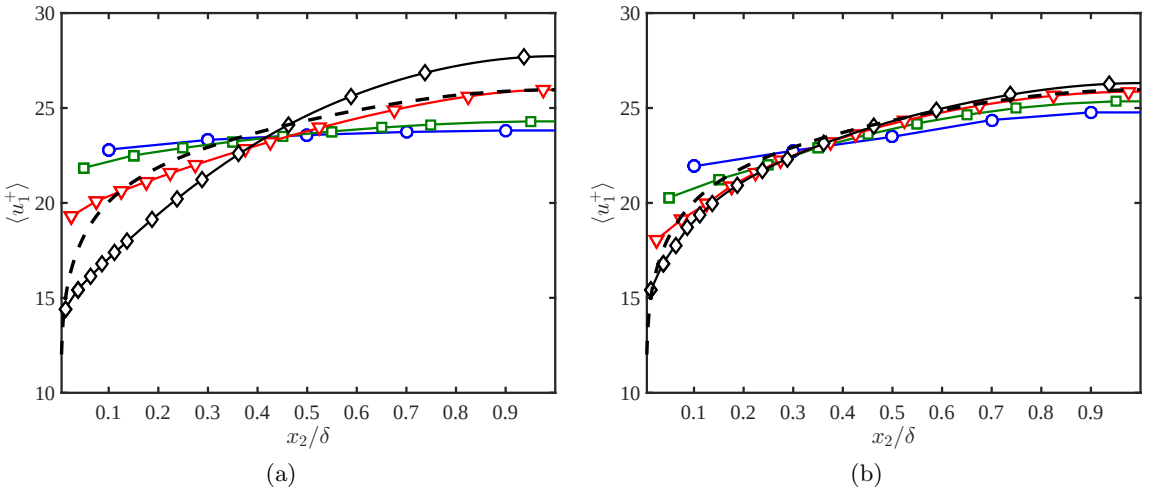

Figure 3.7: Mean streamwise velocity profile for EWS cases at $Re_\tau \approx 4200$ for (a) no explicit SGS model, and (b) DSM for grids i1 (○), i2 (□), i3 (▽), and i4 (◇) from Table 3.2. The DNS is given by (- - -).

3.4.1. A survey of existing subgrid length-scales can be found in Trias et al. [161] but note that in the current study we are discussing the most meaningful grid size to characterize $\mathcal{E}_m$, that differs from the characteristic length-scale embedded in SGS models (i.e., $\tilde{\Delta}$ in the Smagorinsky model $-2C_s\tilde{\Delta}^2\sqrt{2\bar{S}_{nm}\bar{S}_{nm}}\bar{S}_{ij}$, where $\bar{S}_{ij}$ is the resolved rate-of-strain tensor and C_s is the Smagorinsky coefficient).

The errors for cases without SGS model are discernibly larger than those calculated with DSM or AMD, especially for the finer grid resolutions, and similar to those for fully turbulent flows ($\mathcal{E}_{m,\text{turb}} \approx 0.06$). Moreover, they follow a non-monotonic behavior with Δ, inconsistent with the second-order prediction from the linear analysis of the spatial discretization errors, probably because such an approximation only holds for $\Delta \to 0$ and is no longer representative of errors subjected to non-linear diffusion and convection as expected for $\Delta \sim \delta$. Visual inspection of the instantaneous streamwise velocity fields for cases without SGS model in Figure 3.9 shows that there is a substantial change in the flow topology at $\Delta \approx 0.05\delta$. For $\Delta > 0.05\delta$, the velocity field lacks the characteristic turbulence features and exhibits instead a highly disorganized structure (Figures 3.9a-c). On the other

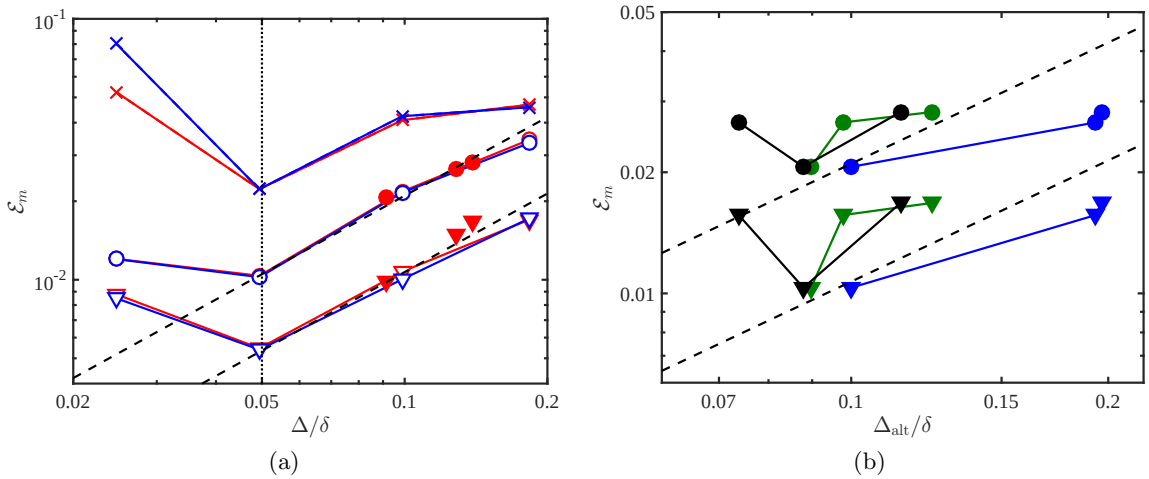

Figure 3.8: (a) Error in the mean velocity profile of the EWS cases as a function of the characteristic grid resolution for different SGS models (DSM, ○; AMD model, ▽; and no SGS model, ×) and Re_τ (4200, ——; 8000, ——). Open and closed symbols are for isotropic and anisotropic grids, respectively. Reference lines are $\mathcal{E}_m = 0.107\Delta/\delta$ and $\mathcal{E}_m = 0.210\Delta/\delta$ (- - - -) and $\Delta/\delta = 0.05$ (·····). (b) Error in the mean velocity profile for $Re_\tau \approx 4200$ as a function of alternate definition of characteristic grid resolution $\Delta_{\rm alt} = \sqrt[3]{\Delta_1\Delta_2\Delta_3}$ (green), $\Delta_{\rm alt} = \max(\Delta_1, \Delta_2, \Delta_3)$ (blue), and $\Delta_{\rm alt} = \sqrt{3/(1/\Delta_1^2 + 1/\Delta_2^2 + 1/\Delta_3^2)}$ (black). The symbols and reference lines (- - - -) are as in (a).

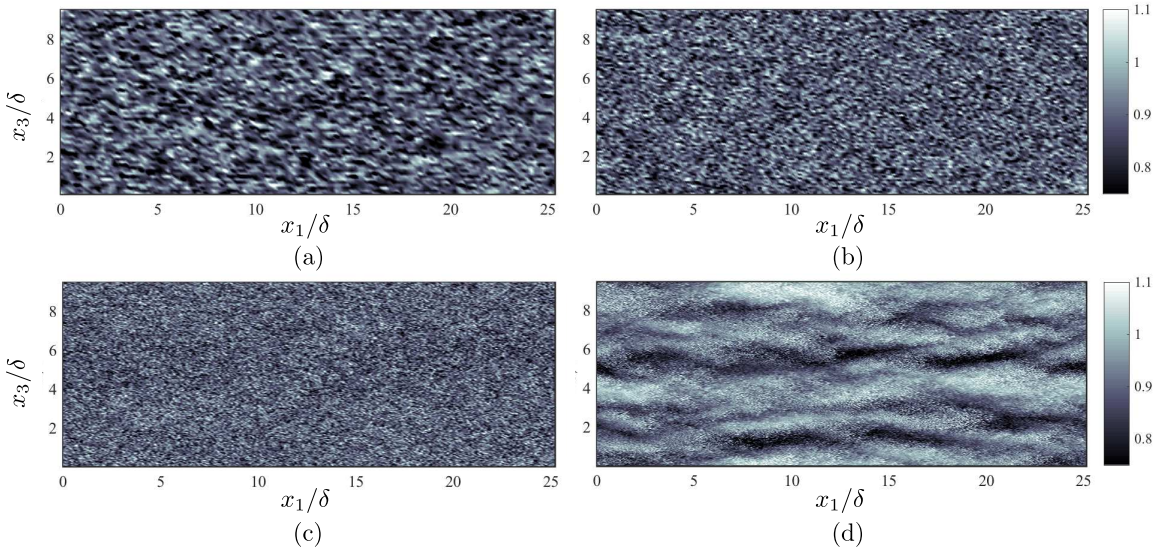

Figure 3.9: Instantaneous snapshots of the streamwise velocity in wall-parallel plane at $x_2 \approx 0.5\delta$ for (a) NM4200-EWS-i1, (b) NM4200-EWS-i2, (c) NM4200-EWS-i3, and (d) NM4200-EWS-i4.

hand, clearly defined streamwise velocity streaks emerge for $\Delta < 0.05\delta$ (Figure 3.9d). The physical justification for the existence of this critical grid resolution is relegated to the spectra analysis in section 3.6, but for now we can argue that these streaks are nonphysical in the sense that they worsen the mean velocity profile prediction as shown in Figure 3.7(a) for NM4200-EWS-i4. This suggest that the errors reported in Figure 3.8(a) should be separated into two different regimes delimited by $\Delta = 0.05\delta$.

For cases with SGS model and $\Delta > 0.05\delta$, the error follows

$$\mathcal{E}_m \sim \left(\frac{\Delta}{\delta}\right) Re_\tau^0 \tag{3.16}$$

for different SGS models. The results show that the LES solution convergences to the correct value free from viscous effects, $\mathcal{E}_m \sim Re_\tau^0$ (given a perfect wall model) as demanded from a proper LES far from the walls. Our results also suggest that $\mathcal{E}_m \sim \Delta$, which agrees with the theoretical estimation $\mathcal{E}_m^{\text{sh}}$ discussed in section 3.4.2. Although both DSM and AMD converge at the same rate with Δ, the prefactor can play an important role in the

error magnitude and thus different models may be preferred.

For $\Delta < 0.05\delta$, the errors depart from $\mathcal{E}_m \sim \Delta$ and saturate, probably due to the same effect that generates the nonphysical flow structures discussed in Fig. 3.9. However, further refinement of the grid show an augmented $\mathcal{E}_m \sim \Delta$ convergence (not shown). Therefore, the convergence of $\langle \bar{u}_1 \rangle$ to the DNS solution may entail an intricate non-monotonic response as reported in Meyers and Sagaut [96] for grids much finer than those typical of wall-resolved LES.

Alternative metrics to functionally quantify $\mathcal{E}_m$ are the resolved turbulent kinetic energy,

$$K_{\text{res}} = \frac{\langle \bar{u}_i \bar{u}_i \rangle}{\langle u_i u_i \rangle}, \tag{3.17}$$

and the SGS activity parameter [43, 97],

$$\varsigma = \frac{\langle 2\nu_e \bar{S}_{ij} \bar{S}_{ij} \rangle}{\langle 2\nu_e \bar{S}_{ij} \bar{S}_{ij} + 2\nu \bar{S}_{ij} \bar{S}_{ij} \rangle}, \tag{3.18}$$

where ν_e is the eddy viscosity. The results are shown in Figure 3.10 where K_{res} and ς are averaged over the wall-normal range $[0.3\delta, \delta]$. Despite the coarse grid resolutions investigated, the resolved kinetic energy remains above 90% for all cases (Figure 3.10a) and emerges as an effective metric to assess the errors in the mean profile, even among different SGS models. The result is not surprising since K_{res} can be easily related to $\mathcal{E}_m$ if we assume that $\langle u_1^2 \rangle / \langle u_i^2 \rangle \gg 1$ for $i = 2, 3$, and $\langle u_i^2 \rangle \approx \langle u_i \rangle^2$. The former are usually $\sim$100 for $0.3\delta < x_2 < \delta$, and the last condition is reasonably well satisfied if u_1 is close to a normal distribution $\mathcal{N}(\mu, \sigma)$ with mean μ and standard deviation σ such that $\mu/\sigma \gg 1$, that can shown to be the case for high-Reynolds-number turbulent channel flows. Under those conditions, the resolved kinetic energy can be expressed as

$$K_{\text{res}} \approx (1 - \mathcal{E}_m)^2, \tag{3.19}$$

which is included in Figure 3.10(a) and shows an excellent agreement with the data. Therefore, $\mathcal{E}_m$ and K_{res} are interchangeable metrics for characterizing errors in $\langle \bar{u}_1 \rangle$. Cases with

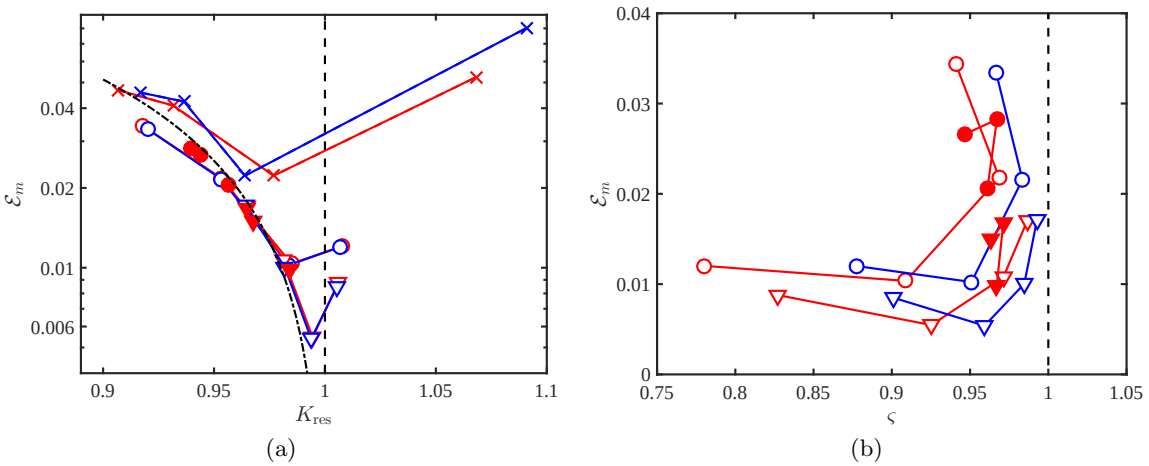

Figure 3.10: Error in the mean streamwise velocity profile of the EWS cases as a function of the (a) resolved total kinetic energy and (b) SGS activity parameter for different SGS models (DSM, ○; AMD model, ▽; and no SGS model, ×) and Re_τ (4200, ——; 8000, ——). Open and close symbols are for isotropic and anisotropic grids, respectively. The reference lines are $K_{\text{res}} \approx (1 - \mathcal{E}_m)^2$ (-·-·-) and $K_{\text{res}} = 1$ and $\varsigma = 1$ (- - -).

no explicit model does not follow the trend, and K_{res} can even exceed unity due to non-physical velocity fluctuations whose origin is discussed in more detail in section 3.5. The SGS activity is plotted in Figure 3.10(b). Increasing ς is associated with increasing $\mathcal{E}_m$, although the results are Reynolds number and SGS model dependent and do not collapse for isotropic and anisotropic grids. Nevertheless, Eq. (3.18) does not require DNS data, and it is a more realistic estimator for practical applications where the reference DNS solution is not available.

3.5 Error scaling of turbulence intensities

In this section, we study the theoretical and numerical convergence of the LES turbulence intensities in wall-bounded flows. In the previous section we have measured the errors on $\langle \bar{u}_1 \rangle$ by assuming that LES and DNS are directly comparable. The assumption is reasonable if the filtering operation has little impact on the mean of a variable ϕ, that is, $\langle \tilde{\phi} \rangle \approx \langle \phi \rangle$, and

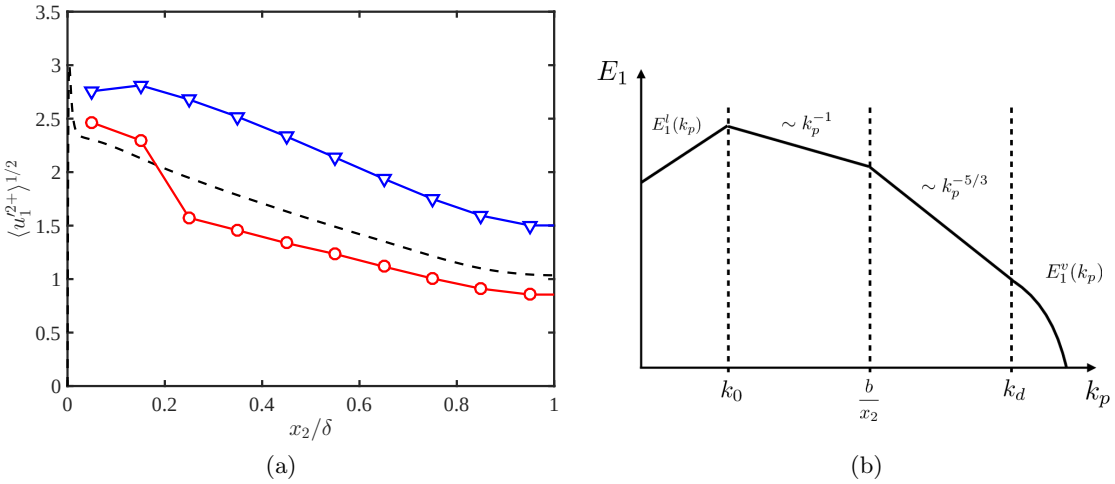

Figure 3.11: (a) Streamwise rms velocity fluctuations at $Re_\tau \approx 4200$ for NM4200-EWS-i2 (▽), DSM4200-EWS-i2 (○), and DNS (- - - -). (b) Model spectrum for the streamwise turbulence intensity. The wavenumbers k_0, b/x_2, and k_d mark transition from the large-scale to shear-dominated to inertial to viscous regimes.

this is the case for the mean velocity profile even with coarse filter sizes. However, smaller-scale motions play a non-negligible role in $\langle u_i'^2 \rangle$, casting doubts on how to compare fairly LES and DNS. If LES is formally interpreted by means of a spatial low-pass filter [34, 76], the meaningful quantities to compare are the turbulence intensities of the filtered DNS velocities. However, although numerical differentiation has a low-pass filtering effect, the filter operator is not distinctly defined in implicitly-filtered LES [84, 22] and, consequently, neither is the associated filter size.

Figure 3.11(a) shows the root-mean-squared (rms) of the streamwise fluctuating velocity for DNS, LES without SGS model, and LES with DSM. In the absence of model, the LES intensities are over-predicted compared with DNS and under-predicted with DSM. Similar results are obtained for the wall-normal and spanwise velocity fluctuations. The change in magnitude of the LES rms fluctuating velocities can be easily understood through the volume integrated conservation of energy equation over the channel flow domain,

$$\frac{u_\tau^2 QV}{2\delta^2} = \int_{\mathcal{V}} (\nu + \nu_e) \left(\frac{\partial \bar{u}_i}{\partial x_k} \frac{\partial \bar{u}_i}{\partial x_k} + \frac{\partial \bar{u}_i}{\partial x_k} \frac{\partial \bar{u}_k}{\partial x_i} \right) \mathrm{d}V. \tag{3.20}$$

where $V = 2\delta L_1 L_3$. Eq. (3.20) shows that the power input to maintain the mass flow Q must be dissipated by the viscous and SGS terms. For DNS and LES with no SGS model, where $\nu_e = 0$, this is achieved by the velocity gradients, $\partial\bar{u}_i/\partial x_j$. Unlike in DNS, where the fluctuations are resolved and the resulting gradients are physical, in LES with no SGS model, the length scales are limited by the grid size Δ_j, and the gradients $\sim u_i'/\Delta_j$. Thus, the only possible mechanism to maintain consistency with the energy equation (3.20) for increasing Δ_j is by increasing the fluctuating velocities as illustrated in Figure 3.11(a). In the case of LES with an SGS model, the additional dissipation through $\nu_e \neq 0$ provides the a way to achieve balance without the necessity to increase the fluctuating velocities.

Thus, the physical mechanism regulating the magnitude of the fluctuating velocities in implicitly-filtered LES is unrelated to the (undefined) filtering operation, but rather to the necessity of generate dissipative terms of the correct magnitude. Nevertheless, the results above shows that even if implicitly-filtered LES is not rigorously equivalent to the filtered Navier-Stokes equations, it does hold some resemblance in the sense that the values of ν_e providing the correct mean velocity profile are accompanied by lower rms velocities as it would be expected from the filtered DNS velocity field.

In general, one is interested in predicting DNS values, whereas their filtered counterparts are of less practical importance. The metric adopted to measure errors in the turbulence intensities in this section is

$$\mathcal{E}_{f,i} = \left[\frac{\int_{0.2\delta}^{\delta} \left(\langle \bar{u}_i'^2 \rangle - \langle u_i'^2 \rangle \right)^2 \mathrm{d}x_2}{\int_{0.2\delta}^{\delta} \langle u_i'^2 \rangle^2 \mathrm{d}x_2} \right]^{1/2}, \quad i = 1, 2, 3, \tag{3.21}$$

where the comparison is made directly with unfiltered DNS values. For brevity, we will occasionally omit the subscript i when the particular component is not relevant in the discussion. Our goal is to estimate $\mathcal{E}_f$ as a function of Δ. The numerical results are also compared with filtered DNS data (fDNS) using a three-dimensional box-filter with filter size equal to the LES grid resolution in each direction.

3.5.1 Theoretical estimations

In the logarithmic layer of wall-bounded turbulence at high Reynolds numbers, the intensities of the velocity fluctuations are known to follow

$$\frac{\langle u_1'^2\rangle}{u_\tau^2} = B_1 - A_1 \log\left(\frac{x_2}{\delta}\right), \quad \frac{\langle u_2'^2\rangle}{u_\tau^2} = B_2, \quad \frac{\langle u_3'^2\rangle}{u_\tau^2} = B_3 - A_3 \log\left(\frac{x_2}{\delta}\right), \tag{3.22}$$

where the coefficients B_i and A_i are constants considered to be universal for turbulent channel flows. Equations (3.22) can be derived by using the attached-eddy hypothesis [160] or by dimensional analysis on the k^{-1} spectrum of u_1 and u_3 [117], and the blocking effect of the wall for u_2. The hypothesis has been confirmed at high-Reynolds-number flows [89, 49], and it has also been clearly observed in the spanwise velocity fluctuations even for relatively low Reynolds numbers [53, 141, 80, 73]. An important consequence of Eqs. (3.22) is that at a given x_2 in δ units, the magnitude of the velocity fluctuations scaled with u_τ is constant and independent of the Reynolds number.

The LES asymptotic high-Reynolds-numbers limit for the filtered fluctuating velocities $\langle \tilde{u}_i'^2\rangle$ can be written as

$$\frac{\langle \tilde{u}_1'^2\rangle}{u_\tau^2} = \tilde{B}_1 - \tilde{A}_1 f\left(\frac{x_2}{\delta}\right), \quad \frac{\langle \tilde{u}_2'^2\rangle}{u_\tau^2} = \tilde{B}_2, \quad \frac{\langle \tilde{u}_3'^2\rangle}{u_\tau^2} = \tilde{B}_3 - \tilde{A}_3 f\left(\frac{x_2}{\delta}\right), \tag{3.23}$$

where $\tilde{B}_i$ and $\tilde{A}_i$ are constants that depend on Δ_i, and f is an unknown function such that $f(x_2) \to \log(x_2)$ as $\Delta_i \to 0$. The exact dependence of $\tilde{B}_i$ and $\tilde{A}_i$ on Δ_i, and the particular shape of f is expected to vary with the filter. The value of $\langle \tilde{u}_i'^2\rangle$ may be estimated for a symmetric filter with well-defined non-zero second moment in real space by considering the relation [22, 180]

$$\langle \tilde{u}_i'^2\rangle = \langle \widetilde{u_i'^2}\rangle - \Delta_k^2 \left\langle \left(\frac{\partial \tilde{u}_i'}{\partial x_k}\right)^2 \right\rangle + \mathcal{O}(\Delta_i^2 \Delta_i^2). \tag{3.24}$$

If we further assume that $\langle \widetilde{u_i'^2} \rangle \approx \langle u_i'^2 \rangle$,

$$\frac{\langle \tilde{u}_i'^2 \rangle}{u_\tau^2} \approx B_i - A_i \log\left(\frac{x_2}{\delta}\right) - \Delta_k^2 \left\langle \left(\frac{\partial \tilde{u}_i'}{\partial x_k}\right)^2 \right\rangle, \tag{3.25}$$

where $A_2 = 0$. Eq. (3.25) shows that the wall-parallel turbulence intensities of the filtered field do not follow Eq. (3.22), and the major contributor to the departure from the classic logarithmic law is the filter dependent correction term on the right-hand side of (3.25). The error is then given by

$$\mathcal{E}_{f,i} \sim \Delta_k^2 \left\langle \left(\frac{\partial \tilde{u}_i'}{\partial x_k}\right)^2 \right\rangle, \tag{3.26}$$

and the estimation for G in section 3.4.1 yields

$$\mathcal{E}_f^{\mathrm{sh}} \sim \Delta^0, \quad \mathcal{E}_f^{\mathrm{in}} \sim \Delta^{2/3}, \tag{3.27}$$

which predict a rather low convergence rate for the LES turbulence intensities.

A limitation of Eq. (3.27) is that it does not provide a clear insight into the explicit logarithmic dependence of $\langle u_1'^2 \rangle$ and $\langle u_3'^2 \rangle$ with x_2. An alternative procedure to estimate $\mathcal{E}_f$ is to connect Eqs. (3.22) and (3.23) by the spectra of the velocity,

$$\frac{\langle u_i'^2 \rangle}{u_\tau^2} = 2 \int_0^\infty E_i(k_p, x_2) \mathrm{d}k_p, \tag{3.28}$$

where E_i is the two-dimensional spectrum for the i-th velocity component as a function of $k_p^2 = k_1^2 + k_3^2$, where k_1 and k_3 are the streamwise and spanwise wavenumbers, respectively. Similarly,

$$\frac{\langle \tilde{u}_i'^2 \rangle}{u_\tau^2} = 2 \int_0^\infty \tilde{E}_i(k_p, x_2) \mathrm{d}k_p, \tag{3.29}$$

where $\tilde{E}_i(k_p, x_2)$ should be interpreted as the energy spectra of the filtered velocities. We will focus on the streamwise velocity component, but the reasoning below is also applicable to the spanwise component. Moreover, to make the problem tractable, we adopt the model spectrum for E_1 from Figure 3.11(b). The four different piecewise domains of the model

correspond to the large-scale, shear-dominated [117], inertial [67] and viscous regimes [68], respectively. Evaluation of Eq. (3.28) for the streamwise velocity component using the model spectrum results in

$$\frac{\langle u_1'^2 \rangle}{2u_\tau^2} \sim \text{constant} - \log\left(\frac{x_2}{b}\right), \tag{3.30}$$

where the contributions from inertial and viscous regimes were neglected. Hence, the results are consistent with the logarithmic functional dependence of the streamwise turbulence intensity from Eq. (3.22). Under the severe assumptions that the filtering operator resembles a Fourier sharp cut-off, and neglecting filtering in the wall-normal direction,

$$\frac{\langle \tilde{u}_1'^2 \rangle}{u_\tau^2} = 2\int_0^\infty \tilde{E}_1(k_p, x_2)\mathrm{d}k_p, \approx 2\int_0^{\pi/\Delta} E_1(k_p, x_2)\mathrm{d}k_p. \tag{3.31}$$

The difference between $\langle u_1'^2 \rangle - \langle \tilde{u}_1'^2 \rangle$, definitory of the error in Eq. (3.21), is

$$\mathcal{E}_{f,1} \sim \int_0^\infty E_1(k_p, x_2)\mathrm{d}k_p - \int_0^{\pi/\Delta} E_1(k_p, x_2)\mathrm{d}k_p, \tag{3.32}$$

and after integration we obtain

$$\mathcal{E}_{f,1}^{\mathrm{sh}} \sim \log(\Delta/x_2), \quad \mathcal{E}_{f,1}^{\mathrm{in}} \sim \Delta^{2/3}, \tag{3.33}$$

for the shear-dominated and inertial regimes, respectively. When the filter cut-off lies on the k_p^{-1} regime, Eq. (3.33) predicts a $\log(\Delta/x_2)$ correction to the Δ^0-dependence estimated in Eq. (3.27), although both cases imply a slow convergence with Δ. Additionally, for Δ within the shear-dominated region,

$$\langle \tilde{u}_1'^2 \rangle \approx \text{constant} + \mathcal{O}(\log(\Delta)), \tag{3.34}$$

independently of x_2, and the LES turbulence intensities will not reproduce the asymptotic logarithmic profile. For the inertial range, the prediction in Eq. (3.33) coincides with the

one reported in Eq. (3.27). Indeed, integration of the model spectrum yields

$$\langle \bar{u}_1'^2 \rangle \sim \text{constant} - \log(x_2) + \mathcal{O}(\Delta^{2/3}), \tag{3.35}$$

and the LES is expected to capture the classic logarithmic behavior in x_2 with an error of the order of $\Delta^{2/3}$.

3.5.2 Numerical assessment

We aim to quantify the exponents α_f and γ_f for the error in turbulence intensities

$$\mathcal{E}_f \sim \left(\frac{\Delta}{\delta}\right)^{\alpha_f} Re_\tau^{\gamma_f}, \tag{3.36}$$

from LES data and the range of grid resolutions of interest in the present work. The results reported in this section are for LES with DSM. Nevertheless, similar conclusions are drawn for AMD for $x_2 > 0.3\delta$ where the turbulence intensities predicted by AMD and DSM are almost indistinguishable. The results are also compared with filtered DNS data (fDNS), but this is only done qualitatively. For that, we use a three-dimensional box-filter with filter size equal to the LES grid resolution in each direction. The choice of this particular filter shape and filter size definition is arbitrary, and it was argued previously that no specific form can be established *a priori* for implicitly-filtered LES.

Figures 3.12(a)-(c) show the turbulence intensities as a function of the wall-normal distance for DNS and LES at $Re_\tau \approx 2000$ and various grid resolutions. The main observation from Figure 3.12(a) is that the LES turbulence intensities diverge from DNS as the grid is coarsened, and the shape of the $\langle \bar{u}_1'^2 \rangle$ becomes distinctively different from $\langle u_1'^2 \rangle$. Moreover, the effect is more pronounced closer to the wall. Hence, the behavior of the DNS is not captured by LES when $\Delta = \mathcal{O}(\delta)$, consistent with the discussion in section 3.5.1. The error between LES and DNS is quantified in Figure 3.12(d) and compared with the predictions from Eq. (3.27). The results show that $\mathcal{E}_{f,1}$ converges as $\Delta^{0.4}$, whereas $\mathcal{E}_{f,2}$ and $\mathcal{E}_{f,3}$ are well represented by $\Delta^{0.7}$.

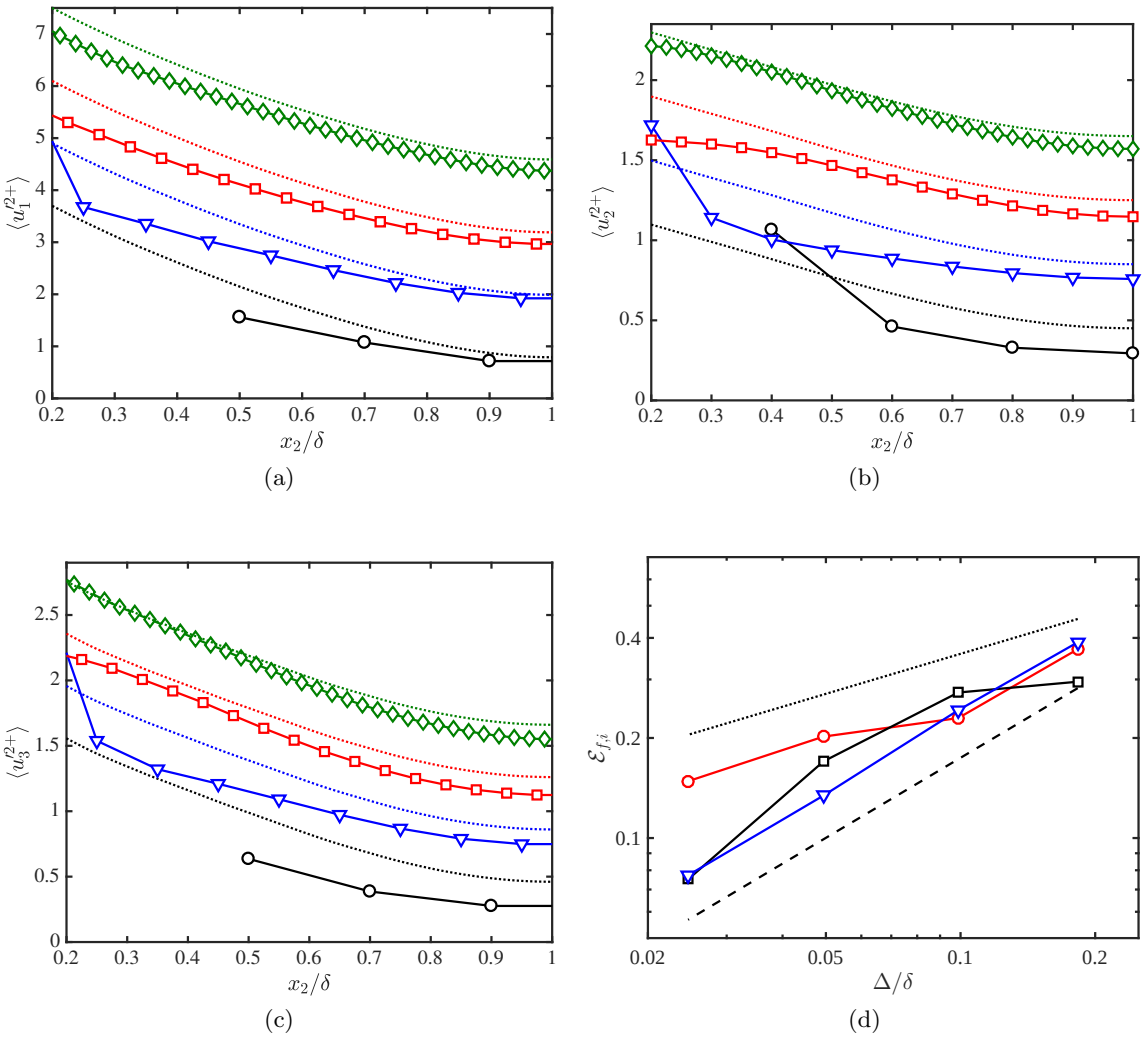

Figure 3.12: (a) Streamwise, (b) wall-normal, and (c) spanwise turbulence intensities of DSM2000-EWS cases as a function of the wall-normal distance for different grid resolutions (or filter sizes) i1 (○), i2 (▽), i3 (□), and i4 (◇) from Table 3.2. The DNS (·····) values are given in the respective colors. For clarity, grid resolutions (filter sizes) i2, i3 and i4 are vertically shifted by 1.2, 2.4 and 3.8 wall units, respectively. The first two points closer to the wall for case DSM2000-EWS-i1 are omitted as they are contaminated by the nonphysical solution close to the wall. (d) Error of the turbulence intensities $\mathcal{E}_{f,i}$ as a function of the characteristic grid resolution for the streamwise (○), wall-normal (▽), and spanwise (□) directions. The dashed and dotted lines are $\mathcal{E}_f \sim \Delta^{0.7}$ and $\mathcal{E}_f \sim \Delta^{0.4}$, respectively.

The effect of the Reynolds number is evaluated in Figure 3.13, which also includes comparisons with fDNS. The grid resolution (or filter size) for the LES and fDNS cases is set to i2 from Table 3.2 ($\Delta = 0.1\delta$), and Re_τ ranges from ≈ 950 to ≈ 4200. The dependence of $\mathcal{E}_{f,i}$ with Re_τ is weak, and the error remains roughly constant for $Re_\tau > 2000$, from where we conclude that $\gamma_f \approx 0$. Therefore, the empirically measured error for the LES turbulence intensities scales as

$$\mathcal{E}_{f,1} \sim \left(\frac{\Delta}{\delta}\right)^{0.4} Re_\tau^0, \quad \mathcal{E}_{f,2}, \mathcal{E}_{f,3} \sim \left(\frac{\Delta}{\delta}\right)^{0.7} Re_\tau^0, \tag{3.37}$$

for $\Delta > 0.025\delta$, and the correct representation of $\langle \bar{u}_i'^2 \rangle$ is more demanding than the mean velocity profile, consistent with the analysis in section 3.5.1.

Figure 3.13(a) also shows that the LES turbulence intensities are well approximated by fDNS, especially for the highest Reynolds numbers and far from the wall. However, the filter operator is not distinctly defined as discussed in the beginning of the section, and the agreement should be interpreted as an indication that the LES turbulence intensities required to predict the correct mean velocity profile for grid size Δ are comparable to the values obtained by filtering the DNS with filter size Δ.

For completeness, we also consider the Reynolds stress tensor interpretation of $\langle u_i u_j \rangle$,

$$R_{ij}^{\mathrm{DNS}} = \langle u_i u_j \rangle - \langle u_i \rangle \langle u_j \rangle, \tag{3.38}$$

where the diagonal components of R_{ij}^{DNS} are the mean squared DNS velocity fluctuations which coincide with the total diagonal Reynolds stress. As argued in Carati et al. [22], assuming $\langle \tilde{\phi} \rangle \approx \langle \phi \rangle$,

$$R_{ij}^{\mathrm{DNS}} = \langle u_i u_j \rangle - \langle u_i \rangle \langle u_j \rangle \approx \langle \widetilde{u_i u_j} \rangle - \langle \tilde{u}_i \rangle \langle \tilde{u}_j \rangle \approx \langle \bar{u}_i \bar{u}_j \rangle + \langle \tau_{ij}^{\mathrm{SGS}} \rangle - \langle \bar{u}_i \rangle \langle \bar{u}_j \rangle = R_{ij}^{\mathrm{LES}}. \tag{3.39}$$

Thus the main difference between considering $\langle u_i' u_j' \rangle$ as a stress rather than a velocity variance lies on the contribution of the SGS tensor, and R_{ij}^{DNS} and R_{ij}^{LES} are directly comparable

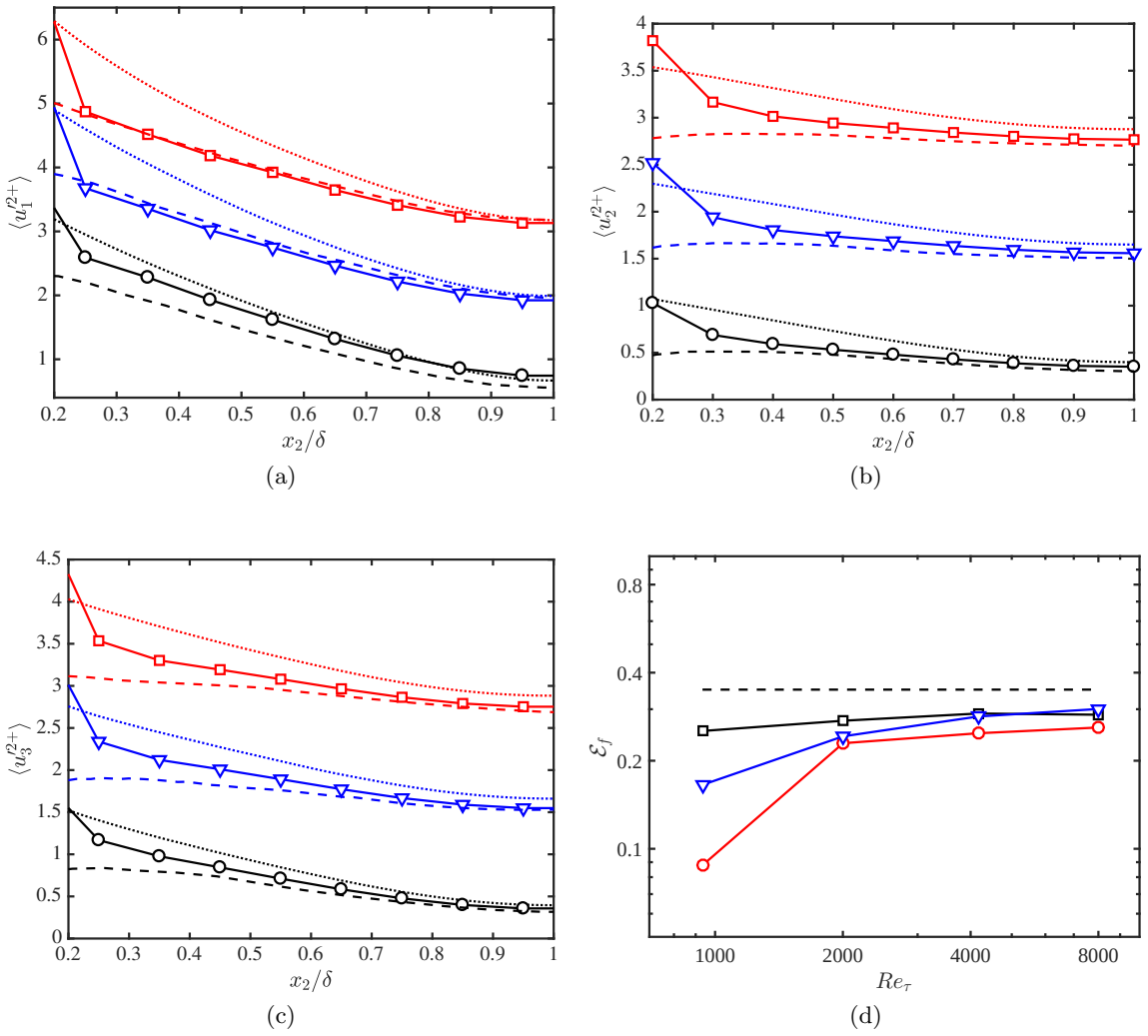

Figure 3.13: (a) Streamwise, (b) wall-normal, (c) and spanwise, turbulence intensities of DSM-EWS cases as a function of the wall-normal distance for $Re_\tau \approx 950$ (○), 2000 (▽), and 4200 (□). The DNS (·····) and box-filtered DNS (- - - -) values are given in the respective colors. For clarity, cases at $Re_\tau \approx 2000$ and $Re_\tau \approx 4200$ are vertically shifted by 1.2 and 2.4 wall units, respectively. (d) Error of the turbulence intensities $\mathcal{E}_{f,i}$ as a function of the Reynolds number for the streamwise (○), wall-normal (□), and spanwise (▽) directions. The reference line is $\mathcal{E}_f = 0.35$ (- - - -).

without prescribing a particular filtering operation. It also shows that the error in the velocity fluctuations can be quantified as the error in the modeled SGS shear stress, i.e., $\tau_{12} - \tau_{12}^{\mathrm{SGS}}$. However, the approach is also accompanied by a limitation for the incompressible Navier-Stokes equations, where the subgrid contribution τ_{ij}^{SGS} is usually modeled as a traceless quantity and in order to allow for straight comparisons, only the deviatoric contributions of R_{ij}^{DNS} and R_{ij}^{LES} must be taken into consideration [175]. An error analogous to Eq. (3.21) can be defined using the traceless counterparts of R_{ij}^{DNS} and R_{ij}^{LES}. The results, omitted for brevity, show that the errors have a weak dependence on the grid resolution and follow $\sim (\Delta/\delta)^{\alpha_f}$ with $\alpha_f < 2/3$.

3.6 Error scaling of the velocity spectra

We consider the two-dimensional kinetic energy spectra for the unfiltered velocity field at a given wall-normal distance x_2, $E_K(k_1, k_3, x_2) = \langle \hat{u}_i \hat{u}_i^* \rangle_t / 2$, where $\hat{(\cdot)}$ is the Fourier transform in the homogeneous directions, $(\cdot)^*$ denotes complex conjugate, and $\langle \cdot \rangle_t$ is average in time. Similarly, the kinetic energy spectra for the filtered velocity is $\tilde{E}_K(k_1, k_3, x_2) = \langle \hat{\tilde{u}}_i \hat{\tilde{u}}_i^* \rangle_t / 2$. The magnitude of E_K is given by

$$\langle u_1'^2 + u_2'^2 + u_3'^2 \rangle = 2 \int_0^\infty \int_0^\infty E_K(k_1, k_3, x_2) \, \mathrm{d}k_1 \mathrm{d}k_3, \tag{3.40}$$

(analogously for $\tilde{E}_K$ and $\bar{E}_K$) and it was investigated in the previous section. We are now concerned with the distribution of energy in the homogeneous scale-space at a given wall-normal distance. Similarly to the turbulence intensities, we compare directly to DNS and thus define the error in the energy spectra as

$$\mathcal{E}_s(x_2) = \left[\frac{\int_0^\infty \int_0^\infty (\bar{E}_K - E_K)^2 \, \mathrm{d}k_1 \mathrm{d}k_3}{\int_0^\infty \int_0^\infty E_K^2 \, \mathrm{d}k_1 \mathrm{d}k_3} \right]^{1/2}. \tag{3.41}$$

3.6.1 Theoretical estimations

The effect of τ_{ij} on the distribution of energy can be analyzed by considering the spectral kinetic energy equation for $\tilde{E}_K$ at a given wall-normal distance,

$$\frac{\partial \tilde{E}_K}{\partial t} = \hat{\mathcal{P}} + \hat{\mathcal{T}} + \hat{\Pi} + \hat{\mathcal{D}} + \hat{\varepsilon} + \hat{\mathcal{D}}_\tau + \hat{\varepsilon}_\tau, \tag{3.42}$$

where the first five terms on the right-hand are the production rate of the turbulent kinetic energy ($\hat{\mathcal{P}}$), turbulent transport ($\hat{\mathcal{T}}$), pressure diffusion ($\hat{\Pi}$), viscous diffusion ($\hat{\mathcal{D}}$), and the molecular dissipation rate ($\hat{\varepsilon}$), respectively. The explicit form of these terms can be found in Mizuno [100]. We will focus on the contributions from τ_{ij},

$$\hat{\varepsilon}_\tau = \mathbb{R}\left[-\mathrm{i}k_1\langle\hat{\tilde{u}}_i^*\hat{\tau}_{i1}\rangle_t - \mathrm{i}k_3\langle\hat{\tilde{u}}_i^*\hat{\tau}_{i3}\rangle_t + \left\langle\frac{\partial\hat{\tilde{u}}_i^*}{\partial x_2}\hat{\tau}_{i2}\right\rangle_t\right], \quad \text{and} \quad \hat{\mathcal{D}}_\tau = \mathbb{R}\left[-\frac{\partial\langle\hat{\tau}_{i2}\hat{\tilde{u}}_i^*\rangle_t}{\partial x_2}\right], \tag{3.43}$$

where $\mathrm{i} = \sqrt{-1}$ and $\mathbb{R}$ denotes the real part. The term $\hat{\varepsilon}_\tau$ is the dissipation rate of the spectral kinetic energy by τ_{ij}, while $\hat{\mathcal{D}}_\tau$ is the wall-normal turbulent transport by τ_{ij}. A detailed equation for the spectral error can be derived from Eq. (3.42) although the result is quite cumbersome. Instead, we will assume, by dimensional arguments, that the functional dependence of $\mathcal{E}_s$ on Δ is proportional to the temporal integration of $(\hat{\varepsilon}_\tau + \hat{\mathcal{D}}_\tau)$,

$$\mathcal{E}_s \sim \int_0^{t_c} (\hat{\varepsilon}_\tau + \hat{\mathcal{D}}_\tau)\mathrm{d}t \sim \Delta^2 G, \tag{3.44}$$

where $t_c \sim G^{-1}$ is a characteristic time, and the estimated error scalings are

$$\mathcal{E}_s^{\mathrm{sh}} \sim \Delta, \quad \mathcal{E}_s^{\mathrm{in}} \sim \Delta^{4/3} \tag{3.45}$$

for grid resolutions comparable to eddies in the shear-dominated or inertial range, respectively.

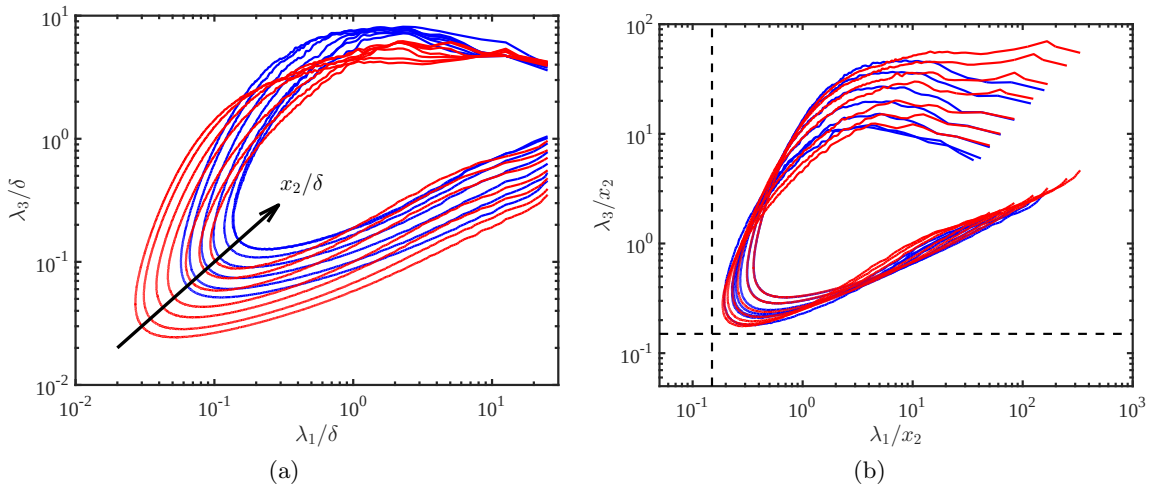

Figure 3.14: Premultiplied two-dimensional kinetic energy spectra for DNS data as a function of the streamwise and spanwise wavelengths normalized by (a) δ, and (b) wall-normal distance. Different contours denote 90% of the turbulent kinetic energy at different heights $x_2/\delta = 0.16, 0.21, 0.30, 0.40, 0.50,$ and 0.60 for $Re_\tau \approx 950$ (——) and $x_2/\delta = 0.08, 0.10, 0.20, 0.30, 0.40,$ and 0.50 for $Re_\tau \approx 2000$ (——).

3.6.2 Energy-resolving grid resolutions estimations

Prior to the numerical assessment of the error scaling, we estimate the required LES grid resolution to resolve 90% of the turbulent kinetic energy at a given wall-normal distance from the two-dimensional spectral energy density $E_K(\lambda_1, \lambda_3, x_2)$ as a function of the streamwise and spanwise wavelengths, namely $\lambda_1 = 2\pi/k_1$ and $\lambda_3 = 2\pi/k_3$, respectively. Simple models describing the 2-D spectral contributions for moderate and high Reynolds numbers have been proposed by Del Álamo et al. [36] and Chandran et al. [24], respectively. However, both works focus on the energy bounds for the large scales, whereas we are interested in the limiting length-scales for the smaller energy-containing eddies, that is, we are seeking for the minimum streamwise and spanwise grid spacing, $\Delta_1^{\min}$ and $\Delta_3^{\min}$ such that $E_K(\lambda_1 > 2\Delta_1^{\min}, \lambda_3 > 2\Delta_3^{\min}, x_2)$ contains 90% of the total turbulent kinetic energy.

Figure 3.14(a) shows contours of 90% energy for E_K at difference wall-normal distances. As expected, the size of the energy-containing eddies shrinks as they get closer to the wall,

and according to the attached eddy hypothesis [160], the only relevant length-scales for the motions spanning along the logarithmic layer is x_2, which allows to write the energy spectra as

$$E_K = E_K(\lambda_1/x_2, \lambda_3/x_2). \tag{3.46}$$

The scaling from Eq. (3.46) has been extensively assessed in the literature [102] and DNS results are plotted in Figure 3.14(b) for various heights and Reynolds numbers. Eq. (3.46) enables the estimation of energy bounds that are approximately valid at all the wall-normal distances within the outer layer. Taking $(\lambda_1)_{\min} = 2\Delta_1^{\min}$ and $(\lambda_3)_{\min} = 2\Delta_3^{\min}$, the *a priori* minimum wall-parallel grid resolutions to resolve 90% of the turbulent kinetic energy at x_2 are

$$\left(\frac{\lambda_1}{x_2}\right)_{\min} = \frac{2\Delta_1}{x_2} \approx 0.15, \quad \left(\frac{\lambda_3}{x_2}\right)_{\min} = \frac{2\Delta_3}{x_2} \approx 0.15. \tag{3.47}$$

For example, to resolve 90% of the turbulent kinetic energy at $x_2 \approx 0.5\delta$, we require $\Delta_1 = \Delta_3 \approx 0.04\delta$. The grid resolution guidelines in Eq. (3.47) imply $\Delta_1 \approx \Delta_3$, in contrast with the common choice of $\Delta_1 > \Delta_3$ among LES practitioners, and usually argued in terms of the elongated streamwise velocity streaks typical of wall-bounded flows. However, it was shown in Figure 3.14(b) that, given its small-scale nature, the 'nose' of the spectra are roughly located at $\lambda_1 \approx \lambda_3$, which justifies the choice of $\Delta_1 \approx \Delta_3$. Nevertheless, it would be reasonable to choose $\Delta_1 > \Delta_3$ for coarser grid resolutions aiming to resolve a lower fraction of the turbulent kinetic energy.

3.6.3 Numerical assessment

Figure 3.15 displays the premultiplied two-dimensional spectra of the streamwise velocity for fDNS and LES (with DSM, AMD, and no explicit SGS model). The filtered spectra was calculated from box-filtered DNS data with a filter size $\Delta_1 \times \Delta_2 \times \Delta_3$. The results show that both DSM and AMD perform similarly, and that the LES spectra is representative of the expected energy distribution for the filtered velocities (Figures 3.15a-c), although the LES prediction tends to be biased towards smaller scales for all grid resolutions.

For cases without explicit SGS model, the spectra is seriously misrepresented for $\Delta >$

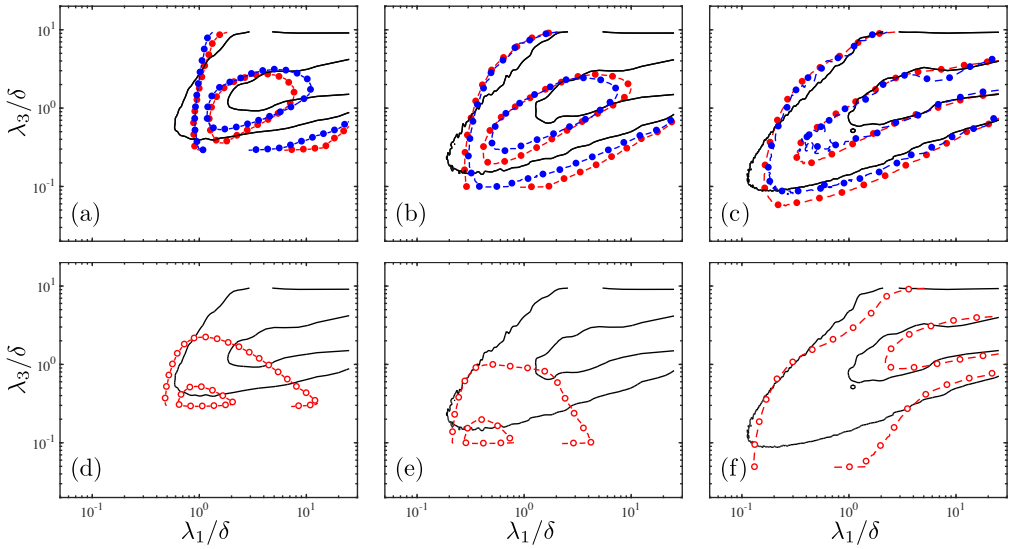

Figure 3.15: Premultiplied two-dimensional streamwise velocity spectra as a function of the streamwise and spanwise wavelengths at $x_2 = 0.75\delta$ for different grid resolutions (left) i1 ($\Delta = 0.2\delta$), (middle) i3 ($\Delta = 0.05\delta$), (right) i4 ($\Delta = 0.025\delta$) from Table 3.2 for the SGS models (top) DSM (●) and AMD model (●) and (bottom) no SGS model (○). The fDNS is given by (——). Contours are 0.1 and 0.6 of the maximum.

0.05δ (Figures 3.15d,e), with most of the energy piled up close to the smallest scales supported by the grid. The physical interpretation of this effect was provided in section 3.5 in terms of the necessary velocity gradients to comply with the conservation of energy. Figures 3.15(d) and (e) are just the spectral depiction of the same effect, i.e., the energy cascades towards the smallest available scales until the resulting gradients can balance the power input driving the flow in the channel. The distribution of energy changes drastically for $\Delta < 0.05\delta$, where large-scale streaks are now a clear constituent feature of the flow (Figure 3.15f). The result is consistent with the visualizations in Figure 3.9(d), which shows a clear streaky pattern in the streamwise velocity for $\Delta = 0.025\delta$, but a notably different non-streaky structure is observed for $\Delta > 0.05\delta$. The existence of this critical grid resolution may be connected to the grid requirements estimated in section 3.6.2, where it was concluded that $\Delta \approx 0.04\delta$ in order to capture at least 90% of the turbulent kinetic energy at $x_2 \approx 0.5\delta$. This seems to be a necessary requirement to support the development of streaks in the absence of SGS model, at least for the particular numerical discretization adopted in this study.

Two mechanisms are potentially responsible for the improvements reported in Figure 3.15 for cases with SGS model with respect to those without: the dissipation of energy piled up at the smallest LES scales by $\hat{\varepsilon}_{\mathrm{SGS}}$, and the redistribution of energy in the wall-normal direction by $\hat{\mathcal{D}}_{\mathrm{SGS}}$. These are the LES counterparts of $\hat{\varepsilon}_\tau$ and $\hat{\mathcal{D}}_\tau$ discussed in section 3.6.1 and their spectra are plotted in Figure 3.16. The computed values reveals that the main contributor is $\hat{\varepsilon}_{\mathrm{SGS}}$ whose magnitude is roughly ten times larger than $\hat{\mathcal{D}}_{\mathrm{SGS}}$, and the improved predictions of the velocity spectra in Figure 3.15(a) and (b) are mostly due to the removal of the excess energy close to the grid cut-off.

Finally, the scaling of $\mathcal{E}_s$ is evaluated in Figure 3.17, which contains the errors for two wall-normal distances $x_2 = 0.2\delta$ and $x_2 = 0.75\delta$. The errors are well scaled by Δ, as argued in 3.6.1 for grid resolutions within the shear-dominated range, and are insensitive to variations in the Reynolds number. In addition, $\mathcal{E}_s$ increases when represented as a function of Δ/δ for different wall-normal heights due to the decrease of the energy-containing eddies relative to δ. Conversely, the errors collapse at different x_2-locations as a function of Δ/L_s,

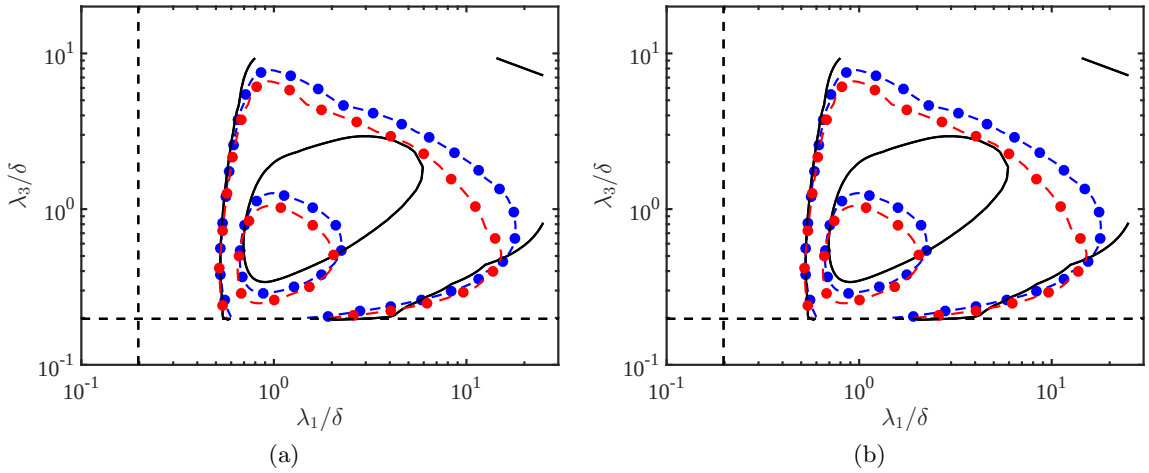

Figure 3.16: Premultiplied two-dimensional spectra of the resolved turbulent kinetic energy $\bar{E}_K$ (——) compared with (a) the SGS dissipation rate of spectral kinetic energy, $\hat{\varepsilon}_{\mathrm{SGS}}$, and (b) the SGS turbulent transport, $\hat{\mathcal{D}}_{\mathrm{SGS}}$, as functions of the streamwise and spanwise wavelengths at $x_2 = 0.75\delta$ for DSM2000-EWS-i2 (●) and AMD2000-EWS-i2 (●). Contours are 0.1 and 0.6 of $\max(\bar{E}_K)$, $\min(\hat{\varepsilon}_{\mathrm{SGS}})$, and $\max(\hat{\mathcal{D}}_{\mathrm{SGS}})$, respectively. Reference lines are $\lambda_1 = \lambda_3 = 0.20\delta$ (- - - ·).

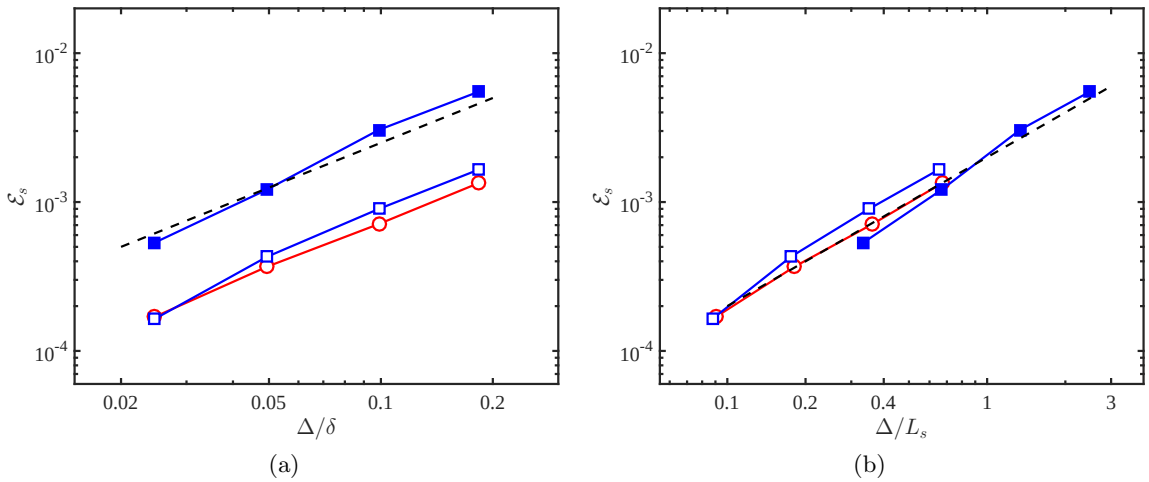

Figure 3.17: Error of the kinetic energy spectra $\mathcal{E}_s$ for DSM-EWS cases as a function of the characteristic grid size Δ scaled by (a) δ and (b) $L_s(x_2)$ for $Re_\tau \approx 950$ (○) and $Re_\tau \approx 2000$ (□) with DSM. Open symbols are for $x_2/\delta = 0.75$ and closed symbols are for $x_2/\delta = 0.2$. Reference lines (- - - ·) are (a) $\mathcal{E}_s \sim \Delta/\delta$ and (b) $\mathcal{E}_s \sim \Delta/L_s$.

reinforcing the shear length scale L_s as the representative physical length-scale to measure the relative magnitude of Δ. In summary, we conclude that the errors in the kinetic energy spectra follow

$$\mathcal{E}_s \sim \left(\frac{\Delta}{L_s}\right) Re_\tau^0. \tag{3.48}$$

3.7 Relevant length-scale for local error quantification

In sections 3.4 and 3.5, we defined the error as an integrated measure across the entire outer layer, and consistently, the grid resolution was non-dimensionalized by the boundary layer thickness δ. However, the length-scale of the energy-containing eddies is a function of the wall-normal distance x_2, and local errors at a given x_2 are expected to vary accordingly. This calls for a new physical length-scale that is relevant for scaling the local SGS model errors. In particular, for the energy spectra, the error was measured locally due its local nature, and the corresponding length-scale was given by the shear length-scale L_s. To investigate the relevant length-scale for the mean velocity profile and turbulence intensities, we define the x_2-dependent error of the mean velocity as

$$\mathcal{E}_{m,l}(x_2) = \left[\frac{\int_{x_2-\Delta_2/2}^{x_2+\Delta_2/2} \left(\langle\bar{u}_1\rangle - \langle u_1\rangle\right)^2 \mathrm{d}x_2}{\int_{0.2\delta}^{\delta}\langle u_1\rangle^2 \mathrm{d}x_2}\right]^{1/2}, \tag{3.49}$$

and the x_2-dependent error of the turbulent kinetic energy $K = (u_1'^2 + u_2'^2 + u_3'^2)/2$ as

$$\mathcal{E}_{K,l}(x_2) = \left[\frac{\int_{x_2+\Delta_2/2}^{x_2+\Delta_2/2} \left(\langle\bar{K}\rangle - \langle K\rangle\right)^2 \mathrm{d}x_2}{\int_{0.2\delta}^{\delta}\langle K\rangle^2 \mathrm{d}x_2}\right]^{1/2}, \tag{3.50}$$

where the integration limits $x_2 \pm \Delta_2/2$ coincide with the LES grid locations of the evaluated quantity. Different candidates for the normalization length, L, are tested, namely, the Kolmogorov scale, the Taylor micro-scale, integral length-scale, and shear length-scale.

The results for $\mathcal{E}_{m,l}$ for AMD4200-EWS-i1,i2,i3,i4 are shown in Figure 3.18, and the best collapse is found for the shear length-scale, L_s. Similar results are obtained for the

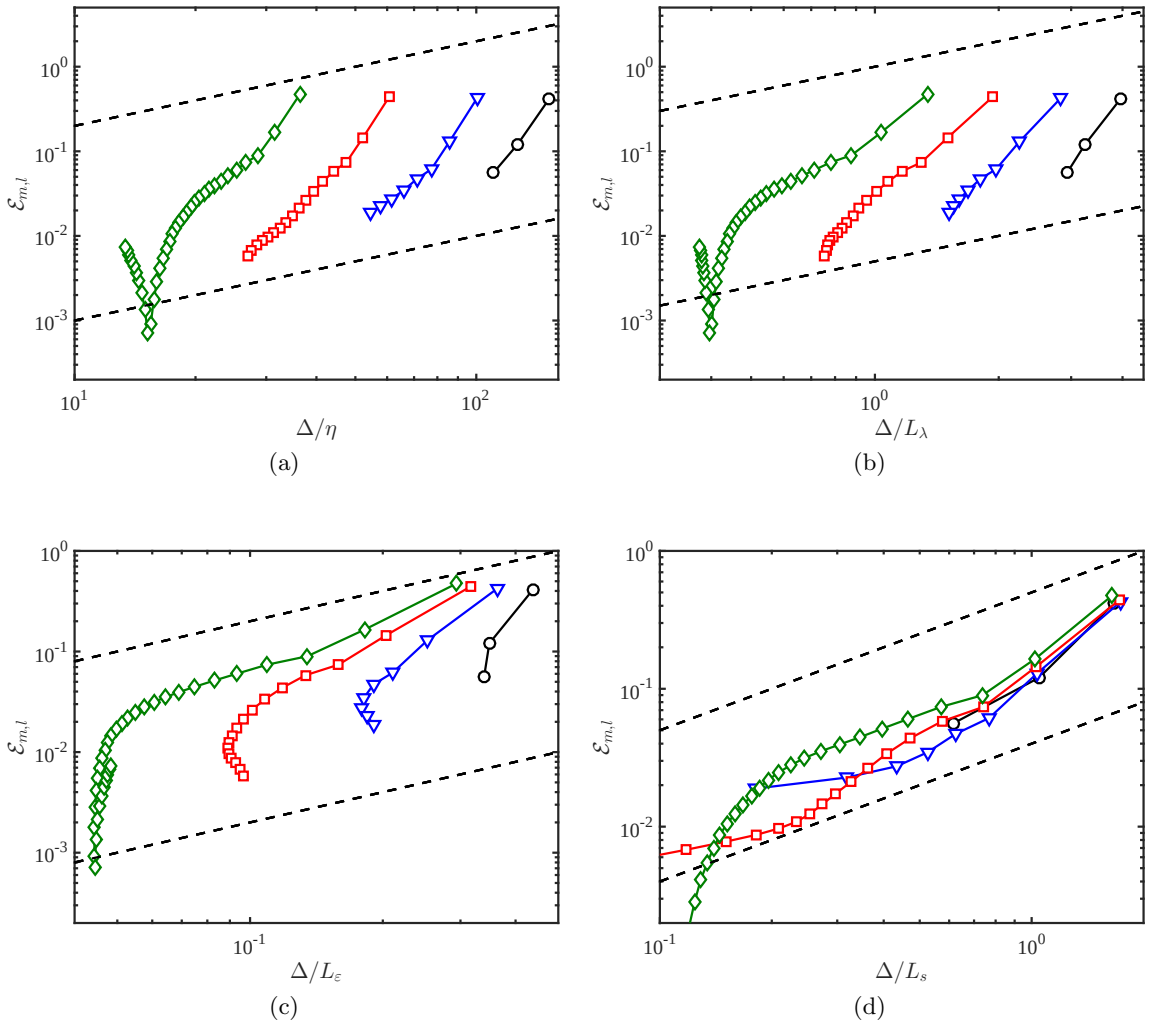

Figure 3.18: Local error in the mean velocity profile as a function of Δ normalized by (a) Kolmogorov scale η, (b) Taylor micro-scale L_λ, (c) integral length-scale L_ε, and (d) shear length-scale L_s for AMD4200-EWS-i1 (○), AMD4200-EWS-i2 (▽), AMD4200-EWS-i3 (□), and AMD4200-EWS-i4 (◇). References lines (- - - ·) are (a) $\mathcal{E}_m \sim \Delta/\eta$, (b) $\mathcal{E}_m \sim \Delta/L_\lambda$, (c) $\mathcal{E}_m \sim \Delta/L_\varepsilon$, and (d) $\mathcal{E}_m \sim \Delta/L_s$.

equivalent DSM cases except for the first off-wall grid point (not shown). It shows that $\mathcal{E}_{m,l} \sim \Delta/L_s$, which are the same scaling as the errors integrated over the entire channel height. The local error lies below 10% when the grid resolution is at least 0.5 times smaller than L_s, and it drastically drops for $\Delta < 0.2L_s$, although these ranges should be understood as tentative estimates. The results are also consistent with the excellent agreement with the scaling of the integrated quantities with δ shown in Figure 3.8 since assuming the universality of mean velocity profile in the outer layer of the boundary layer, the average integrated effect of the shear length-scale is $(L_s)_{\text{avg}} = 1/(0.8\delta)\int_{0.2\delta}^{\delta} L_s(x_2)\mathrm{d}x_2 \sim \delta$. For instance, under the coarse assumption that there is no wake effect and the logarithmic layer is valid until the edge of the boundary layer δ then $(L_s)_{\text{avg}} \approx 0.25\delta$.

The large errors for $\Delta/L_s > 1$ correspond to the first off-wall point. They are the consequence of a very low contribution of τ_{12}^{SGS} at $x_2 = 0$ and, hence, a very large $\langle \partial \bar{u}_1/\partial x_2 \rangle$ in order to achieve the target τ_w. Note that close to the wall $L_s \approx \kappa x_2$, where κ is the von Kármán constant, and given that the third grid point is always at $x_2 = 2\Delta$, then $\Delta/L_s \approx 1/(2\kappa) \approx 1.25$ independently of Δ. Consequently, no improved predictions are expected for the first few off-wall grid point as Δ is refined until the grid resolution reaches the wall-resolved-LES-like regime, as argued by Larsson et al. [71] based on the size of wall-attached eddies across the logarithmic region. However, recent studies show that the first grid point may still be utilized for wall-modeling if a temporal filter is applied [179].

Figure 3.19 shows that the best collapse for $\mathcal{E}_{K,l}$ is also with L_s, which stands again as a sensible measure of the size of the energy-containing eddies that are significant for quantifying LES errors when compared with η, L_λ and L_ε. It shows that $\mathcal{E}_{K,l} \sim (\Delta/L_s)^{2/3}$, consistent with the errors integrated over the entire channel height.

3.8 Summary

Large-eddy simulation has emerged as a fundamental tool for both scientific research and industrial applications. However, the solutions provided by implicitly-filtered LES are grid-dependent, and multiple computations are required in order to faithfully assess the quality of

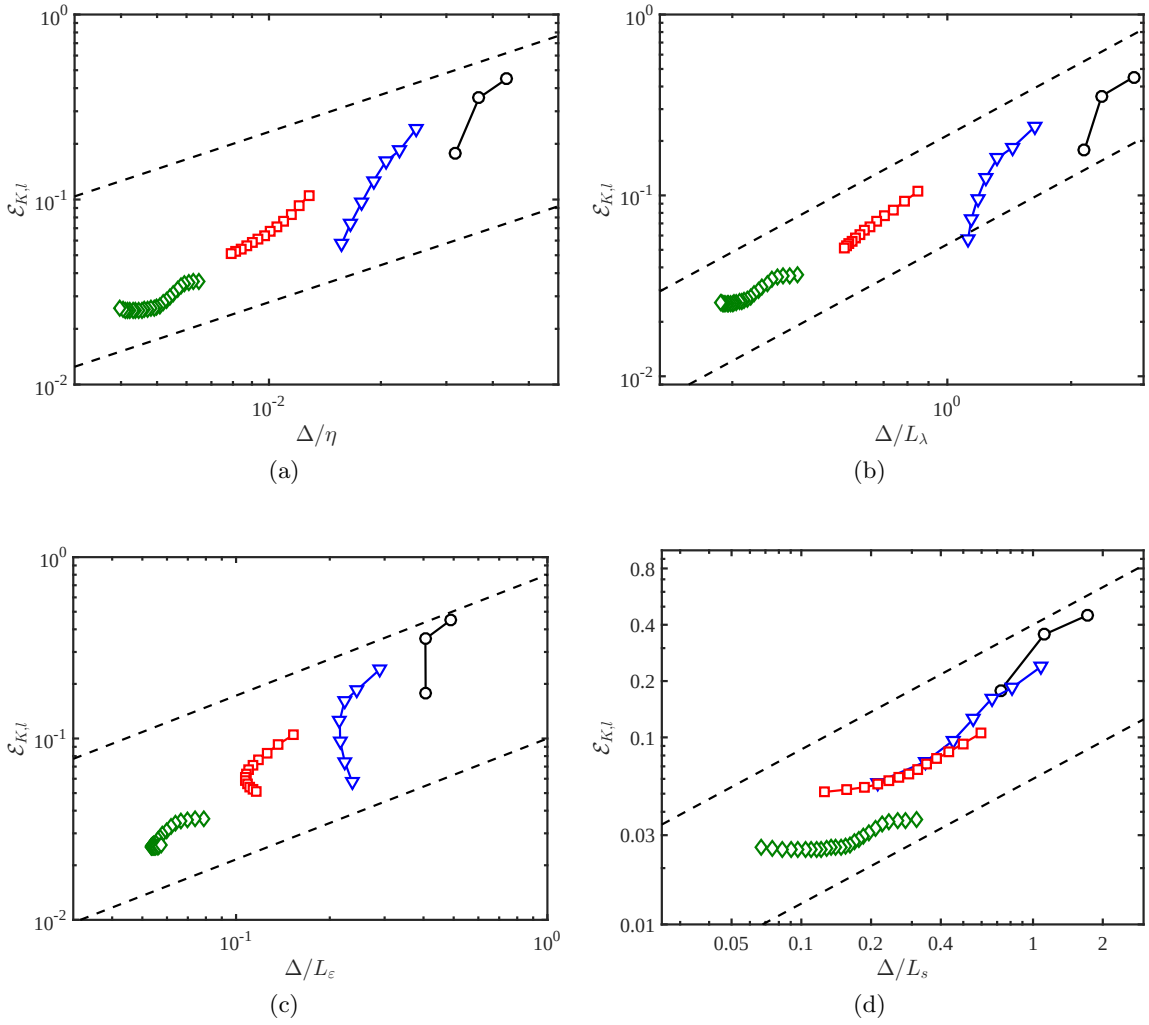

Figure 3.19: Local error in the turbulence kinetic energy as a function of Δ normalized by (a) Kolmogorov scale η, (b) Taylor micro-scale L_λ, (c) integral length-scale L_ε, and (d) shear length-scale L_s for DSM4200-EWS-i1 (○), DSM4200-EWS-i2 (▽), DSM4200-EWS-i3 (□), and DSM4200-EWS-i4 (◇). References lines (- - - ·) are (a) $\mathcal{E}_f \sim (\Delta/\eta)^{2/3}$, (b) $\mathcal{E}_f \sim (\Delta/L_\lambda)^{2/3}$, (c) $\mathcal{E}_f \sim (\Delta/L_\varepsilon)^{2/3}$, and (d) $\mathcal{E}_f \sim (\Delta/L_s)^{2/3}$.

the LES results and obtain meaningful conclusions. This brings the fundamental question of what is the expected LES error scaling as a function of Reynolds number and grid resolution, which has been the aim of this investigation. In particular, we have focused on wall-bounded flows at high Reynolds numbers with grid resolutions comparable to the boundary layer thickness, as expected to be the typical scenario encountered in computational fluid mechanics for external aerodynamics.

LES of wall-bounded turbulence is, nevertheless, challenging since the energy-containing eddies are constrained to reduce their characteristic size in order to accommodate the presence of the wall. Proper wall-resolved LES calculations demand nested grid refinements to capture these eddies, with an associated high computational overhead. To make the problem tractable, previous studies have quantified the SGS errors in wall-resolved LES at relatively low Reynolds numbers and unrealistically fine grids. In those conditions, most of the errors reported are probably dominated by the near-wall region, where SGS models are known to be deficient, while the outer layer resolution is fine enough for the contribution of the SGS models to be negligible. For example, we have shown that for $Re_\tau \approx 1000$ and 20 points per δ, errors smaller than 1% in the mean velocity profile can be obtained by wall-modeled LES without any explicit SGS model. Since wall-modeled LES stands as the most feasible approach compared to wall-resolved LES or DNS and given that in this case, the SGS model is only effective for the outer flow, we have argued that it is necessary to consistently isolate the errors from the bulk flow from those in the near-wall region.

In order to evaluate the performance of SGS models in the outer region independently of the effect of the wall, we have designed a numerical experiment referred to as exact-wall-stress channel flows where the integrated effect of the near-wall region on the outer flow is bypassed by supplying the exact stress at the wall. This numerical experiment retains the same physics as the traditional channel flow far from the wall and hence is a perfect framework to test boundary layer flows. We have considered two SGS models, namely, dynamic Smagorinsky model and minimum dissipation model, that are representative of eddy viscosity models with and without test filtering, respectively.

We have investigated the error scaling of the mean velocity profile, turbulence intensities,

and kinetic energy spectra, with the grid resolution and Reynolds number of the form

$$\mathcal{E}_{(\cdot)} \sim \left(\frac{\Delta}{L}\right)^{\alpha_{(\cdot)}} Re_\tau^{\gamma_{(\cdot)}}, \tag{3.51}$$

for each quantity of interest, where Δ and L are the characteristic grid size and the energy-containing eddies length-scale, respectively. Our results show that Δ/L is an intricate function of the flow state and grid resolutions, but it is well approximated by the L_2-norm of $(\Delta_1, \Delta_2, \Delta_3)$ divided by δ for quantities integrated over the outer layer, and by the shear length-scale, L_s for errors along the wall-normal direction. The observation that $L \approx L_s$ as the relevant physical length-scale to scale LES errors is consistent with L_s as representative of the size of the energy-containing eddies. For large Reynolds number, $Re_\tau > 1000$, the errors are independent of the viscous effects, and $\gamma \approx 0$, as expected for wall-modeled LES. We have derived the theoretical values for $\alpha_{(\cdot)}$ by assuming an hypothetical SGS model that is able to represent the Reynolds stress tensor up to fourth order, and the results have been compared with the empirical values obtained by numerical simulations. To be consistent with the available computational resources, we have only considered cases where the grid resolutions are a fraction of the boundary layer thickness, and the corresponding LES filter cut-off lies either in the shear-dominated regime or in the inertial range, and always far from the viscous Kolmogorov region. Overall, the theoretical predictions match the numerical estimations, and we detail below the results of (3.51) for the different flow statistics investigated.

Errors in the mean velocity profile follow $\mathcal{E}_m \sim \Delta/\delta$, where the constant prefactor is model dependent. Local measurements of the deviation of the LES profiles with respect to DNS have revealed that the errors increase with the proximity of the wall, and the prediction in the first off-wall grid point does not improve with grid refinement until the grid resolutions approach the wall-resolved LES regime.

We have reasoned that the turbulence intensities in implicitly-filtered LES are akin to those from filtered Navier-Stokes, but the former are controlled by the necessity of dissipating the energy input at the rate consistent with the statistically steady state, while the

latter are directly linked to the filtering operation. In terms of convergence, the turbulence intensities are more demanding than the mean velocity profile and their error scales as $\mathcal{E}_f \sim (\Delta/\delta)^{\alpha_f}$ with $\alpha_f \approx 0.4 - 0.7$. Furthermore, in order to correctly capture the classic wall-normal logarithmic dependence of the streamwise and spanwise turbulence intensities, the grid resolution must lie within the inertial range, and we have shown that the turbulence intensities may exhibit a disparate behavior otherwise.

Errors in the relative distribution of the turbulent kinetic energy have been analyzed through the two-dimensional wall-parallel spectra, and they have been shown to follow $\mathcal{E}_s \sim (\Delta/L_s)^{4/3}$. We have pointed out that SGS models affect the distribution of energy via two difference mechanisms, namely, dissipation and space-space transport, but that the former dominates and is ten times larger in magnitude than the latter. The wall-parallel kinetic energy spectra from DNS was also utilized to estimate the LES grid requirements to resolve 90% of the turbulent kinetic energy as a function of x_2, resulting in $\Delta_1 \approx \Delta_3 \approx 0.15x_2$. For example, if we wish to accurately resolved 90% of the turbulent kinetic energy at $x_2 \approx 0.2\delta$, then $\Delta_1 = \Delta_3 \approx 0.03\delta$. If we further assume an isotropic grid, the count results in $\sim$30 points per boundary layer thickness.

Chapter 4

Dynamic slip wall models*

4.1 Motivation

The near-wall resolution requirement to accurately resolve the boundary layer in wall-bounded flows remains a pacing item in large-eddy simulation (LES) for high-Reynolds-number engineering applications. Choi and Moin [26] estimated that the number of grid points necessary for a wall-resolved LES scales as $Re^{13/7}$, where Re is the characteristic Reynolds number of the problem. The computational cost is still excessive for many practical problems, especially for external aerodynamics, despite the favorable comparison to the $Re^{37/14}$ scaling required for direct numerical simulation (DNS), where all the relevant scales of motion are resolved.

By modeling the near-wall flow such that only the large-scale motions in the outer region of the boundary layer are resolved, the grid-point requirements for wall-modeled LES scale at most linearly with increasing Reynolds number. Therefore, wall-modeling stands as the most feasible approach compared to wall-resolved LES or DNS. Several strategies for modeling the near-wall region have been explored in the past, and most of them are effectively applied by replacing the no-slip boundary condition in the wall-parallel directions

*Part of the contents of this chapter have been published in *Physical Review Fluids*, volume 3, 014610 (2018) with coauthors Adrián Lozano-Durán, Sanjeeb T. Bose, and Parviz Moin [6] and submitted to *Journal of Fluid Mechanics* with coauthors Adrián Lozano-Durán, Sanjeeb T. Bose, and Parviz Moin [7].

with a Neumann condition. This approach is motivated by the observation that, with the no-slip condition, most subgrid-scale models do not provide the correct stress at the wall when the near-wall layer is not resolved by the grid [54].

Examples of the most popular and well-known wall models are the traditional wall-stress models (or approximate boundary conditions), and detached eddy simulation (DES) and its variants. Approximate boundary condition models compute the wall stress using either the law of the wall [34, 139, 123, 178] or the Reynolds-averaged Navier-Stokes (RANS) equations [10, 171, 29, 60, 113]. DES [149] combines RANS equations close to the wall and LES in the outer layer, with the interface between RANS and LES domains enforced implicitly through the change in the turbulence model. The reader is referred to Piomelli and Balaras [120], Cabot and Moin [19], Larsson et al. [71], and Bose and Park [14] for a more comprehensive review of wall-stress models and to Spalart [148] for a review of DES.

One of the most important limitations of the models above is that they depend on pre-computed parameters and/or assume explicitly or implicitly a particular law for the mean velocity profile close to the wall. Recently this has been challenged by Bose and Moin [13] with a dynamic slip wall model that is free of any *a priori* specified coefficients. In addition, the no-transpiration condition used in most wall models was replaced by a Robin boundary condition in the wall-normal direction. This chapter is divided in two parts. In the first part, we investigate the use of the slip boundary condition at the wall for the three velocity components in the context of wall-modeled LES. The motivation for the use of this boundary condition is corroborated both theoretically and through detailed *a priori* tests of filtered velocity fields. We then assess whether this condition is physically advantageous compared to other boundary conditions when the LES grid resolution is insufficient to accurately resolve the near-wall region. Additionally, sensitivities of the slip boundary condition with respect to Reynolds number, grid resolution, and SGS models in actual LES are explored. In the second part of the chapter, we discuss the requirements for constructing wall models based on the slip condition and present a dynamic procedure independent of any *a priori* tunable parameters, consistent with the slip boundary condition, and based on the invariance of wall stress under test filtering.

The chapter is organized as follows. In section 4.2, we present and motivate the suitability of the slip boundary condition for LES by considering the behavior of the filtered velocities at the wall. *A priori* testing is performed on filtered DNS data to test the validity of the analysis. In section 4.3, we perform a set of turbulent channel LES with the slip boundary condition and study the effect of the slip parameters, choice of SGS model, grid resolution, and Reynolds number on the one-point statistics such as the mean and root-mean-squared (rms) velocity profiles. A more detailed analysis of the effect of the slip boundary condition on turbulence intensities is given in section 4.4. A dynamic procedure is presented in section 4.5, and its performance is evaluated in section 4.6 for LES of two-dimensional and non-equilibrium three-dimensional transient turbulent channel flows and zero-pressure-gradient flat-plate turbulent boundary layer. Finally, a summary is offered in section 4.7.

4.2 Slip boundary condition with transpiration

We define the slip boundary condition with transpiration as

$$\bar{u}_i|_w = l_i \left.\frac{\partial \bar{u}_i}{\partial n}\right|_w + v_i, \quad i = 1, 2, 3, \tag{4.1}$$

where repeated indices do not imply summation. The indices $i = 1, 2, 3$ denote the streamwise, wall-normal, and spanwise spatial directions represented by x_1, x_2 and x_3, respectively, u_i are the flow velocities, $\bar{(\cdot)}$ is the resolved LES field, n is the wall-normal direction, and $(\cdot)|_w$ indicates quantities evaluated at the wall. The grid or filter size will be denoted as Δ_i for the respective directions. We define l_i to be the slip lengths and v_i the slip velocities. In general, both the slip lengths and velocities are functions of space and time. A sketch of the slip boundary condition for a flat wall is given in Figure 4.1. In this section we provide theoretical motivation for the slip boundary condition in the context of filtered velocity components and inspect the validity of Eq. (4.1) using *a priori* testing of filtered DNS data. The physical implications of the slip lengths are investigated in terms of the mean

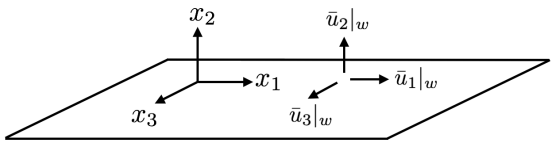

Figure 4.1: Sketch of the slip boundary condition with transpiration ($\bar{u}_2|_w \neq 0$) for a flat wall.

velocity profile and rms velocity fluctuations.

4.2.1 Theoretical motivation

Let us consider a wall-bounded flow. For the Navier-Stokes equations, the velocity at the wall is given by the no-slip boundary condition [152]

$$u_i|_w = 0, \quad i = 1, 2, 3. \tag{4.2}$$

If we interpret LES as the solution of the filtered Navier-Stokes equations [76], the filtering operation in the wall-normal direction will result, in general, in non-zero velocities at the wall. For wall-resolved LES, where the effective filter size near the wall is small, $\bar{u}_i|_w$ can still be approximated by the no-slip boundary condition [45]. However, when the filter size is large or the near-wall resolution is coarse, such as in wall-modeled LES, a modified wall boundary condition different from the usual no-slip is required for the three velocity components. Consider a one-dimensional symmetric filter kernel $\mathcal{G}(\chi)$ with nonzero associated filter size $\tilde{\Delta}$ defined by its second moment

$$\tilde{\Delta}_{\mathcal{G}}^2 = \int_{-\infty}^{\infty} \mathcal{G}(\chi')\chi'^2 \, \mathrm{d}\chi'. \tag{4.3}$$

Then, far from the wall ($x_2 \gg \tilde{\Delta}$), where $x_2 = 0$ is the location of the wall, the filtered velocity field can be computed as

$$\tilde{u}_i(\boldsymbol{x}) = \int_{-\infty}^{\infty}\int_{-\infty}^{\infty}\int_{-\infty}^{\infty} \mathcal{G}(-x_1+\chi_1')\mathcal{G}(-x_2+\chi_2')\mathcal{G}(-x_3+\chi_3')u_i(\boldsymbol{\chi'}) \, \mathrm{d}\boldsymbol{\chi'}, \tag{4.4}$$

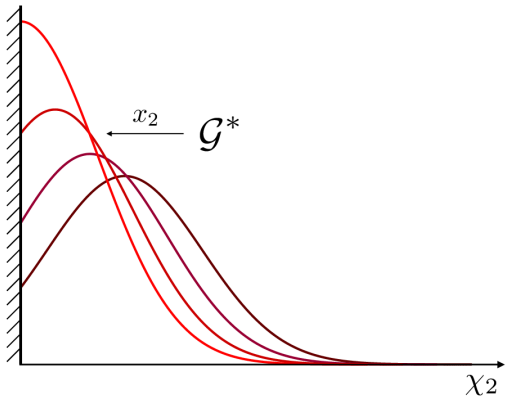

Figure 4.2: Sketch of the change in effective kernel near the wall as it approaches the wall.

where $\boldsymbol{x} = (x_1, x_2, x_3)$ and $\boldsymbol{\chi'} = (\chi_1', \chi_2', \chi_3')$. However, in near-wall region, the filter kernel in the wall-normal direction has a functional dependence on the wall-normal distance, which becomes prevalent as $x_2 \to 0$ for depicted in Figure 4.2. The new filter operator restricted by the wall then becomes

$$\tilde{u}_i(\boldsymbol{x}) = \int_{-\infty}^{\infty}\int_{0}^{\infty}\int_{-\infty}^{\infty} \mathcal{G}(-x_1+\chi_1')\mathcal{G}^*(x_2,-x_2+\chi_2')\mathcal{G}(-x_3+\chi_3')u_i(\boldsymbol{\chi'})\,\mathrm{d}\boldsymbol{\chi'} \tag{4.5}$$

where

$$\mathcal{G}^*(x_2,\chi) = \frac{\mathcal{G}(\chi)}{\int_{-x_2}^{\infty}\mathcal{G}(\varphi)\,\mathrm{d}\varphi} \tag{4.6}$$

is the effective (rescaled) kernel at a wall-normal distance x_2.

Assuming no slip for the unfiltered velocity and approximating the velocity near the wall as a Taylor expansion $u_i(\boldsymbol{x}) = \sum_{m=1}^{p} a_m x_2^m$, the filtered velocity at the wall can be expressed as

$$\tilde{u}_i|_w = \sum_{m=1}^{p} a_m M_{\mathcal{G}_0^*}^{(m)}, \tag{4.7}$$

where $M_{\mathcal{G}_0^*}^{(m)}$ is the m-th moment of $\mathcal{G}^*(0,\chi)$, the effective filter at the wall. From (4.7, it

can be shown that

$$\left.\frac{\partial \tilde{u}_i}{\partial x_2}\right|_w = \sum_{m=1}^{p} -2a_m \mathcal{G}(0) M_{\mathcal{G}_0^*}^{(m)} + m a_m M_{\mathcal{G}_0^*}^{(m-1)}. \tag{4.8}$$

Since $M_{\mathcal{G}_0^*}^{(m)} \sim \tilde{\Delta}_{\mathcal{G}}^{m}$ and $\mathcal{G}(0) \sim \tilde{\Delta}_{\mathcal{G}}^{-1}$, we can use Eqs. (4.7) and (4.8) to obtain an second order approximation of the boundary condition of the form

$$\tilde{u}_i|_w = l \left.\frac{\partial \tilde{u}_i}{\partial x_2}\right|_w, \tag{4.9}$$

where $l = M_{\mathcal{G}_0^*}^{(1)} / \left(1 - 2\mathcal{G}(0) M_{\mathcal{G}_0^*}^{(1)}\right)$.

This boundary condition is exact for a linear velocity profile but is expected to deteriorate as the linear approximation is no longer valid for $x_2 < \tilde{\Delta}$. In this case, the second- and higher-order terms neglected in Eq. (4.9) may result in different slip lengths and extra terms for each velocity component as in Eq. (4.1) in order to achieve an accurate representation of the flow at the wall. The particular expressions for l_i and v_i depend formally on the filter shape, size, and instantaneous configuration of the filtered velocity vector at the wall.

Equation (4.9) motivates the use of the slip boundary condition for wall-modeled LES. Nevertheless, it is important to highlight a few remarks regarding the derivation and the consistency of the slip condition. The first observation is that in the case of explicitly-filtered LES [85, 84, 12] with a well-defined filter operator, the filter size is a given function of the wall-normal distance, and the slip lengths and velocities can be computed explicitly. However, in the present study, we focus on traditional implicitly-filtered LES, where the filter operator is not distinctly defined and, as a consequence, neither is the filter size, which is typically assumed to be proportional to the grid size. This supposed relation between the filter and grid sizes is not always valid [84, 142], and worsens close to the wall. Therefore, in the near-wall region, it is reasonable to assume that the effective filter size is an unknown function of the wall-normal distance, and the slip lengths and velocities must be modeled as they cannot be computed explicitly. As a final remark, note that commutation of the filter and derivative operators is necessary to formally derive the LES equations which, in turn,

entails a constant-in-space filter size or filter operator constructed to be commutative [88]. This condition is not met by Eq. (4.1) but given that the filter size for implicitly-filtered LES is an unknown function of space, we also neglect terms arising from commutation errors.

4.2.2 A priori evaluation

A priori testing of the slip boundary condition is conducted to assess the validity of Eq. (4.1) in filtered DNS data of turbulent channel flow from Del Álamo et al. [36], Hoyas and Jiménez [48], and Lozano-Durán and Jiménez [80] at friction Reynolds numbers of $Re_\tau \approx 950$, 2000 and 4200, respectively.

In the following, u_τ is the friction velocity, ν is the kinematic viscosity, and the channel half-height is denoted by δ. Wall units are defined in terms of ν and u_τ and denoted by the superscript $+$. In each case, the DNS velocity vector is filtered in the three spatial directions with a box-filter with filter size $\tilde{\Delta}_i/\delta$. The resulting filtered data contain $\tilde{u}_i|_w$ and $\partial\tilde{u}_i/\partial x_2|_w$, which can be used to test the accuracy of Eq. (4.1) by computing their joint probability density function (PDF). The PDF for $Re_\tau = 950$ with $\tilde{\Delta}_1 = \tilde{\Delta}_2 = \tilde{\Delta}_3$ are plotted in Figure 4.3(a-c). The results show, on average, a linear correlation between $\tilde{u}_i|_w$ and $\partial\tilde{u}_i/\partial x_2|_w$, which supports the suitability of the slip boundary condition given in Eq. (4.1) with $v_i = 0$. However, the spread of the joint PDFs increases with increasing filter size. A trend similar to that of Figure 4.3(a-c) appears when increasing the Reynolds number for a constant filter size $\tilde{\Delta}_i/\delta$ (not shown), which implies that the second-order approximation deteriorates as the filter size increases in wall units. However, despite this scaling, a linear relationship between $\tilde{u}_i|_w$ and $\partial\tilde{u}_i/\partial n|_w$ is still satisfied on average, and it will be shown in section 4.3 that this is enough to obtain accurate predictions of the mean velocity profile in actual LES.

Finally, Figure 4.3(d) shows the streamwise slip length l_1 as a function of Reynolds number for a constant $\tilde{\Delta}_i/\delta$. The slip length was computed as the average ratio of $\tilde{u}_1|_w$ and $\partial\tilde{u}_1/\partial x_2|_w$. The plot shows that the dependence of the streamwise slip length on Reynolds number is stronger for smaller Re_τ. This behavior can be explained by the relative thickness

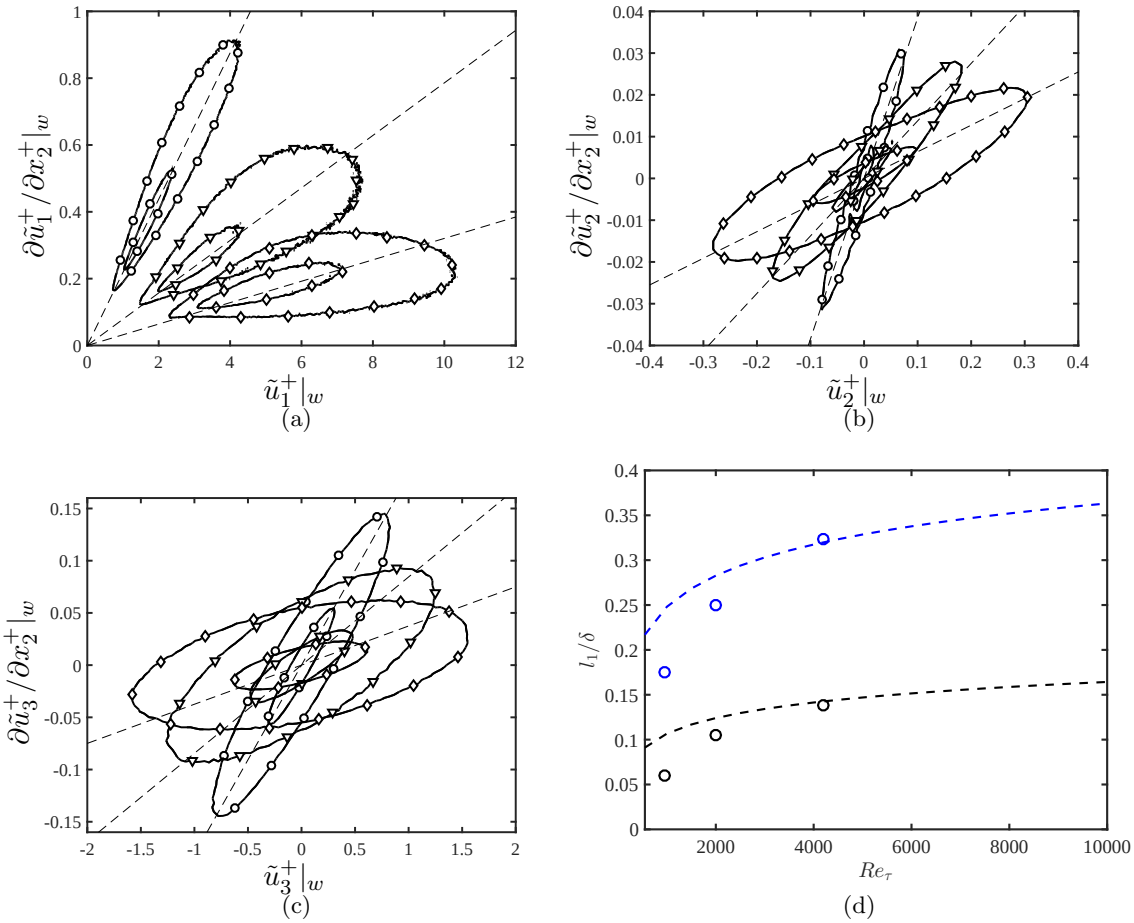

Figure 4.3: Joint probability density function of (a) $\tilde{u}_1|_w$ and $\partial\tilde{u}_1/\partial x_2|_w$, (b) $\tilde{u}_2|_w$ and $\partial\tilde{u}_2/\partial x_2|_w$, and (c) $\tilde{u}_3|_w$ and $\partial\tilde{u}_3/\partial x_2|_w$ for box-filtered DNS and $\tilde{\Delta}_i = 0.01\delta$ ($\circ$), 0.02δ ($\triangledown$), and 0.03δ ($\diamond$) with $Re_\tau = 950$. For each probability distribution the contours are 50% and 95%. (d) l_1 dependence on Re_τ with $\tilde{\Delta}_2 = 0.050\delta$ (black) and 0.100δ (blue) calculated from box-filtered DNS channel flow data ($\circ$), and estimation from box-filtered logarithmic layer approximation $l_1/\delta = \tilde{\Delta}_2/(2\delta)\left[\log(Re_\tau\tilde{\Delta}_2/(2\delta)) - 1\right] + \kappa B\tilde{\Delta}_2/(2\delta)$, $\kappa = 0.41$ and $B = 5.3$, (- - - -).

of the filter size and the buffer layer. When the ratio is of $\mathcal{O}(1)$, the filtered velocity at the wall takes into account contributions from the buffer layer, and l_1 is expected to be sensitive to changes in Reynolds number. However, when the buffer layer is a small fraction of the filter size, most of the contribution to l_1 comes from the logarithmic layer, which has a universal behavior with Re_τ. Neglecting the effect of the buffer layer, the approximate functional dependence of the slip length on Reynolds number can be estimated from the logarithmic velocity profile,

$$\frac{\langle u_1 \rangle}{u_\tau} = \frac{1}{\kappa} \log\left(x_2^+\right) + B, \tag{4.10}$$

where $\langle \cdot \rangle$ denotes average in the homogeneous directions and time, κ is the von Kármán constant, and B is the intercept constant. In the limit of high Reynolds numbers, the box-filtered streamwise velocity and its wall-normal derivative can be estimated by assuming a logarithmic law in the entire near-wall region and integrating Eq. (4.10). This gives an approximation for the average streamwise slip length

$$\frac{l_1}{\delta} \sim \frac{\langle \tilde{u}_1/u_\tau \rangle}{\partial \langle \tilde{u}_1/u_\tau \rangle / \partial (x_2/\delta)} \sim \frac{\tilde{\Delta}_2}{2\delta} \left[\log\left(Re_\tau \frac{\tilde{\Delta}_2}{2\delta} \right) - 1 \right] + \kappa B \frac{\tilde{\Delta}_2}{2\delta} \tag{4.11}$$

(dashed lines in Figure 4.3d), which predicts a weak Re_τ dependence for large Reynolds numbers. It is important to remark that l_1 from the figure is only an estimation from *a priori* testing and the particular values are not expected to work in an actual LES, although we expect the trends to be relevant.

4.2.3 Consistency constraints on the slip parameters

In an actual LES implementation, the choice of l_i and v_i must comply with the symmetries of the flow. Moreover, it is also necessary to satisfy on average the impermeability constraint of the wall to preserve the physics of the flow (more details are offered in section 4.3.6). Therefore, the slip boundary condition for a plane channel flow should fulfill

$$\langle \bar{u}_i |_w \rangle = \left\langle l_i \left. \frac{\partial \bar{u}_i}{\partial n} \right|_w \right\rangle + \langle v_i \rangle = 0, \quad i = 2, 3. \tag{4.12}$$

Equation (4.12) can be further simplified by assuming l_i and v_i to be constant in the homogeneous directions. Since $\langle \bar{u}_i|_w \rangle = 0$ and $\langle \partial \bar{u}_i / \partial x_2|_w \rangle = 0$ for $i = 2, 3$, $\langle v_2 \rangle$ and $\langle v_3 \rangle$ must be set to zero. We can also set $\langle v_1 \rangle = 0$ without loss of generality, since its average effect can be absorbed by moving the frame of reference at constant uniform velocity. Then, the slip boundary condition consistent with the symmetries of the channel is of the form

$$\bar{u}_i|_w = l_i \left. \frac{\partial \bar{u}_i}{\partial n} \right|_w . \tag{4.13}$$

When the flow is no longer homogeneous in x_1, as in a spatially developing flat-plate boundary layer, the above arguments based on the symmetry of the channel do not hold. Then, the slip velocity v_i can be used to impose zero mean mass flow through the walls and ensure that the boundary behaves, on average, as a non-permeable wall. The mass through a flat wall is only affected by v_2, and we can still set v_1 and v_3 to zero for simplicity.

4.3 Effect of the slip boundary condition on one-point statistics

It was argued in section 4.2 that the most general form of the Robin boundary condition, given by Eq. (4.1), should replace the no-slip condition in wall-modeled LES. In this section, we investigate the effects of l_i and v_i on the one-point statistics of LES of plane turbulent channel flow and flat-plate boundary layer. Our conclusions will be numerically corroborated by considering l_i and v_i as free parameters in an LES with slip boundary conditions at the walls. A dynamic procedure to compute these parameters will be given in section 4.5.

4.3.1 Numerical experiments

We perform a set of plane turbulent channel LES with parameters given in Table 4.1. The simulations are computed with a staggered second-order finite difference [110] and a fractional-step method [62] with a third-order Runge-Kutta time-advancing scheme [176].

Case	SGS model	Re_τ	Δ_i^+	Δ_i/δ	l_1/δ	l_2/δ
DSM-2000	DSM	2003	83.3	0.050	0.008	0.008
DSM-2000-s1					0.008	0.004
DSM-2000-s2					0.004	0.008
DSM-2000-s3					0.097	0.045
DSM-2000-c1	DSM	2003	154	0.077	0.008	0.008
DSM-2000-c2			200	0.100		
DSM-950	DSM	934	46	0.050	0.008	0.008
DSM-4200		4179	210			
AMD-2000	AMD	2003	100	0.050	0.008	0.008
SM-2000	SM					
NM-2000	NM					

Table 4.1: Tabulated list of cases. The numerical experiments are labeled following the convention [SGS model]-[Re_τ](-[other cases]). SGS models used are the dynamic Smagorinsky model (DSM), constant coefficient Smagorinsky model (SM), anisotropic minimum-dissipation model (AMD), and no SGS model (NM). Grid resolutions different from the baseline case are noted by c1 and c2. Three additional cases with different slip length than the baseline case are labeled s1, s2, and s3. See text for details.

The size of the channel is $2\pi\delta \times 2\delta \times \pi\delta$ in the streamwise, wall-normal, and spanwise directions, respectively. It has been shown that this domain size is sufficient to accurately predict one-point statistics for Re_τ up to 4200 [80]. Periodic boundary conditions are imposed in the streamwise and spanwise directions. The eddy viscosity ν_e is computed at the cell centers and the values at the wall are obtained by applying the Neumann boundary condition, which is motivated by the fact that for coarse grid resolutions the SGS contribution at the wall must be non-zero. The channel flow is driven by imposing a constant mean pressure gradient, and all simulations were run for at least 100 eddy turnover times (defined as δ/u_τ) after transients.

The slip boundary condition from Eq. (4.13) is used on the top and bottom walls. We have tested the variability of l_i in time by oscillating $l_i(t)$ with different amplitudes and frequencies around a given mean. The frequency of the oscillation considered were 0.5, 1, and 2 times the natural frequency given by the size of the grid and u_τ, and the amplitudes imposed were up to 0.5 times the value of the mean. The different cases resulted in almost

identical one-point statistics as those obtained with a constant l_i of the same mean with the relative difference in the resulting wall stress below 0.5% for all cases. Thus, l_i will be considered constants in both homogeneous directions and time for the remainder of the section.

We take as a baseline case the friction Reynolds number $Re_\tau \approx 2000$ with a uniform grid resolution of $128 \times 40 \times 64$ in the x_1, x_2, and x_3 directions, respectively. The grid size in outer units is 0.050δ in the three directions and follows the recommended grid resolution by Chapman [25] for resolving the large eddies in the outer portion of the boundary-layer. The baseline SGS model used is the dynamic Smagorinsky model (DSM) [42, 77]. The baseline slip lengths are $l_i = 0.008\delta$ for reasons given in section 4.3.2. Three additional cases with different slip lengths are used to study the effect of the slip lengths on one-point statistics.

To study the effects of the slip boundary condition on grid resolution, we define two meshes with $82 \times 26 \times 42$ and $64 \times 20 \times 32$ grid points distributed uniformly in each direction, which correspond to a uniform grid size of 0.077δ and 0.100δ, respectively. The resolutions were chosen such that the first interior point lies in the logarithmic region and is far from the inner-wall peak of the streamwise rms velocity. The intention is to avoid capturing (even partially) the dynamic cycle in the buffer layer, since the wall-normal lengths of the near-wall vortices and streaks scale in viscous units, and that scaling is incompatible with the computational efficiency pursued in wall-modeled LES. The range of grid resolutions is limited due to the fact that the outer layer still needs to be resolved by the LES. However, it will be shown in section 4.3.5 that the selected range of grid resolutions is sufficient to show the sensitivity of the slip lengths on the grid resolution.

To investigate the effect of the Reynolds number we will consider three cases at $Re_\tau \approx$ 950, 2000 and 4200. The sensitivity to the SGS model will be assessed by comparing results from DSM, constant-coefficient Smagorinsky model (SM) [146] without damping function at the wall, the anisotropic minimum-dissipation model (AMD) [135], and cases without an SGS model (NM). Finally, LES results will be compared with DNS data from Del Álamo et al. [36], Hoyas and Jiménez [48], and Lozano-Durán and Jiménez [80].

4.3.2 Control of the wall stress and optimal slip lengths

In an LES of channel flow with the slip boundary condition Eq. (4.13), the wall stress is given by

$$\langle \tau_w \rangle = \nu \left\langle \left. \frac{\partial \bar{u}_1}{\partial x_2} \right|_w \right\rangle - \langle \bar{u}_1 \bar{u}_2|_w \rangle - \left\langle \tau_{12}^{\mathrm{SGS}}\big|_w \right\rangle , \tag{4.14}$$

where τ_w is the stress at the wall, τ_{12}^{SGS} is the tangential SGS stress tensor, and $\langle \bar{u}_1 \bar{u}_2|_w \rangle$ is the result of the non-zero velocity provided by the slip condition. The slip lengths can be explicitly introduced by substituting $\bar{u}_1 \bar{u}_2$ from Eq. (4.13) such that

$$\langle \tau_w \rangle = \nu \left\langle \left. \frac{\partial \bar{u}_1}{\partial x_2} \right|_w \right\rangle - \left\langle \left. l_1 l_2 \frac{\partial \bar{u}_1}{\partial x_2} \frac{\partial \bar{u}_2}{\partial x_2} \right|_w \right\rangle - \left\langle \tau_{12}^{\mathrm{SGS}}\big|_w \right\rangle , \tag{4.15}$$

where τ_{12}^{SGS} also implicitly depend on the slip lengths. Therefore, the wall stress (and hence the mass flow) can be controlled by the proper choice of slip lengths. This is an important property of the slip boundary condition, and it is illustrated in Figure 4.4. For coarse LES with no-slip boundary conditions, the near-wall region cannot be accurately computed due to the inadequacy of the current SGS models and large numerical errors in the near-wall region, even if the resolution is enough to resolve the outer layer eddies. This may result in under- or over-predictions of the wall stress, among other effects, and the mean velocity shift with respect to DNS. Figure 4.4 shows the mean streamwise velocity profile for the cases DSM-2000 and DSM-2000-s[1-3]. The results reveal that increasing l_1 (at constant l_2) moves up the mean velocity profile by 8%, while increasing l_2 (at constant l_1) have the opposite effect and decreases the mean by 15%. Although not shown, it was tested that varying l_3 has a second-order effect on the mean velocity profile when compared to changes of the same order in l_1 and l_2. For instance, the change in mean velocity profile is 1.2% when l_3 is changed from 0.008δ to 0.004δ for case DSM2000. The result is not totally unexpected since $\bar{u}_1$ and $\bar{u}_2$ are active components of the mean streamwise momentum balance in a channel flow (see Eq. 4.15), while $\bar{u}_3$ enters only indirectly. All calculations in this chapter have been performed with l_3 equal to l_2.

The observations in Figure 4.4 may be explained in terms of the mean streamwise

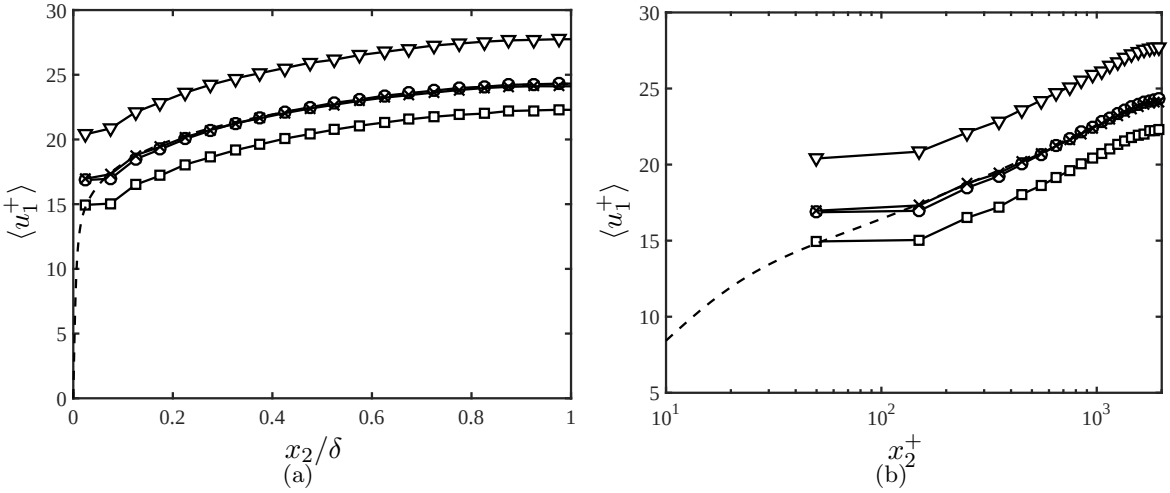

Figure 4.4: Mean streamwise velocity profile as a function of (a) outer units and (b) wall units for DSM-2000, $(l_1, l_2) = (0.008\delta, 0.008\delta)$ ($\circ$), DSM-2000-s1, $(l_1, l_2) = (0.008\delta, 0.004\delta)$ ($\triangledown$), DSM-2000-s2, $(l_1, l_2) = (0.004\delta, 0.008\delta)$ ($\square$), DSM-2000-s3, $(l_1, l_2) = (0.097\delta, 0.045\delta)$ ($\times$), and DNS (- - -)

momentum balance at the wall and non-zero streamwise slip. With respect to the former, increasing l_2 enhances the $\langle \bar{u}_1 \bar{u}_2 \rangle$ contribution at the wall, which is translated into a lower mean velocity profile due to the higher momentum drain at the boundaries. The same argument applies when increasing l_1. However, higher l_1 also implies larger average slip in x_1, which overcomes the previous momentum drain. The resulting net effect of larger l_1 is an increase of the mean mass flow. For the laminar Poiseuille flow with the slip boundary condition, the shift in the mean velocity profile can be computed analytically and can be shown to be proportional to l_1.

The duality between the streamwise and wall-normal slip lengths makes possible to always achieve the correct wall stress by an appropriate selection of (l_1, l_2), which we define as optimal slip lengths. The optimal slip lengths are effectively computed by running an LES with slip boundary condition using Eq. (4.15) with $\tau_w = \tau_w^{\mathrm{DNS}}$ as a constraint, and then averaging in time the values obtained for l_1 and l_2. Note that we have the freedom to impose the ratio l_1/l_2, and the optimal slip lengths are not unique. Two examples are shown in Figure 4.4. Is is also important to remark that the control of the mean velocity

profile is not possible in general without wall-normal transpiration. In particular, if an LES with $l_1/\delta = l_2/\delta = 0$ (no-slip) already over-predicts the mean velocity profile with respect to DNS, the only possible outcome of increasing l_1/δ while maintaining $l_2/\delta = 0$ is a positive shift of the mean velocity profile. Since our experience shows that negative values of l_1 will result in an unstable solution, the conclusion is that the correct mean velocity profile cannot be achieved in theses cases unless $l_2 \neq 0$, making the wall-normal slip length indispensable.

4.3.3 Prediction of the logarithmic layer

A second observation from Figure 4.4 is that the shape of the mean velocity profile remains roughly constant for different slip lengths, and changes in l_1 and l_2 are mainly responsible for a shift along the mean velocity axis. We would like to connect the previous observation with the classic logarithmic profile for the mean streamwise velocity given in Eq. (4.10). Assuming that the filter operation does not alter the logarithmic shape of $\langle \bar{u}_1 \rangle$ for the typical filter sizes (or grid resolutions), Eq. (4.10) should also hold for LES. However, it is not clear whether this would be the case for an actual LES. For example, Millikan's asymptotic matching argument [99] requires a scale separation that tends to infinity as the Reynolds number increases, which is not the case in wall-modeled LES as the length scales are fixed in outer units. Other arguments, such as the Prandtl's mixing length hypothesis [129] would suggest that the correct wall-normal mixing of the flow should be obtained in order to recover the logarithmic profile. Alternatively, from the point of view of Townsend's attached eddy hypothesis [160], the flow from the LES should be populated by a self-similar hierarchy of eddies with sizes proportional to the wall distance and the proper number of eddies per unit area. In all cases, the SGS model plays a non-negligible role in fulfilling these conditions, especially at high Reynolds numbers and coarse grids. As a consequence, not all SGS models are expected to recover the correct shape of the mean velocity profile, and this is further discussed in section 4.3.5.

The prominent role of the SGS model in the correct representation of the logarithmic

layer can be seen from the integrated mean streamwise momentum balance for LES velocities

$$\langle \bar{u}_1^+ \rangle (x_2^+) = \underbrace{\langle \bar{u}_1^+ |_w \rangle}_{\sim B} + \underbrace{x_2^+ \left(1 - \frac{x_2}{2\delta}\right) + \int_0^{x_2^+} \langle \bar{u}_1^+ \bar{u}_2^+ + \tau_{12}^{\mathrm{SGS}+} \rangle dx_2'^+}_{\sim 1/\kappa \log(x_2^+)} . \tag{4.16}$$

By comparing the structure of Eqs. (4.10) and (4.16), it is reasonable to hypothesize that the slip boundary condition mainly influences the intercept B, which is independent of x_2, while the SGS model controls the x_2-dependent slope $1/\kappa$, related to the wall-normal mixing of the flow by the attached eddies. Note that this is not strictly the case, and some coupling is expected between all terms in Eq. (4.16). For example, the value of the integrand at the wall will depend on the slip lengths.

4.3.4 Velocity fluctuations and Reynolds stress contribution

The sensitivity of $\langle u_i'^2 \rangle^{1/2}$ to the choice of slip lengths is examined in Figures 4.5(a). Three cases DSM-2000, DSM-2000-s1, and DSM-2000-s3 are considered, two of them supplying the correct mean velocity profile. The rms velocities are insensitive, especially away from the wall, even when the slip lengths are such that the mean velocity profile does not match that of DNS. The most noticeable difference is observed at the wall, where larger l_1 results in smaller rms values. The consequence is that even if the mean velocity profile matches that of DNS for an optimal (l_1, l_2), some pairs are preferred in order to avoid the near-wall under- and over-shoot in the rms velocity fluctuations. A more comprehensive study of the near-wall turbulence intensities with the slip boundary condition can be found in section 4.4.

Figure 4.5(b) stresses another important property of the slip condition. As was the case for rms velocities, the changes in the mean tangential Reynolds stresses are negligible to varying values of l_1 and l_2, except at the walls. For the case with larger l_1, the wall-stress contribution from the $\langle \bar{u}_1 \bar{u}_2 \rangle$ is roughly 50%, and the remaining stress is then carried by the SGS and viscous terms. This can be considered an advantage compared to the classic no-transpiration condition since the SGS model, usually known to under-predict the wall

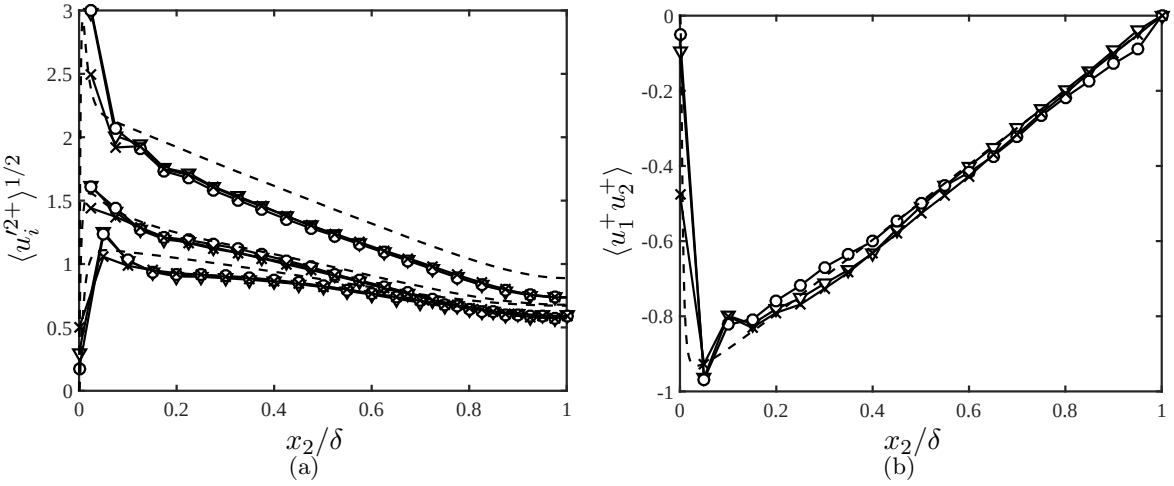

Figure 4.5: (a) Streamwise, spanwise and wall-normal rms velocity fluctuations (from top to bottom), and (b) mean Reynolds stress contribution for DSM-2000, $(l_1, l_2) = (0.008\delta, 0.008\delta)$ ($\circ$), DSM-2000-s1, $(l_1, l_2) = (0.008\delta, 0.004\delta)$ ($\triangledown$), DSM-2000-s3, $(l_1, l_2) = (0.097\delta, 0.045\delta)$ ($\times$), and DNS (- - - ·).

stress [54], is not constrained to account for the resolved non-zero $\bar{u}_i \bar{u}_j$ at the wall.

Finally, the structure of the streamwise velocity at the wall for filtered DNS and wall-modeled LES is shown in Figure 4.6. The filtered DNS data was obtained by box-filtering the streamwise velocity with filter size $\tilde{\Delta}_i = 0.050\delta$, that coincides with the LES grid resolution. Although our analysis is qualitative, the figures show that despite the comparable intensities, the filtered DNS is organized into more elongated streaks. Also note that for a constant l_1, the slip boundary condition forces the velocity and its wall-normal derivative to have the same structure close to the wall, that is inconsistent with box-filtered DNS. This suggests that an accurate representation of the flow structure at the wall is neither expected nor necessary in order to obtain accurate predictions of the low-order flow statistics far from the wall. This is consistent with previous studies indicating that the outer layer dynamics are relatively independent of the near-wall cycle [37, 39, 102, 52, 81, 38].

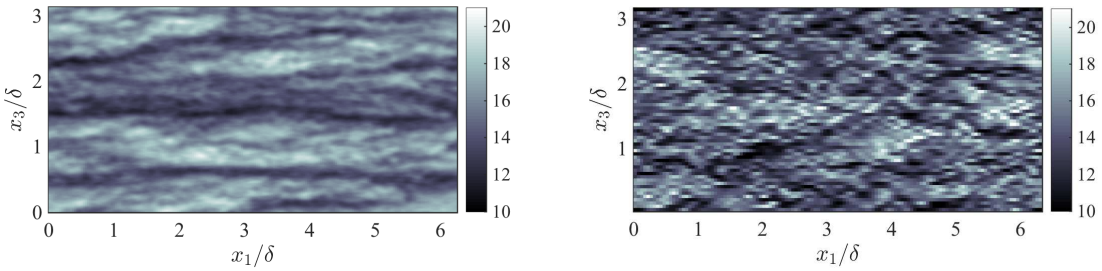

Figure 4.6: Instantaneous snapshot of the streamwise velocity at the wall for (a) box-filtered DNS ($Re_\tau \approx 2000$) with filter size $\tilde{\Delta}_i/\delta = 0.050$ and (b) wall-modeled LES (DSM-2000) with grid resolution $\Delta_i/\delta = 0.050$ of channel flow. Colors indicate velocity in wall units.

4.3.5 Sensitivity to SGS model, Reynolds number, and grid resolution

In this section, we study the effect of the SGS model, Reynolds number, and grid resolution on the mean velocity profile and rms fluctuations for different slip lengths. The discussion is necessary for understanding the most relevant sensitivities of wall models based on the slip boundary condition.

Figure 4.7 shows the sensitivity of the mean velocity to different SGS models for DSM-2000, SM-2000, AMD-2000, and NM-2000. In all of the cases, the slip lengths are fixed and equal to 0.008δ such that the velocity profile at the center of the channel for DSM-2000 matches the DNS data. Note that this particular choice is arbitrary, and that alternative values of slip lengths could be selected to find the best match between SM-2000, AMD-2000, or NM-2000 with DNS. However, the results below are independent of this choice, since the relative shift between cases is barely affected. The results in Figure 4.7 reveal that not only the shape but also the mean mass flow, and thus the optimal slip lengths for each SGS model, are highly dependent on the SGS model for the grid resolutions typical of wall-modeled LES. Regarding the shape of $\langle \bar{u}_1 \rangle$ (Figure 4.7b), for low-dissipation SGS models (e.g. NM), the flow becomes more turbulent, causing the mean velocity profile to flatten due to the enhanced mixing. On the other hand, for highly-dissipative SGS models (e.g. SM), the shape approaches a parabolic profile, that is closer to the laminar solution.

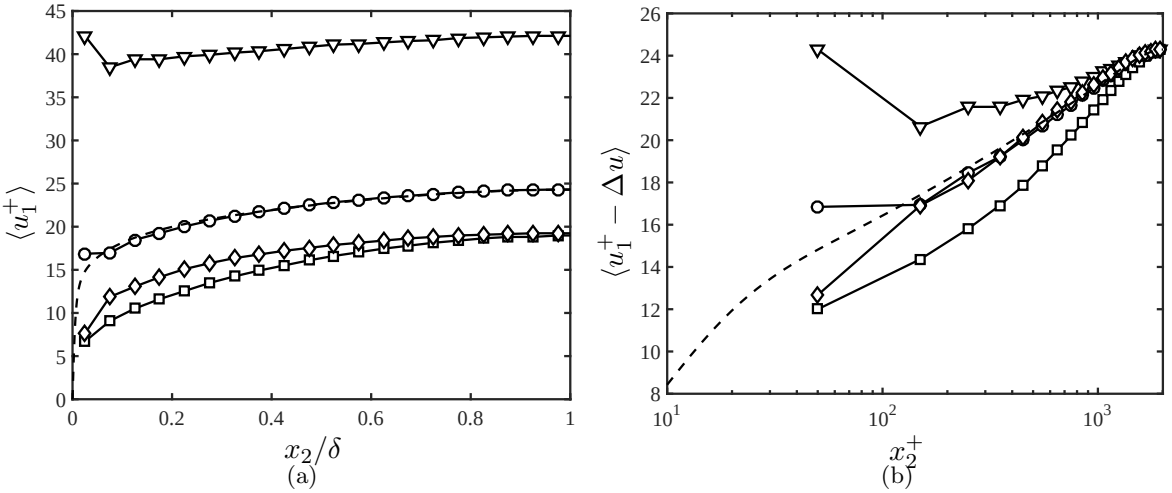

Figure 4.7: (a) Effect of SGS models on the mean velocity profile for $l_i = 0.008\delta$. (b) The mean velocity profiles have been shifted to compare the shapes of the mean velocity profile, where the shift is given by $\Delta u = u_1^+(\delta) - u_1^{+\mathrm{DNS}}(\delta)$. Dynamic Smagorinsky model ($\circ$), constant coefficient Smagorinsky model ($\square$), anisotropic minimum-dissipation model ($\lozenge$), and no model ($\triangledown$) are given for the turbulent channel with $Re_\tau = 2000$. DNS (- - - -).

The effect of each SGS model on the mass flow rate in wall units can be understood by considering the definition of the friction velocity,

$$u_\tau^2 = -\langle \bar{u}_1 \bar{u}_2|_w \rangle + \left\langle \nu \frac{\partial \bar{u}_1}{\partial x_2}\bigg|_w \right\rangle + \left\langle \nu_e \frac{\partial \bar{u}_1}{\partial x_2}\bigg|_w \right\rangle . \tag{4.17}$$

For a channel flow driven by a constant mass flow rate, the last term in Eq. (4.17) is zero for LES without an SGS model, which results in lower u_τ and therefore a positive shift of the mean velocity profile scaled in wall units. For non-zero eddy viscosity, the mean SGS stress at the wall will contribute to increase u_τ, creating a negative shift in the mean velocity profile in wall units. The actual impact of the SGS model on u_τ is more intricate due to the coupling between ν_e and the flow velocities. However, the qualitative behavior of u_τ still holds.

Conversely, the effects on the mass flow can also be explained for a channel flow driven by a constant pressure gradient. In this case, the left-hand side of Eq. (4.17) is fixed. As a consequence, variations in the SGS stress at the wall must be compensated by variations in

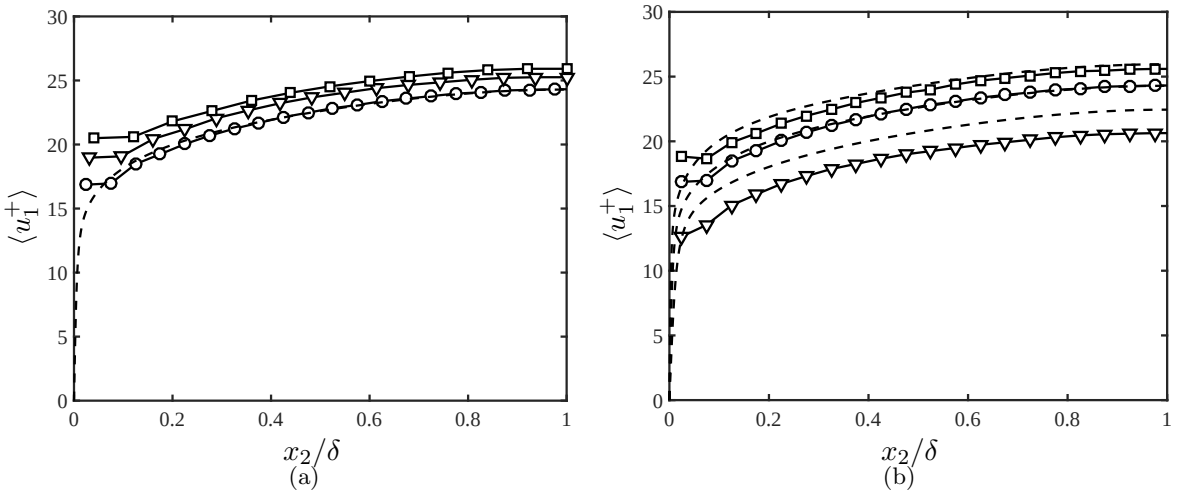

Figure 4.8: Effect of (a) the grid resolution, and (b) Reynolds number on the mean velocity profile for $l_i = 0.008\delta$. (a) $\Delta_i/\delta = 0.050$ (○), 0.063 (▽), and 0.077 (□). (b) $Re_\tau = 950$ (▽), $Re_\tau = 2000$ (○), $Re_\tau = 4200$, (□). DNS (- - - ·).

the Reynolds and viscous stress terms. We have observed that these changes are balanced by the viscous stress, $\nu\, \partial\bar{u}_1/\partial x_2|_w$, rather than by the Reynolds stress term. The variation in the mass flow can then be understood through the slip boundary condition, where larger $\partial\bar{u}_1/\partial x_2|_w$ implies a larger slip at the wall and, hence, higher mass flow.

The grid resolution and Reynolds number sensitivity are studied in Figure 4.8, again maintaining constant slip lengths. Regarding the resolution, coarsening the grid increases the mass flow. This phenomenon is also observed in LES with no-slip boundary condition and, in the present case, is probably related to an inconsistency between the choice of slip lengths and the wall-normal momentum flux provided by the SGS model. Figure 4.8(b) shows a weak dependence of the mean velocity profile on the Reynolds number. The most notable observation is the under-estimation of the mass flow for the lowest Reynolds number, but overall the optimal slip lengths are quite insensitive to Re_τ, consistent with our analysis in section 4.2.2.

4.3.6 The role of slip velocity in imposing zero mean mass flow through the walls

As discussed in section 4.2.3, we require the slip velocities to guarantee no net mass flow through the walls for flows which are inhomogeneous in the wall-parallel direction. The requirement is demonstrated here in an LES of zero-pressure-gradient flat-plate turbulent boundary layer.

The numerical method is similar to that of the channel flow with the exception of the boundary conditions and the Poisson solver, which was modified to take into account the non-periodic boundary conditions in the streamwise direction. The simulation ranges from $Re_\theta \approx 1000$ to 10,000, where Re_θ is the Reynolds number based on the momentum thickness. This range is comparable to the boundary layer simulation by Sillero et al. [141], which will be used for comparisons.

The slip boundary condition from Eq. (4.1) is used in the bottom (x_1-x_3) plane located at $x_2/\delta = 0$. In the top plane, we impose $u_1 = U_\infty$ (free-stream velocity), $u_3 = 0$, and u_2 estimated from the known experimental growth of the displacement thickness for the corresponding range of Reynolds numbers as in Jiménez et al. [56]. This controls the average streamwise pressure gradient, whose nominal value is set to zero. The turbulent inflow is generated by the recycling scheme of Lund et al. [86], in which the velocities from a reference downstream plane, x_{ref}, are used to synthesize the incoming turbulence. The reference plane is located well beyond the end of the inflow region to avoid spurious feedback [109, 143]. In our case, $x_{\text{ref}}/\theta_0 = 890$, where θ_0 is the momentum thickness at the inlet. A convective boundary condition is applied at the outlet with convective velocity U_∞ [114] and small corrections to enforce global mass conservation [143]. The spanwise direction is periodic. The length, height and width of the simulated box are $L_1 = 1060\theta_{\text{avg}}$, $L_2 = 18\theta_{\text{avg}}$ and $L_3 = 35\theta_{\text{avg}}$, where $\theta_{\text{avg}} = 2.12\theta_0$ denotes the momentum thickness averaged along the streamwise coordinate. This domain size is similar to those used in previous studies [138, 56, 141]. The streamwise and spanwise resolutions are $\Delta_1/\delta = 0.05$ ($\Delta_1^+ = 118$) and $\Delta_3/\delta = 0.04$ ($\Delta_3^+ = 84.3$) at $Re_\theta \approx 6500$. The number of wall-normal grid

points per boundary layer thickness is chosen to be ~ 20 at the inlet, which is in line with the channel flow simulations in the previous sections. The grid is slightly stretched in the wall-normal direction with minimum $\Delta_2/\delta = 0.01$ ($\Delta_2^+ = 20.8$). All computations were run with CFL=0.5 and for 50 washouts after transients.

The slip lengths are computed to match the empirical friction coefficient, C_f, from White and Corfield [173]. The connection between the slip parameters and the friction coefficient including the effect of v_2 is

$$\frac{1}{2}U_\infty^2\langle C_f\rangle = \nu\left\langle \frac{\partial\bar{u}_1}{\partial x_2}\bigg|_w\right\rangle - \left\langle l_1 l_2 \frac{\partial\bar{u}_1}{\partial x_2}\frac{\partial\bar{u}_2}{\partial x_2}\bigg|_w\right\rangle + \left\langle v_2\frac{\partial\bar{u}_1}{\partial x_2}\bigg|_w\right\rangle - \left\langle \tau_{12}^{\mathrm{SGS}}\big|_w\right\rangle, \tag{4.18}$$

where the slip lengths are now a function of the streamwise coordinate to take into account the inhomogeneity of the flow in x_1. In order to ensure numerical stability, exponential filtering in time with filter size $0.2\delta/u_\tau$ was applied to the slip lengths in addition to averaging in the homogeneous direction. Equation (4.18) is key to guarantee the correct wall stress, but we have the freedom to impose two more conditions to fully determine l_1, l_2 and l_3, which for simplicity, we set $l_1 = l_2 = l_3 = l$. The value of v_2 is computed at each time step to ensure zero mean mass flow through the wall such that

$$v_2(t+\Delta_t) = -\langle u_2(x_1, 0, x_3, t)\rangle_w, \tag{4.19}$$

where Δ_t is the time step and $\langle\cdot\rangle_w$ denotes averaging over the entire wall. Equations (4.18) and (4.19) were used to compute the slip parameters. The mean v_2 obtained was of the order of $10^{-3}U_\infty$. The slip velocities v_1 and v_3 in Eq. (4.1) are set to zero.

Figure 4.9(a) shows the resulting mean slip lengths computed to produce the target C_f, and that was successfully achieved as shown in Figure 4.9(b). It is important to stress again that one of the main differences of the boundary layer case with respect to the channel flow is the necessity of a nonzero v_2 term from Eq. (4.1) in order to guarantee that the wall behaves as a no-transpiration boundary on average. We have implemented a global condition (constant-in-space v_2, Eq. 4.19) that does not prevent instantaneous local mass

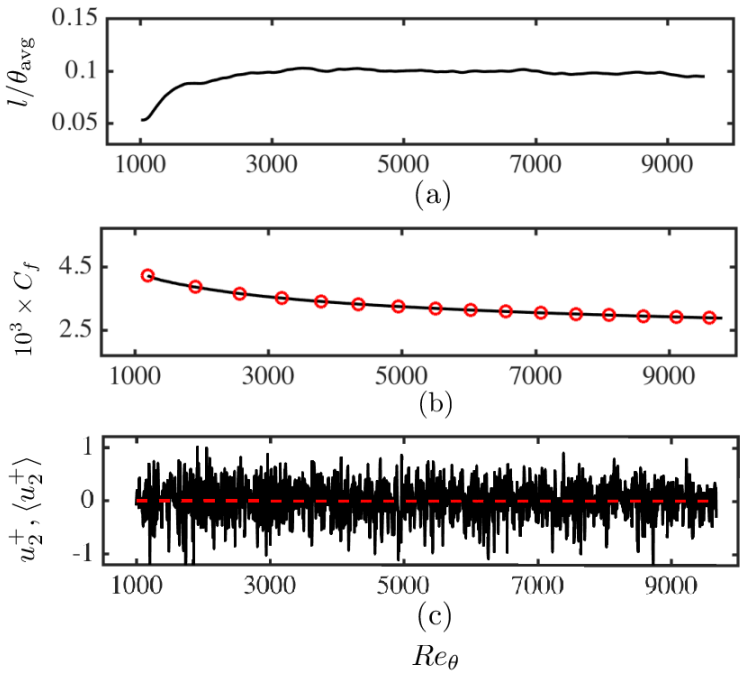

Figure 4.9: (a) Mean slip length l (——) normalized by θ_{avg}, the average momentum thickness, (b) the friction coefficient from the wall-modeled LES (——) and the empirical friction coefficient from White and Corfield [173] (○), and (c) the instantaneous (——) and time-averaged (- - -) wall-normal velocities at the wall as a function of Re_θ.

flow at a particular streamwise location as seen in Figure 4.9(c). However, the mean mass flow remains locally close to zero for all streamwise locations.

The mean streamwise velocity and the three rms velocity fluctuations at $Re_\theta \approx 6500$ ($Re_\tau \approx 1989.5$) are shown in Figure 4.10 and compared with Sillero et al. [141]. As expected, the mean DNS and LES velocities match in the wake region, as the correct C_f in the LES is imposed. The shape of the profile is also well predicted. The rms velocities are reasonably well reproduced at this Reynolds number, with no over-prediction of the streamwise rms velocity and under-prediction of the other two components close to the wall, consistent with the analysis in section 4.3.4. Overall, these results along with those from LES of channel flow in the previous sections show that the slip boundary condition successfully reproduces the one-point statistics of the flow as long as the slip lengths accurately reflect the correct mean wall stress.

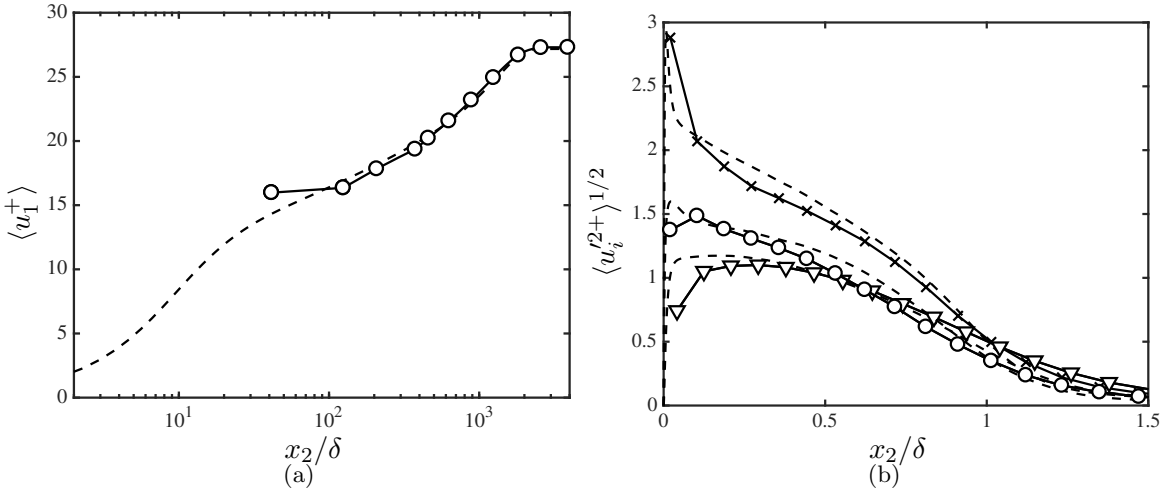

Figure 4.10: (a) Mean streamwise velocity profile (——) and (b) rms streamwise (×), spanwise (○), and wall-normal (▽) fluctuation profiles at $Re_\theta \approx 6500$. Symbols are LES. DNS from Sillero et al. [141] (- - - ·).

Two more cases (not shown) were run to test the effect of the slip boundary condition on the net mass flow through the wall. In the first case, a slip boundary condition was imposed such that the net mass flow through the wall is positive (incoming flow through the wall) such that $\langle \bar{u}_2|_w \rangle_w \approx 0.01 U_\infty$. In this case, the boundary layer thickness grew five times faster than the reference DNS. On the contrary, when the simulation was run with net negative mass flow through the walls ($\langle \bar{u}_2|_w \rangle_w \approx -0.01 U_\infty$), the flow remained laminar. The results are consistent with observations in previous studies on blowing and suction of boundary layers [144, 4, 31, 181] and highlight the relevance of imposing a correct zero net mass flow through the walls in order to faithfully predict the boundary layer growth.

4.4 Effect of the slip boundary condition on predictions of turbulence intensities

4.4.1 Numerical experiments

We perform a set of plane turbulent channel LES. The details of the numerical methods are the same as in the previous section. The DSM is used as the SGS model [42, 77]. The grid

Case	Re_τ	Δ_1^+	Δ_3^+	$\min(\Delta_2^+)$	$\max(\Delta_2^+)$	$\frac{\max\langle\bar{u}_1'^2\rangle^{1/2}}{\max\langle u_{1\mathrm{DNS}}'^2\rangle^{1/2}}$
NS-550-s	546	107.4	53.6	1.41	98.6	1.75
NS-550-s-f	546	53.6	26.8	0.64	49.7	1.24
NS-2000-s-f	2003	196.7	98.3	2.35	182.1	1.90
NS-550-u						1.07
NE-550-u	546	107.4	53.6	34.2	34.2	1.15
SL-550-u						1.00

Table 4.2: Tabulated list of cases. The case name is given in the first column, where the first two upper-case letters indicate the boundary condition used: no-slip (NS), Neumann (NE), and slip (SL). The middle number is Re_τ for $Re_\tau \approx 550$, 2000. The lower-case letter is used to denote the stretching of the grid: stretched (s) and uniform (u). Case with a finer grid resolution is denoted with f. The relative intensity of the peaks for $\langle u_1'^2\rangle^{1/2}$ for LES with respect to DNS is given in the sixth column. The symbols for each case are used in the subsequent plots.

resolutions for this set of cases are chosen to be comparable to those found in the literature [96].

At the wall, three different boundary conditions are applied: the no-slip boundary condition, the Neumann boundary condition without transpiration, and the slip boundary condition with transpiration with the optimal slip lengths. The Neumann boundary condition without transpiration is defined as

$$\frac{\partial \bar{u}_1}{\partial n} = \frac{\tau_w^{\mathrm{DNS}}}{\langle \nu + \nu_e \rangle_w}, \quad \bar{u}_2 = 0, \quad \frac{\partial \bar{u}_3}{\partial n} = 0, \tag{4.20}$$

where τ_w^{DNS} is mean wall stress corresponding to the DNS case. We have adopted the simplification of imposing the correct mean wall stress, which has been shown by Lee et al. [72] to be sufficient for prediction of low-order turbulence statistics in channel flow for the Neumann boundary condition. The channel was driven by imposing a constant mean pressure gradient, and all cases were run for at least $100\delta/u_\tau$ after transients, where u_τ is the friction velocity.

The details of the simulations are given in Table 4.2. The table is divided in two blocks. The first group is used to assess whether the problem under investigation scales in

inner or outer units. The second group serves to evaluate the effect of different boundary conditions. The results are compared with DNS data at the corresponding Reynolds number from Del Álamo et al. [36] and Hoyas and Jiménez [48].

4.4.2 Scaling of the problem

An example of the under- and over-estimation of the turbulence intensities is shown in Figures 4.11(a) and (b). The relative intensity of the peaks for $\langle \bar{u}_1'^{2+} \rangle^{1/2}$ with respect to DNS is given in the last column of Table 4.2.

The first question is to assess whether the grid requirements to address this problem scales in outer or inner units for no-slip LES. As demonstrated in Figure 4.11(a), the resolution used in case NS-550-s ($Re_\tau \approx 550$) results in large peaks for the streamwise rms velocity fluctuations, whereas doubling the number of grid points in each direction improves the prediction noticeably (Figure 4.11c). The result worsens again by increasing the Reynolds number from $Re_\tau \approx 550$ to 2000 while maintaining the finer grid resolution (Figure 4.11d). This suggests that, for the no-slip boundary condition, the problem is independent of the outer-layer eddies, and the required near-wall grid to avoid under/over-predictions scales in wall units.

4.4.3 Effect of the streak breakup

The cause of the problem is analyzed in Figures 4.12 and 4.13, which show instantaneous snapshots and the auto-correlations of $\langle \bar{u}_1'^{2+} \rangle^{1/2}$ at $x_2^+ \approx 15$ for a selection of the cases from Table 4.2. The results reveal that when the peaks are not well-predicted, as in Figures 4.12(a) and 4.13(a), the associated flow is dominated by streamwise streaks several times longer than those of DNS. This is consistent with observations in Baggett [8], Rasam et al. [130], Weatheritt et al. [172]. On the other hand, the lengths of the streaks developed in the flow when increasing the resolution (Figure 4.13b) or introducing the slip boundary condition (Figures 4.12b and 4.13c) are comparable to those from DNS. Although not shown, the Neumann boundary condition (NE-550-u) yields similar results to those observed for

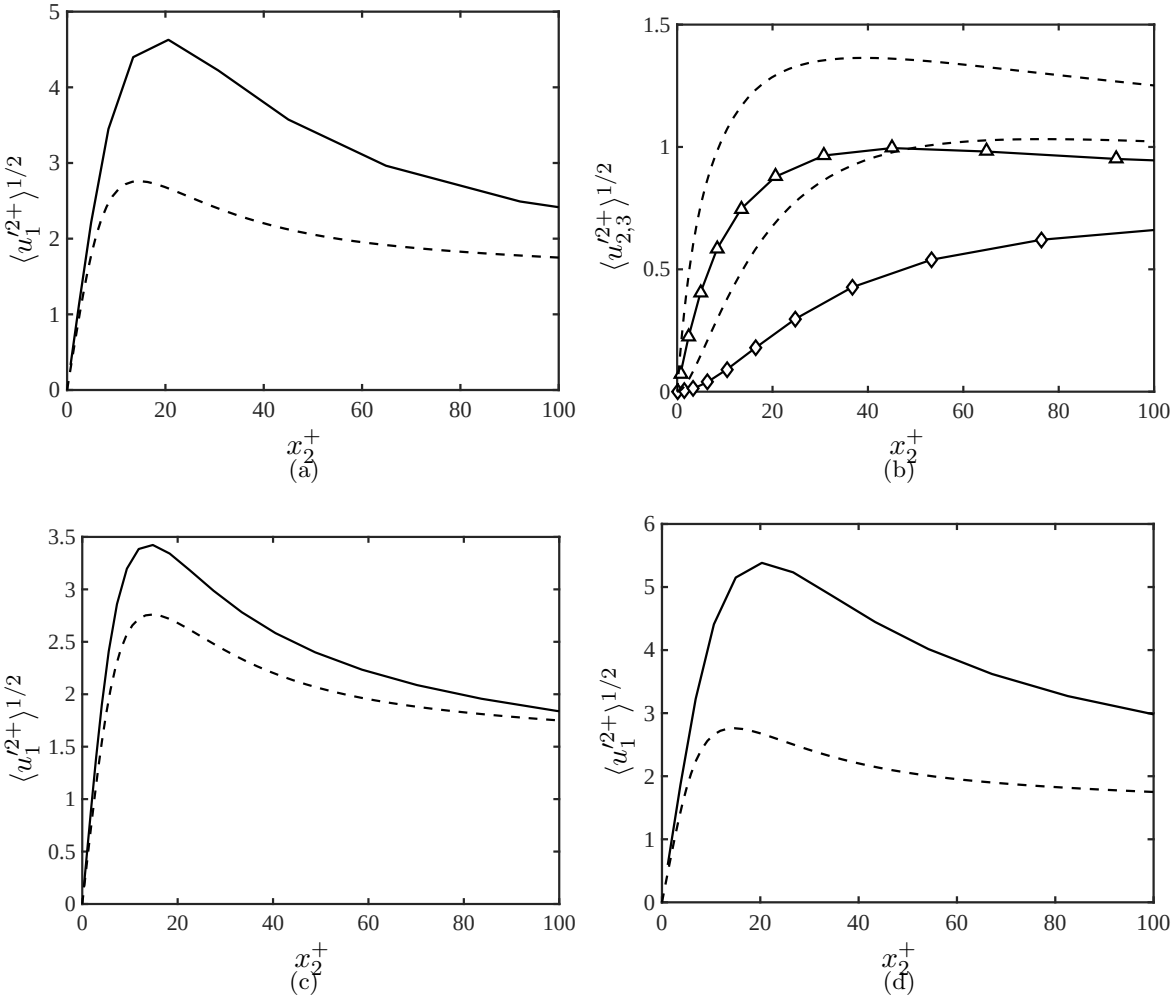

Figure 4.11: The rms velocity fluctuations (——) for NS-550-s in the (a) streamwise, (b) spanwise (△) and wall-normal (◊) directions. Streamwise rms velocity fluctuations for (c) NS-550-s-f and (d) NS-2000-s-f. DNS data at the corresponding Reynolds number (- - - -).

the slip case. Note that the improvement achieved with the Neumann or slip boundary condition does not increase the computational cost of the simulation since grid refinement was not required, in contrast to the improvements attained using the no-slip boundary condition in Figure 4.11(c).

The interpretation from the previous results is that, in the case of the no-slip boundary condition, the near-wall dynamics are altered in such a way that the streaks are unable to follow their natural cycle of meandering and breakup [169, 55], which manifests itself in the flow by a strong $\langle \bar{u}_1'^{2+} \rangle$ and reduced $\langle \bar{u}_2'^{2+} \rangle$ and $\langle \bar{u}_3'^{2+} \rangle$. Other investigations on drag reduction have reported a similar behavior in the turbulence intensities by controlling the near-wall streaks [170] or by adding a stochastic forcing term to break up the large-scale structures [90, 124].

The previous interpretation is further supported by the improved intensities (Figure 4.14) and shorter streamwise streaks (Figure 4.13d) in case NS-550-u, where the first interior grid point is such that the streaks below $x_2^+ \approx 15$ are bypassed while maintaining the no-slip boundary condition. A more systematic analysis of the effect of the first grid point is shown in Figure 4.15(a), where the grid is stretched in order to modify Δ_2 at the wall. For coarse resolutions with $\Delta_2^+ > 15$, the over-prediction of $\langle \bar{u}_1'^{2+} \rangle$ is mitigated for all boundary conditions. By stretching the grid such that Δ_2 is finer at the wall, only the slip boundary condition provides good predictions of the streamwise turbulence intensities regardless of the grid resolution, whereas the results from the no-slip and Neumann boundary conditions degrade for $\Delta_2^+ < 15$. As an example, the streamwise rms velocities for the most stretched grid are shown in Figure 4.15(b). Note that despite the good prediction of the no-slip case for resolutions with $\Delta_2^+ > 15$, this is not a practical solution as the no-slip condition cannot be used in context of wall-modeled LES. Another important remark is that in most wall-modeled LES, the Neumann boundary condition has been used on canonical flows such as channel or boundary layer flows, where the near-wall grid resolution is usually chosen to satisfy $\Delta_2^+ > 15$. Our analysis is relevant for those flow configurations where the local Reynolds number is not known a priori and, hence, the first grid point may lie in the region $\Delta_2^+ < 15$.

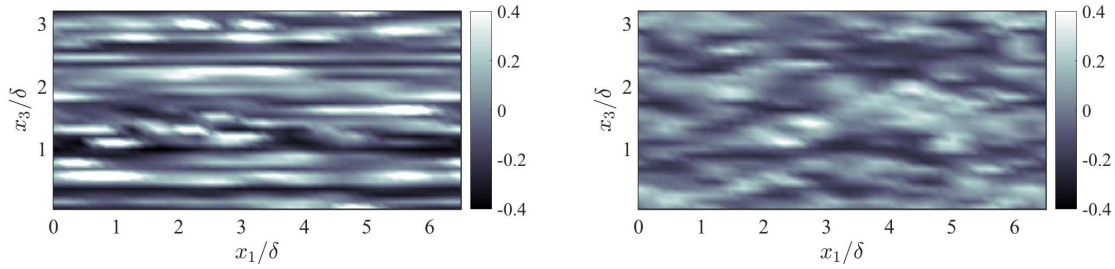

(a) (b)

Figure 4.12: Instantaneous snapshots of the streamwise velocity component at $x_2^+ \approx 15$ for (a) NS-550-s and (b) SL-550-u.

Finally, the results in Figure 4.15(a) highlight the fact that providing the perfect wall model (correct mean wall stress) is not enough for good prediction of the turbulence intensities at all resolutions, and the intensities also depend on the form of the boundary condition.

According to the previous results, both Neumann and slip boundary conditions improve the prediction of the turbulence intensities by avoiding the formation of long streaks; however, the mechanisms involved are different for each case. To analyze in more detail these mechanisms, the production ($\mathcal{P}$), pressure strain (Π), and turbulent transport ($\mathcal{T}$) components of the streamwise turbulence intensity budget are plotted in Figures 4.16(a-c). The choice of these quantities is motivated by the fact that the energy source for $\langle u_1'^{2+} \rangle$ is given by the production term, while the transfer of energy to the $\langle u_2'^{2+} \rangle$ and $\langle u_3'^{2+} \rangle$ components is provided through the streamwise pressure strain correlation [125]. The turbulent transport term is also included since it is used to explain the improvements with the Neumann boundary condition at coarse near-wall grid resolutions.

In all cases, the magnitude of the pressure strain is under-estimated, and moderate improvements appear by refining the grid or using either the Neumann or slip boundary

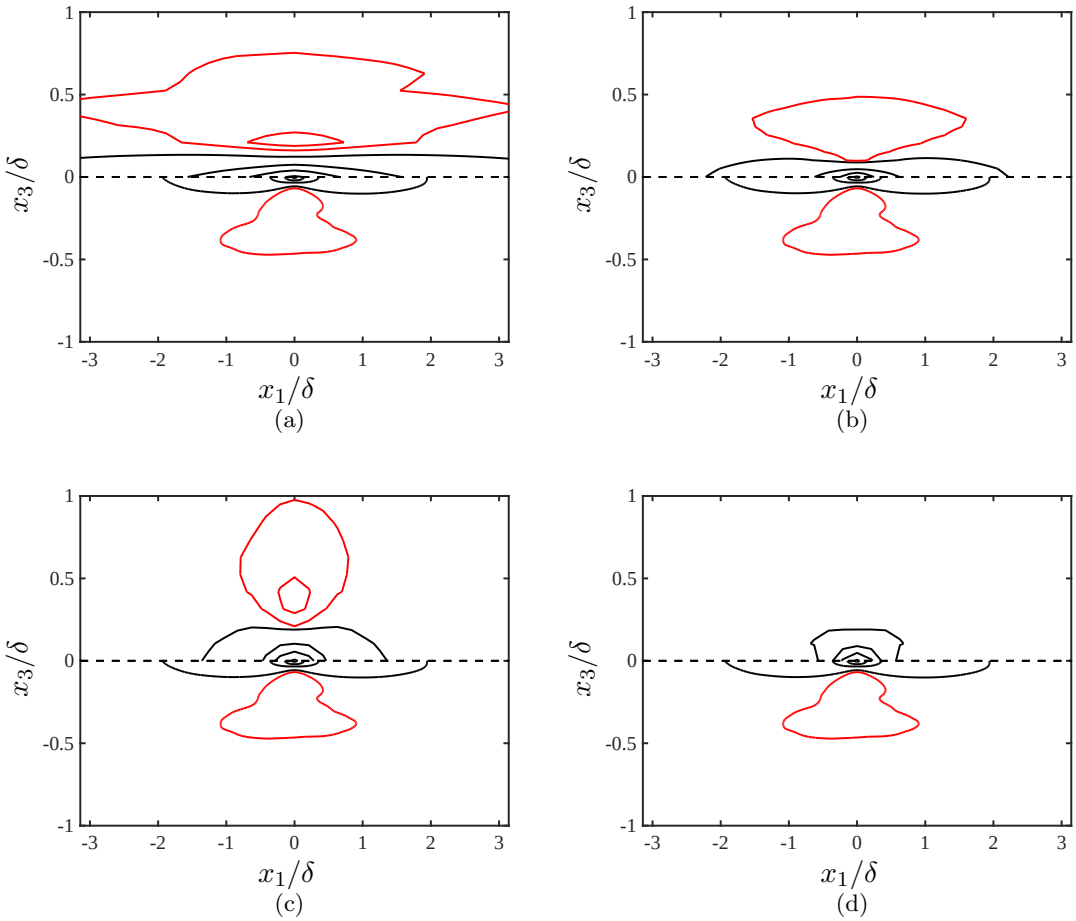

Figure 4.13: Auto-correlations of the streamwise velocity component at $x_2^+ \approx 15$ for (a) NS-550-s, (b) NS-550-s-f, (c) SL-550-u, and (d) NS-550-u. The upper half of the auto-correlation is for LES and the lower half for DNS. Contour lines are for positive correlations of 5% and 35% of the maximum (——) and negative correlations of 2% and 7 % of the maximum (——).

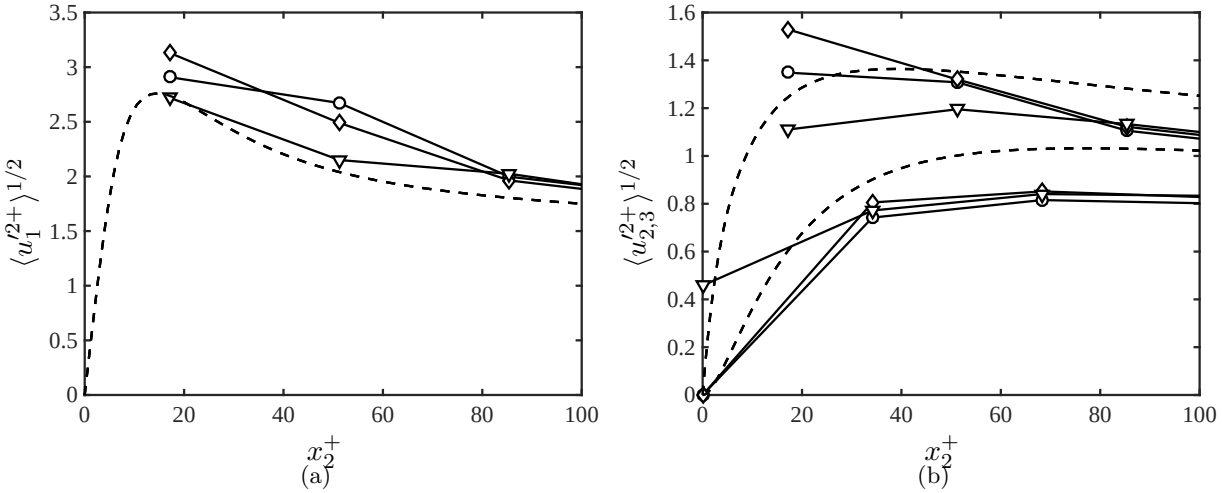

Figure 4.14: (a) Streamwise, (b) spanwise (top) and wall-normal (bottom) rms velocity fluctuations of $Re_\tau \approx 550$ for uniform grids with no-slip (○), Neumann (◊), and slip (▽) boundary condition. DNS given by (- - - ·).

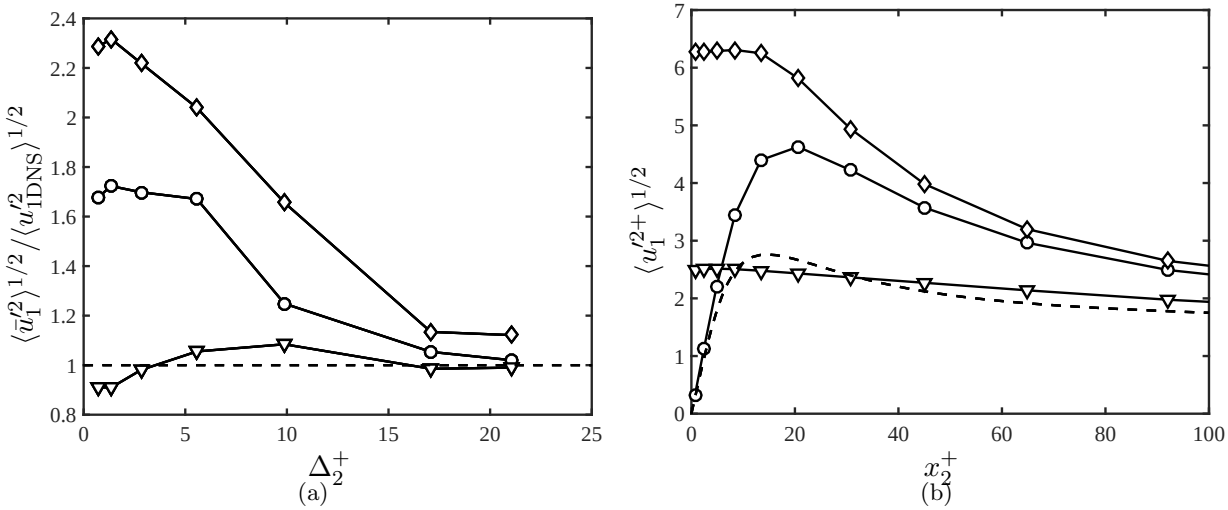

Figure 4.15: (a) Relative intensity of the streamwise rms peaks with respect to DNS as a function of Δ_2 at the wall and the (b) streamwise rms velocities for the most stretched mesh with $\Delta_2^+|_w = 1.41$ for the no-slip (○), Neumann (◊), and slip (▽) boundary condition. DNS given by (- - - ·).

condition. Regarding the production, the no-slip cases are characterized by a strong near-wall peak. On the contrary, this peak is absent for cases with slip, where most of the production is concentrated far from the wall. Similar results are observed for all slip cases shown in Figure 4.15(a). In the case of the Neumann boundary condition, the strong near-wall maxima in the production term is still present but is compensated by the turbulent transport term, which transports the excess energy away from the wall. This is only the case when the near-wall resolution bypasses the near-wall peaks. For Neumann cases with $\Delta_2^+ < 15$ in Figure 4.15(a), the magnitude of the turbulent transport term is reduced near the wall, while the strong peak in the production term persists (not shown).

The above results are consistent with the streak lengths observed in Figure 4.13 and it could be hypothesized that the excess of $\mathcal{P}+\mathcal{T}$ intensifies the streaks (stronger $\langle u_1'^{2+}\rangle$) while the lack of pressure strain reduces the distribution of the energy to the other two velocity components (weaker $\langle u_2'^{2+}\rangle$ and $\langle u_3'^{2+}\rangle$). This is further supported by the results in Figure 4.16(d), which shows that the ratio $\langle \mathcal{P}+\mathcal{T}\rangle/\langle \Pi\rangle$ approaches the DNS value for those cases where the under- and over-shoots of the rms velocity fluctuations are less pronounced.

4.4.4 Wall blocking effect

An additional cause of the problem may be attributed to the formation of splats due to the blocking effect of the wall. Splats are local regions of stagnation point flow resulting from fluid impinging on a wall and have been investigated in Perot and Moin [116]. Here we study the effect of the splats on the turbulence intensities by comparing cases NE-550-u (Neumann boundary condition with no transpiration) and SL-550-u (slip boundary condition with transpiration). The resulting rms velocity fluctuations are plotted in Figure 4.14. Note that $\langle \bar{u}_2'^{2+}\rangle$ is not zero at the wall for the slip case due to transpiration. Although not shown, for coarser grid resolutions, the required slip lengths to match the target Re_τ are larger, which leads to a larger variability in the transpiration velocities as well. As the grid is refined, the slip length (and hence $\langle \bar{u}_2'^{2+}\rangle$) approaches zero. The results in Figure 4.14 show that the blocking effect of the wall intensifies the splats, increasing the wall-parallel turbulence intensities near the wall. Compared to the traditional Neumann condition,

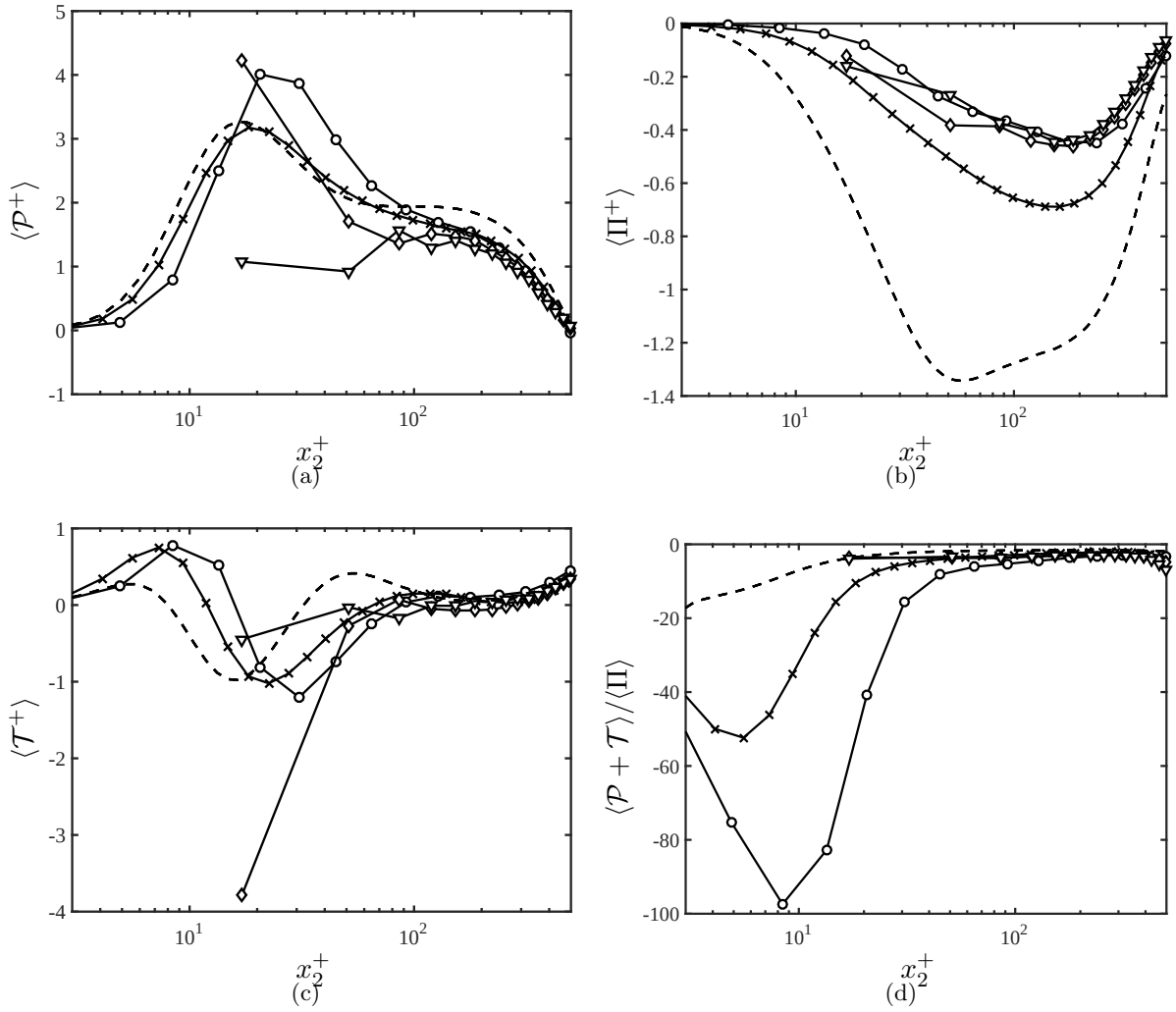

Figure 4.16: (a) Average production $\langle \mathcal{P} \rangle$, (b) pressure strain $\langle \Pi \rangle$, and (c) turbulent transport $\langle \mathcal{T} \rangle$ for the streamwise turbulence intensity budget, and (d) $\langle \mathcal{P} + \mathcal{T} \rangle / \langle \Pi \rangle$ for NS-550-s ($\circ$), NS-550-s-f ($\times$), NE-550-u ($\Diamond$), and SL-550-u ($\triangledown$). DNS given by (- - -).

better predictions of the streamwise velocity fluctuations are obtained when transpiration is allowed due to the local nonzero $\bar{u}_2$ which reduces the formation of splats.

4.5 Wall-stress invariant model

It is pertinent to discuss first the expected role of wall models in LES. From section 4.3.4 and previous analysis in the literature [72], the most important requirement for a wall model is to supply accurate mean tangential stress at the wall. This requirement must be accompanied by an effective SGS model responsible for generating correct turbulence statistics in the outer region, where the wall model plays a secondary role. The first requirement is necessary for obtaining the correct bulk velocity, whereas the last point is crucial to predict the shape of the mean velocity profile and rms velocity fluctuations far from the wall (see sections 4.3.2 and 4.3.5).

The wall models reviewed in the introduction are capable of meeting the first requirement by assuming a specific state of the boundary layer and relying on empirical parameters consistent with such state. In this regard, most traditional wall models assume quasi-equilibrium turbulence in the vicinity of the wall and encode explicitly or implicitly information about law of the wall which cannot be derived from first principles but only extracted from DNS or wind tunnel experiments, such as the values of κ and B. Despite the equilibrium-turbulence assumption, current wall-modeling approaches have been successful in predicting numerous flow configurations up to date, although their performance in some regimes such as transitional or separated flows as well as non-equilibrium turbulence is still open to debate.

The main purpose of a dynamic wall model is similar to that of traditional wall models, i.e., the estimation of accurate wall stress τ_w. However, the objective is to achieve this goal without prior assumptions regarding the state of the boundary layer or embedded empirical parameters. Instead, dynamic wall models aim to use only the current (local) state of the LES velocity field and universal modeling assumptions valid across different flow scenarios. Note that the task outlined above is an outstanding challenge, since without any empirical

coefficients there is no explicit reference to how the near-wall flow should behave in different situations. Moreover, the instantaneous velocity field is intertwined with the effects of the LES grid resolution, Reynolds number, and SGS model choice as documented in previous sections. Additionally, numerical errors are amplified at the wall, and discretization schemes are expected to play an important role as well. Dynamic models must encompass these factors in order to be of practical use, and whether this can be accomplished for arbitrary flow configurations remains to be demonstrated.

Despite the aforementioned difficulties, we provide below a dynamic slip model that shows the ability to adapt to different grid resolutions and Reynolds numbers as well as flow configurations, provided an SGS model. For a slip boundary condition of the form (4.1), the problem of estimating τ_w can be reformulated as finding the value of slip parameters that provides the correct wall stress. The relationship between l and τ_w was shown in sections 4.3.2 and 4.3.6 for channels and boundary layers. Moreover, for the slip boundary condition to be used as a predictive tool in wall-modeled LES, the computed l_i and v_i should comply with the observations discussed in the previous sections.

4.5.1 Previous dynamic models

Bose and Moin [13] introduced a dynamic wall model based on the slip boundary condition free of any *a priori* parameters. The slip length, assumed to be equal for the three spatial directions, is computed via a modified form of the Germano's identity [42],

$$l^2 \left(\Delta_R^2 \frac{\partial \tilde{\bar{u}}_i}{\partial n} \frac{\partial \tilde{\bar{u}}_j}{\partial n} - \frac{\partial \bar{u}_i}{\partial n} \frac{\partial \bar{u}_j}{\partial n} \right) + T_{ij}^{\mathrm{SGS}} - \widetilde{\tau_{ij}}^{\mathrm{SGS}} = \widetilde{\bar{u}_i \bar{u}_j} - \bar{u}_i \bar{u}_j, \tag{4.21}$$

where l is the slip length, $(\tilde{\cdot})$ is the test filter, Δ_R is the filter size ratio between the test and grid filters, τ_{ij}^{SGS} and T_{ij}^{SGS} represent the grid and test filter SGS tensors, respectively. Equation (4.21) is then solved for l by using least-squares.

In Bose and Moin [13], the model was tested for a series of LES of turbulent channel flow and NACA 4412 airfoil. However, our attempts to reproduce the channel flow results did not perform as expected with our current implementation, which uses a different SGS

model and numerical discretization. The discrepancies motivated a deeper study of the slip boundary condition and investigation of alternative dynamic wall-models as the one presented in the next section.

4.5.2 Wall-stress invariant dynamic wall model

We present a dynamic wall model based on the invariance of wall stress under filtering when the flow is in the statistically steady state. The physical rationale behind this assumption lies in the observation that, in LES, we aim to obtain the same wall stress regardless of the grid resolution (or filter). A similar approach was adopted by Anderson and Meneveau [2] for modeling rough walls.

As mentioned before, the problem of constructing a wall model consists of estimating the stress at the wall, τ_w, given the current and/or past states of the flow. An important observation is that the coupling of the wall model and the governing equations forms a dynamical system such that for a statistically steady flow, the equilibrium state must be stable and $\|\tau_w - \tau_w^{\mathrm{DNS}}\|$ is below the acceptable tolerance in some norm $\|\cdot\|$. For the slip boundary condition, an equivalent equilibrium state can be stated in terms of the slip lengths. We will refer to this condition as the stable-dynamical-model requirement.

We propose a procedure to build dynamic wall models based on the stable-dynamical-system requirement. In addition, we will impose four more model requirements, namely, that (R1) the model only uses information of flow quantities at the wall, (R2) the wall stress is imposed through a slip boundary condition, (R3) the wall is impermeable on average, and (R4) the dynamic model should only use up to two test filter levels.

Condition (R1) has a practical implication since wall models using information far from the wall are difficult (and ambiguous) to implement in complex geometries [179]. The use of condition (R2) is has been motivated in Sections 4.3 and 4.4. (R3) is an important constraint to support mass conservation as discussed in Section 4.3.6; however, in the case of a channel flow, no special treatment is required given the symmetry of the set-up (see Section 4.2.3). Regarding (R4), in the limit of the grids required for wall-modeled LES, increasing the levels of test filtering adds little information since most of the fluctuating

energy content is already lost.

If the slip boundary condition holds for both grid- and test-filtered velocity fields, then

$$l^2 \frac{\partial \bar{u}_i}{\partial n}\frac{\partial \bar{u}_j}{\partial n} - \tilde{l}^2 \frac{\partial \tilde{\bar{u}}_i}{\partial n}\frac{\partial \tilde{\bar{u}}_j}{\partial n} = \bar{u}_i\bar{u}_j - \tilde{\bar{u}}_i\tilde{\bar{u}}_j, \tag{4.22}$$

where $\tilde{l}$ is the slip length at the test filter level. We will assume a linear functional dependence of the slip length with the filter size of the form $\tilde{l} = \Delta_R l$. The actual *a posteriori* values for the optimal slip length (Eq. 4.15 with $l_1 = l_2$) as a function of grid resolution can be seen in Figure 4.18(c), which shows a close to linear relationship. The next step is to include a control term $\mathcal{F}_{ij}$ that is a function of the flow, in order to meet the stable-dynamical-model requirement,

$$l^2 \left(\frac{\partial \bar{u}_i}{\partial n}\frac{\partial \bar{u}_j}{\partial n} - \Delta_R^2 \frac{\partial \tilde{\bar{u}}_i}{\partial n}\frac{\partial \tilde{\bar{u}}_j}{\partial n} \right) = \bar{u}_i\bar{u}_j - \tilde{\bar{u}}_i\tilde{\bar{u}}_j + \mathcal{F}_{ij}. \tag{4.23}$$

To close the functional form of $\mathcal{F}_{ij}$, we will assume that it is only a function of the wall stress at different filter levels. Taking into account restriction (R4), there are six possible definitions of wall stress under test filtering,

$$\mathcal{T}_{ij}^1 = -\bar{u}_i\bar{u}_j - \tau_{ij}^{\mathrm{SGS}}\ (\bar{\mathbf{u}}) + 2\nu S_{ij}(\bar{\mathbf{u}}) - p(\bar{\mathbf{u}})\delta_{ij}, \tag{4.24}$$

$$\mathcal{T}_{ij}^2 = -\widetilde{\bar{u}_i\bar{u}_j} - \widetilde{\tau_{ij}}^{\mathrm{SGS}}(\bar{\mathbf{u}}) + 2\nu\widetilde{S_{ij}}(\bar{\mathbf{u}}) - \tilde{p}(\bar{\mathbf{u}})\delta_{ij}, \tag{4.25}$$

$$\mathcal{T}_{ij}^3 = -\tilde{\bar{u}}_i\tilde{\bar{u}}_j - \tau_{ij}^{\mathrm{SGS}}\ (\tilde{\bar{\mathbf{u}}}) + 2\nu S_{ij}(\tilde{\bar{\mathbf{u}}}) - p(\tilde{\bar{\mathbf{u}}})\delta_{ij}, \tag{4.26}$$

$$\mathcal{T}_{ij}^4 = -\widetilde{\widetilde{\bar{u}_i\bar{u}_j}} - \widetilde{\widetilde{\tau_{ij}}}^{\mathrm{SGS}}(\bar{\mathbf{u}}) + 2\nu\widetilde{\widetilde{S_{ij}}}(\bar{\mathbf{u}}) - \tilde{\tilde{p}}(\bar{\mathbf{u}})\delta_{ij}, \tag{4.27}$$

$$\mathcal{T}_{ij}^5 = -\widetilde{\tilde{\bar{u}}_i\tilde{\bar{u}}_j} - \widetilde{\tau_{ij}}^{\mathrm{SGS}}(\tilde{\bar{\mathbf{u}}}) + 2\nu\widetilde{S_{ij}}(\tilde{\bar{\mathbf{u}}}) - \tilde{p}(\tilde{\bar{\mathbf{u}}})\delta_{ij}, \tag{4.28}$$

$$\mathcal{T}_{ij}^6 = -\tilde{\tilde{\bar{u}}}_i\tilde{\tilde{\bar{u}}}_j - \tau_{ij}^{\mathrm{SGS}}\ (\tilde{\tilde{\bar{\mathbf{u}}}}) + 2\nu S_{ij}(\tilde{\tilde{\bar{\mathbf{u}}}}) - p(\tilde{\tilde{\bar{\mathbf{u}}}})\delta_{ij}, \tag{4.29}$$

where $\mathcal{T}_{ij}^k$ is the wall stress tensor at different filter levels, and τ_{ij}^{SGS}, S_{ij} and $p\delta_{ij}$ are the subgrid stress, the strain-rate and pressure tensors, respectively, computed from the specified (test- or grid-filtered) velocity field. The wall stress τ_w can be computed as the norm of the projection of $\mathcal{T}_{ij}^k$ onto the wall-normal direction. The formulation above also

allows to account for different types of walls by adding the appropriate drag term to the right-hand side of Eqs. (4.24-4.29).

Then, a family of dynamic wall models can be formulated as

$$l^2 \left(\frac{\partial \bar{u}_i}{\partial n} \frac{\partial \bar{u}_j}{\partial n} - \Delta_R^2 \frac{\partial \tilde{\bar{u}}_i}{\partial n} \frac{\partial \tilde{\bar{u}}_j}{\partial n} \right) = \bar{u}_i \bar{u}_j - \tilde{\bar{u}}_i \tilde{\bar{u}}_j + a_k \mathcal{T}_{ij}^k, \tag{4.30}$$

where a_k are constants that need to be specified. In order to limit the parameter space of a_k, we limit the constant a_k to have values equal to -1, 0 or 1.

Finally, the model from Eq. (4.30) needs to satisfy the stable-dynamical-model requirement in order to be usable. This condition can be formally expressed as

$$\begin{cases} \text{a) If } \tau_w \approx \tau_w^{\text{DNS}}, \text{ then } a_k \mathcal{T}_{ij}^k \approx 0, \\ \text{b) If } \tau_w > \tau_w^{\text{DNS}}, \text{ then } a_k \mathcal{T}_{ij}^k < 0 \text{ for } t > t_c, \\ \text{c) If } \tau_w < \tau_w^{\text{DNS}}, \text{ then } a_k \mathcal{T}_{ij}^k > 0 \text{ for } t > t_c, \end{cases} \tag{4.31}$$

where t is time and t_c is a characteristic time scale of the flow to adapt to changes in the boundary condition. Condition a) implies that the change in the predicted l for the next step should be minimal when starting from a flow configuration where $\tau_w \approx \tau_w^{\text{DNS}}$. This is achieved by $a_k \mathcal{T}_{ij}^k \approx 0$. In Section 4.3.2, we show that increasing l results in increasing τ_w, and vice versa. Hence, conditions b) and c) are related to the stability of the model and are necessary to guarantee that the predicted slip length drives the flow in the correct direction. For example, when $\tau_w > \tau_w^{\text{DNS}}$, l at the next step should decrease (that is, $a_k \mathcal{T}_{ij}^k < 0$), and when $\tau_w < \tau_w^{\text{DNS}}$, l must increase ($a_k \mathcal{T}_{ij}^k > 0$). In addition, the invariance of wall stress under test filtering is taken into account by imposing $\sum_k a_k = 0$, which is also required in order to guarantee that the wall models revert to the no-slip boundary condition as the grid size $\Delta \to 0$.

The system in Eq. (4.30) is over-determined and l is computed via least-squares. For incompressible flows, the isotropic part τ_{ij}^{SGS} is usually not defined by the SGS models. Since the system is already over-determined, we will exclude the $i = j$ components of Eq. (4.30).

Ideally, we would like to construct a dynamic wall model of the form (4.30) that satisfies condition (4.31), where the coefficients a_i are determined based only on first principles. However, the task is quite challenging due to the highly non-linear nature of the Navier-Stokes equations, and it is difficult to assess whether condition (4.31) will be satisfied *a priori* once the wall model is coupled with the flow. Furthermore, this condition must hold for a broad range of equilibrium and non-equilibrium flow configurations of interest. Instead, to make the problem tractable, we will evaluate models in Eq. (4.30) *a posteriori* by considering only three reference channel flow simulations at $Re_\tau \approx 4200$ with DSM and grid resolution $\Delta_1 = \Delta_2 = \Delta_3 = 0.050$. The first case, C1, is computed using the optimal slip length, $l_{c1} = l_{\text{opt}}$. In a channel flow with transpiration, the wall stress is given by Eq. (4.14). If τ_w^{DNS} is known, l_{opt} is easily obtained by introducing the slip boundary condition (4.1) in the term $\langle \bar{u}_1 \bar{u}_2 \rangle|_w$, and the resulting equation for l_{opt} is

$$l_{\text{opt}}^2 = \frac{\nu \left\langle \partial \bar{u}_1 / \partial x_2 \right\rangle|_w - \left\langle \tau_{12}^{\text{SGS}} \right\rangle\big|_w - \tau_w^{\text{DNS}}}{\langle (\partial \bar{u}_1 / \partial x_2)(\partial \bar{u}_2 / \partial x_2) \rangle}. \tag{4.32}$$

Note that Eq. (4.32) is not a wall model itself but rather a compatibility condition that links the stress at the wall with the slip length. The second and third cases, denoted by C2 and C3, are analogous to C1 but with $l_{c2} = 1.35\langle l_{\text{opt}} \rangle$ and $l_{c3} = 0.65\langle l_{\text{opt}} \rangle$, respectively.

We proceed to evaluate the performance of different dynamic wall models using condition (4.31) with $t_c = 0$. Starting from cases C1, C2 and C3, we compute the slip length at the next time step, l_{c1}^m, l_{c2}^m, and l_{c3}^m, evaluated from all possible models in the family (4.30). Condition (4.31a) can be quantified by $\epsilon_{c1} = |l_{c1}^m - l_{c1}|/l_{c1}$. Conditions (4.31b) and (4.31c) can be similarly quantified by $\epsilon_{c2} = (l_{c2} - l_{c2}^m)/l_{c2}$ and $\epsilon_{c3} = (l_{c3}^m - l_{c3})/l_{c3}$. For a model to be viable, it is necessary that $\epsilon_{c1} \ll 1$ and $\epsilon_{c2}, \epsilon_{c3} > 0$. We defined the "best" model as the one with $\epsilon_{c1} < 0.05$ and maximum $\epsilon_{c2} + \epsilon_{c3}$. Additionally, in order for the model to be less sensitive to the filter size ratio, the above requirements should hold for both $\Delta_R = 1.6$ and 1.8. After a search over all possible models complying with our constraints, the wall-stress

invariant model (WSIM) for the slip boundary condition is given by the modeling choice

$$\mathcal{F}_{ij} = \mathcal{T}^1_{ij} - \mathcal{T}^3_{ij} - \mathcal{T}^5_{ij} + \mathcal{T}^6_{ij}, \tag{4.33}$$

such that l is computed from

$$l^2 \left(\frac{\partial \bar{u}_i}{\partial n} \frac{\partial \bar{u}_j}{\partial n} - \Delta_R^2 \frac{\partial \tilde{\bar{u}}_i}{\partial n} \frac{\partial \tilde{\bar{u}}_j}{\partial n} \right) = \bar{u}_i \bar{u}_j - \tilde{\bar{u}}_i \tilde{\bar{u}}_j + \mathcal{T}^1_{ij} - \mathcal{T}^3_{ij} - \mathcal{T}^5_{ij} + \mathcal{T}^6_{ij}, \tag{4.34}$$

which can be rewritten as

$$l^2 \mathcal{M}_{ij} = \mathcal{R}_{ij} + \mathcal{F}_{ij} \tag{4.35}$$

with

$$\mathcal{M}_{ij} = \frac{\partial \bar{u}_i}{\partial n} \frac{\partial \bar{u}_j}{\partial n} - \Delta_R^2 \frac{\partial \tilde{\bar{u}}_i}{\partial n} \frac{\partial \tilde{\bar{u}}_j}{\partial n}, \quad \mathcal{R}_{ij} = \bar{u}_i \bar{u}_j - \tilde{\bar{u}}_i \tilde{\bar{u}}_j, \tag{4.36}$$

The least-squares process can be written as

$$l^2 = \frac{(\mathcal{R}_{ij} + \mathcal{F}_{ij}) \mathcal{M}_{ij}}{\mathcal{M}_{ij} \mathcal{M}_{ij}} = \frac{\mathcal{R} + \mathcal{F}}{\mathcal{M}}, \tag{4.37}$$

where repeated indices imply summation and the compact notation $\mathcal{R} = \mathcal{R}_{ij}\mathcal{M}_{ij}$, $\mathcal{F} = \mathcal{F}_{ij}\mathcal{M}_{ij}$, and $\mathcal{M} = \mathcal{M}_{ij}\mathcal{M}_{ij}$ is used.

Note that the first part of the right-hand-side of (4.30), $\bar{u}_i \bar{u}_j - \tilde{\bar{u}}_i \tilde{\bar{u}}_j$ ($\mathcal{R}_{ij}$), is the result of applying the boundary condition at the grid and test filter levels. The remaining terms, $\mathcal{T}^1_{ij} - \mathcal{T}^3_{ij} - \mathcal{T}^5_{ij} + \mathcal{T}^6_{ij}$ ($\mathcal{F}_{ij}$), then act as an effective control such that the slip length increases if the current wall stress is under-predicted, and decreases if the wall stress is over-predicted. This self-regulating mechanism can be examined by analyzing the terms $\mathcal{M}$, $\mathcal{R}$, and $\mathcal{F}$ for three test cases C1, C2, and C3. The terms $\mathcal{M}$, $\mathcal{R}$, and $\mathcal{F}$ were evaluated after the cases were run with their corresponding slip lengths fixed in time until the statistically steady state was reached. Note that the term $\mathcal{R}$ can be interpreted as the model prior to applying the control mechanism, and this allows us to define two slip lengths, namely, $l_{\mathcal{R}} = \mathcal{R}/\mathcal{M}$ and $l_{\mathcal{R}+\mathcal{F}} = (\mathcal{R} + \mathcal{F})/\mathcal{M}$.

The terms $\mathcal{M}$, $\mathcal{R}$, and $\mathcal{R} + \mathcal{F}$ evaluated from the three test cases are plotted in figure

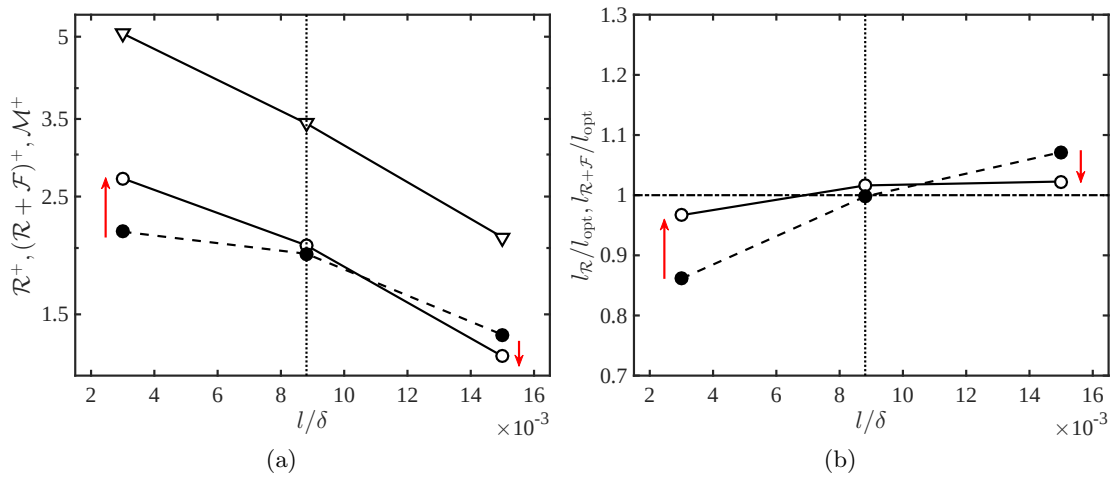

Figure 4.17: (a) $\mathcal{R}$ (●), $\mathcal{R}+\mathcal{F}$ (○), and $\mathcal{M}$ (▽) computed from channel LES using the slip boundary condition with fixed l equal to $l = 0.35l_{\rm opt} = 0.003\delta$, $l = l_{\rm opt} = 0.009\delta$, and $l = 1.70l_{\rm opt} = 0.015\delta$. (b) The slip lengths $l_{\mathcal{R}}$ (●), $l_{\mathcal{R}+\mathcal{F}}$ (○) normalized by the optimal slip length. Δ_R was assigned to be 1.6. The vertical dotted lines are $l = l_{\rm opt}$. Red arrows highlight the improvement achieved by including the control term $\mathcal{F}_{ij}$. See text for more details.

4.17(a), and the corresponding slip lengths $l_{\mathcal{R}}$ and $l_{\mathcal{R}+\mathcal{F}}$ in figure 4.17(b). The results show that application of WSIM recovers the optimal slip length, and thus the correct wall stress, through the control mechanism $\mathcal{F}_{ij}$. The analysis provided here is performed *a priori*, that is, the wall model was used to predict l at time $t + \Delta_t$ for a given flow field at time t, but without an actual dynamic coupling between WSIM and LES. The remainder of the chapter is devoted to test WSIM in real LES under different test scenarios.

4.6 Performance of the wall-stress invariant model

4.6.1 Test cases

To test the performance of WSIM, three flow configurations are considered: a statistically steady plane turbulent channel (2-D channel), a non-equilibrium three-dimensional transient channel (3-D channel), and a zero-pressure-gradient flat-plate turbulent boundary layer. The numerical methods of the simulations are the same as the ones given in sections 4.3.1

and 4.3.6. The 2-D channel flow and the turbulent boundary layer was discussed in section 4.3. The three-dimensional transient channel flow is a temporally developing turbulent boundary layer in a planar channel subjected to a sudden spanwise forcing as in Moin et al. [105].

The size of the 2-D and 3-D channel domain is $8\pi\delta \times 2\delta \times 3\pi\delta$ in the streamwise, wall-normal and spanwise directions, respectively. For both 2-D and 3-D channel flows, periodic boundary conditions are applied in the streamwise and spanwise directions. For the top and bottom walls, we impose either the no-slip (NS), slip boundary condition for WSIM, or Neumann boundary condition for cases with the equilibrium wall model (EQWM). The formulation for the EQWM follows Kawai and Larsson [60] with a matching location at the third grid cell for the streamwise velocity, although recent studies have shown that the first grid cell may be used for the EQWM when the velocities are filtered using a spatial or temporal filter [179] following the methodology first introduced for algebraic wall models [16].

For the 2-D channel, the flow is driven by imposing a constant mean pressure gradient and the simulations are started from a random initial condition run for at least $100\delta/u_\tau$ after transients. In the case of the 3-D channel, the calculations were started from a 2-D fully developed plane channel flow driven by a streamwise mean pressure gradient. The subsequent calculations were performed with a transverse (spanwise) mean pressure gradient of $\partial\langle p\rangle/\partial x_3 = 10\tau_w^{2D}/\delta$, where τ_w^{2D} is the mean wall shear stress of the unperturbed channel. The 3-D channel simulations were run for $10u_{\tau 0}/\delta$ and averaged over seven realizations, where $u_{\tau 0}$ is the friction velocity of the 2-D initial condition.

For the boundary layer, the setup is identical to the one in section 4.3.6, where the range of Re_θ is from 1000 to 10,000. The length, height and width of the simulated box are $L_1 = 1060\theta_{\text{avg}}$, $L_2 = 18\theta_{\text{avg}}$, and $L_3 = 35\theta_{\text{avg}}$ with the streamwise and spanwise resolutions of $\Delta_1^+ = 118$ and $\Delta_3^+ = 84.3$ at $Re_\theta \approx 6500$. The grid is slightly stretched in the wall-normal direction with minimum $\Delta_2^+ = 20.8$. The inlet, outlet, and top boundary conditions are as in section 4.3.6 with $x_{\text{ref}}/\theta_0 = 890$. For the bottom wall, we impose the slip boundary condition for WSIM.

Grid label	Δ_1/δ	Δ_2/δ	Δ_3/δ
G0	0.080	0.080	0.080
G1	0.050	0.050	0.050
G2	0.025	0.025	0.025

Table 4.3: Grid resolutions in outer units. The first column contains the label used to name LES cases for the 2–D and 3–D channel flow simulations computed with different grids. The second, third, and fourth columns are the streamwise, wall-normal, and spanwise grid resolutions, respectively.

It is important to note the details of the filter operation, as dynamic wall models are particularly sensitive to this choice (see section 4.6.2). Test filtering a variable f in a given spatial direction at point i is computed as $1/6f(i-1)+2/3f(i)+1/6f(i+1)$ (Simpson's rule). The operation is repeated for all three directions away from the wall. This corresponds to a discrete fourth-order quadrature over a cell of size $2\Delta_1 \times 2\Delta_2 \times 2\Delta_3$ for a uniform grid, where Δ_1, Δ_2 and Δ_3 are the grid sizes in the three directions, respectively. At the wall, the same filtering operation is used in the horizontal directions while the wall-normal filter is one-sided and given by $2/3f(1) + 1/3f(2)$, with $f(1)$ and $f(2)$ denoting values at the first and second wall-normal grid points. This is an integration over a cell of size $2\Delta_1 \times \Delta_2 \times 2\Delta_3$. Also, the definition of the filter operation fixes the value of Δ_R, which is the ratio between the grid and test filter sizes at the wall. In this case, the Δ_R based on the cell volume is given by $\sqrt[3]{2 \times 1 \times 2} \approx 1.6$.

The cases for the 2-D and 3-D channel are labeled in following the convention ([Channel type]-[Wall model]-[Reynolds number]-[Grid]), where the grid labels G0, G1, and G2 given in table 4.3 correspond to $320 \times 25 \times 120$ ($\Delta_1 = \Delta_2 = \Delta_3 = 0.080\delta$), $512 \times 40 \times 192$ ($\Delta_1 = \Delta_2 = \Delta_3 = 0.050\delta$), and $1024 \times 80 \times 384$ ($\Delta_1 = \Delta_2 = \Delta_3 = 0.025\delta$), respectively. The wall model applied are labeled NS, EQWM, WSIM. Additional cases with anisotropic grids, different values of Δ_R, test-filtering operations, or SGS model were run to study the sensitivity of the model to these choices. They are discussed in section 4.6.2.

The 2-D channel results are compared with DNS data from Hoyas and Jiménez [48] and Lozano-Durán and Jiménez [80] for $Re_\tau \approx 2000$ and 4200, Yamamoto and Tsuji [177] for

$Re_\tau \approx 8000$, and with the law-of-the wall for $Re_\tau > 8000$. For the boundary layer, the resulting friction coefficient is compared to the empirical C_f from White and Corfield [173], and the mean velocity profiles are compared with the DNS data from Sillero et al. [141] at $Re_\theta \approx 6500$ and the experimental data from Österlund [111] at $Re_\theta \approx 8000$.

The performance of the WSIM in laminar flows has not been studied. However, in the limit of fine grids, the dynamic procedure of WSIM should produce zero slip lengths and revert to the no-slip boundary condition. Thus, for laminar cases with enough grid resolution to resolve the near-wall structures, we expect the dynamic wall model to naturally switch off.

4.6.2 Statistically steady two-dimensional channel flow

We assess the performance of WSIM compared to EQWM and NS. The results are discussed in terms of the error in the streamwise mean velocity profile across the logarithmic region. This choice was necessary in order to include higher Reynolds number cases where the corresponding DNS was not available and the law of the wall is used instead. Restricting the error to be evaluated only in the logarithmic layer is justified as wall models mainly impact the solution by vertically shifting the mean velocity profile and do not alter its shape for the range of grid resolutions tested as shown in section 4.3.3. In particular, the error in the mean profile is measured as the normalized L_2 error of the streamwise mean velocity profile between the second grid point and 0.2δ.

$$\mathcal{E}_m = \left[\frac{\int_{\Delta_2}^{0.2\delta} \left(\langle \bar{u}_1 \rangle - \langle u_1^{\mathrm{DNS}} \rangle \right)^2 \mathrm{d}x_2}{\int_{\Delta_2}^{0.2\delta} \left(\langle u_1^{\mathrm{DNS}} \rangle \right)^2 \mathrm{d}x_2} \right]^{1/2}. \tag{4.38}$$

In the case where the corresponding DNS does not exist, $\langle u_1^{\mathrm{DNS}} \rangle$ is replaced by the law of the wall,

$$\langle u_1^{\mathrm{DNS}} \rangle = \frac{1}{\kappa} \log x_2^+ + B, \tag{4.39}$$

with $\kappa = 0.392$ and $B = 4.48$ [83].

Figure 4.18(a) and (b) shows $\mathcal{E}_m$ as a function of grid resolution and Reynolds number.

At moderate Reynolds numbers ($Re_\tau < 8000$) and all grid resolutions, the error for WSIM ($\mathcal{E}_m$ ∼2-6%) is similar to that of the EQWM ($\mathcal{E}_m$ ∼2-4%). With increasing Reynolds number, the performance degrades (up to $\mathcal{E}_m$ ∼15% at Re_τ ≈100,000), while the EQWM does not. The accurate results for EQWM are not surprising as its modeling assumptions are well satisfied for channel flow settings. The declining performance of WSIM at very high Reynolds number is probably connected to the discussion in section 4.2.1 where it was argued that the underlying assumptions for the slip condition are invalidated for large filter sizes. However, it is worth mentioning that the errors for an LES with no wall model ($\mathcal{E}_m$ ≈100% for 2D-NS-4200-G1) are an order of magnitude larger than the errors of WSIM for all cases. The mean velocity profiles and streamwise rms velocity fluctuations for WSIM for various cases are shown in Figure 4.19.

The slip lengths predicted by WSIM are shown in Figure 4.18(c) and (d) as a function of Reynolds number and grid resolution and compared to the optimal slip lengths. It is remarkable that WSIM captures the overall behavior of the optimal slip lengths, that is, a strong dependence on grid resolution and a weak variation with Reynolds number.

Four additional cases were computed to analyze the sensitivity of the WSIM to Δ_R, grid anisotropy, shape of the test filter, and choice of SGS model. The effect of Δ_R turned out to be negligible for the plausible range of values $\Delta_R = [1.4, 1.8]$, and the measured difference in $\mathcal{E}_m$ was less than 1%. Regarding grid anisotropy, coarsening case 2D-WSIM-4200-G1 by a factor of two in only the streamwise or spanwise direction had a negligible effect on $\mathcal{E}_m$. While coarsening in both the streamwise and spanwise directions simultaneously by a factor of two had a larger effect with $\mathcal{E}_m$ increasing to ∼8%. The error trend for anisotropic grids also follows the results shown in Fig. 4.18 (a) when scaled with grid size based on cell volume, Δ. This shows that the wall model is robust to mild grid anisotropies.

On the contrary, the test filter shape and SGS model highly impacted the prediction of the mean flow. Case 2D-WSIM-4200-G1 was repeated using test filter based on the trapezoidal rule, and the error increased from 2.5% to 32%. When 2D-WSIM-4200-G1 was run using the anisotropic minimum-dissipation (AMD) model, the stress provided by the SGS model τ_{12}^{SGS} was larger than u_τ^2, and the slip length prediction by WSIM was clipped to

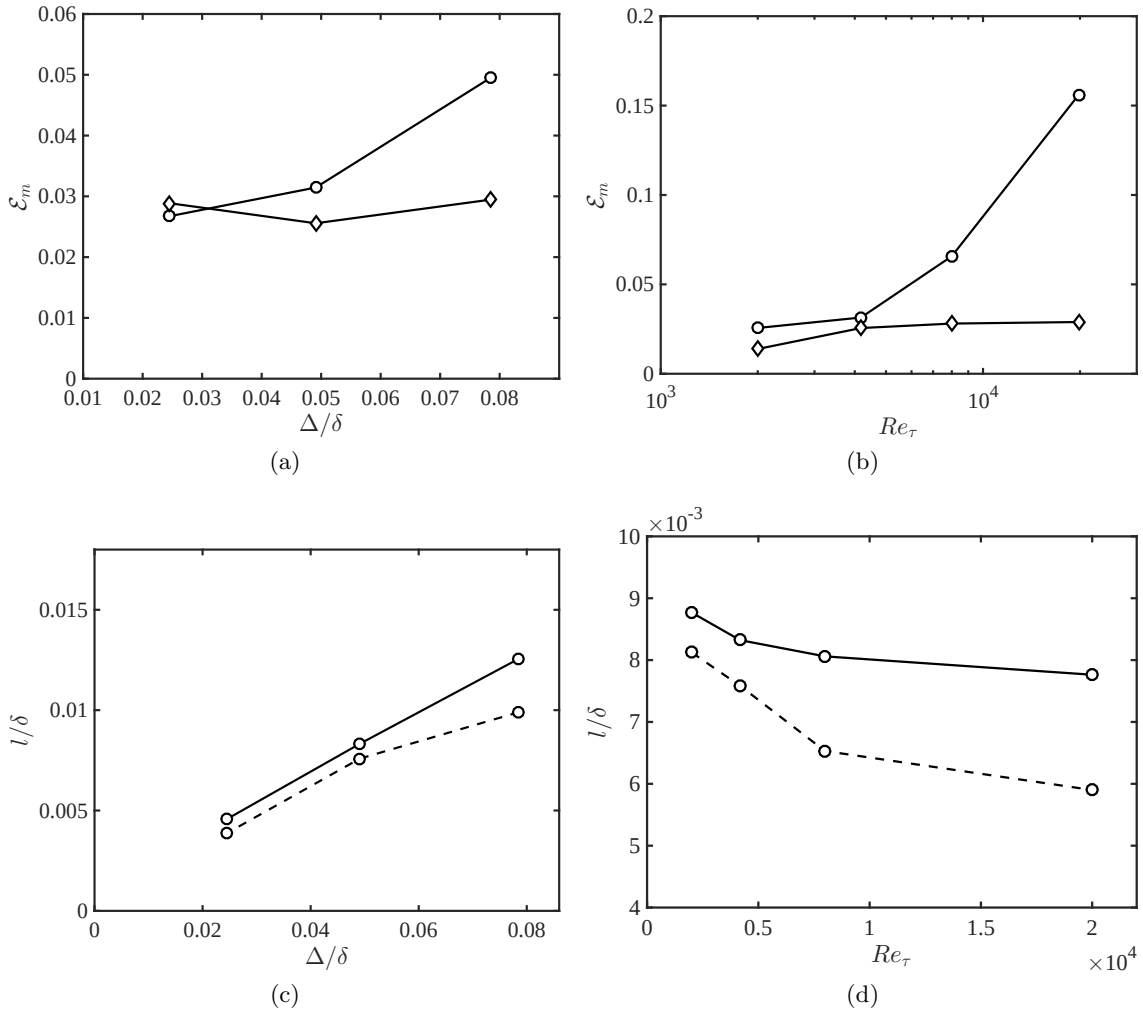

Figure 4.18: Error in the streamwise mean velocity profile, $\mathcal{E}_m$, as a function of (a) grid size (for $Re_\tau = 4200$) and (b) Reynolds number (for grid G1) for WSIM (○) and EQWM (◊). The slip lengths l/δ for WSIM (——) and optimal slip lengths (- - - ·) as a function of (c) grid resolution for $Re_\tau = 4200$ and (d) Reynolds number for grid G1.

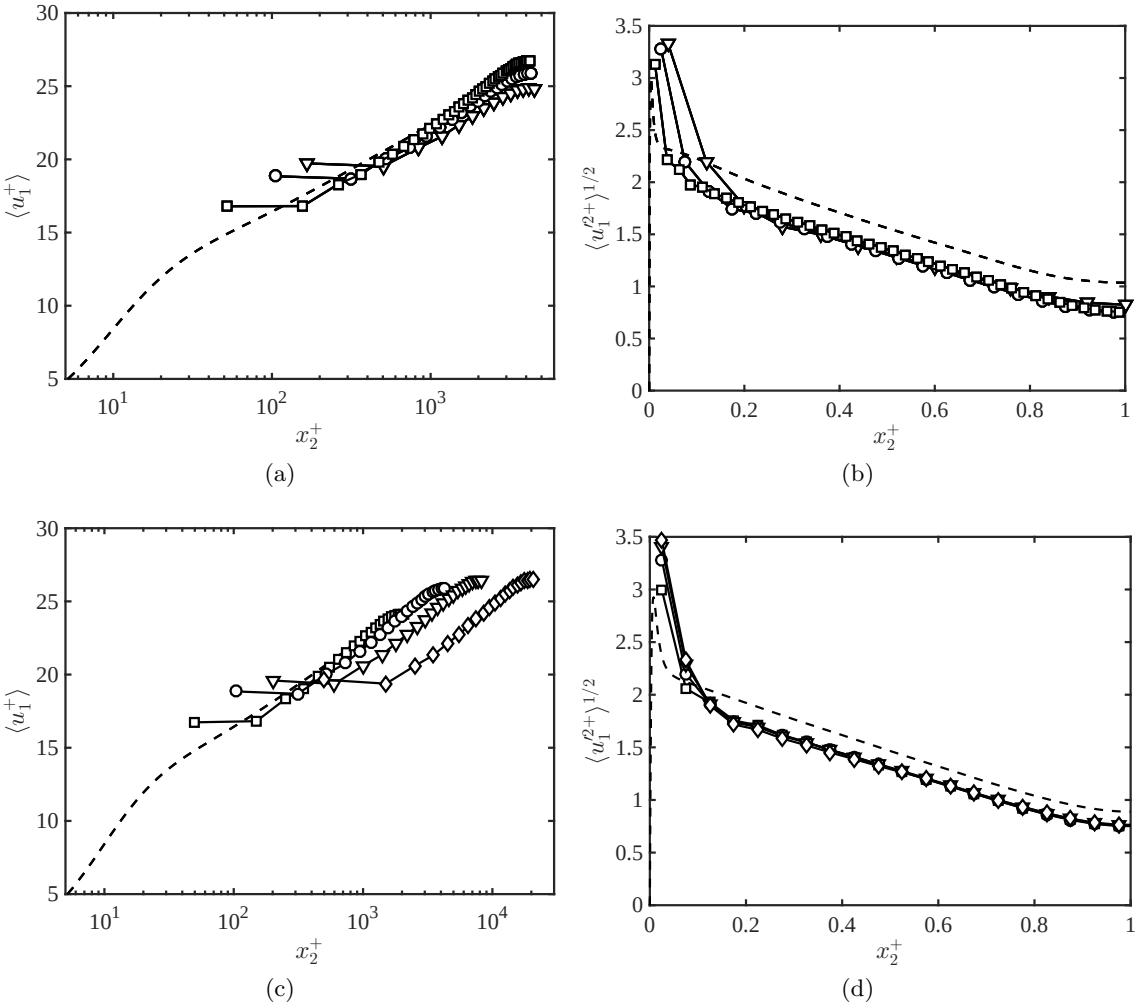

Figure 4.19: (a) Mean velocity profiles and (b) streamwise rms velocity fluctuations for WSIM at $Re_\tau \approx 4200$ for grid G0 ($\triangledown$), G1 ($\circ$), and G2 ($\square$). DNS for $Re_\tau \approx 4200$ (- - - ·). (b) Mean velocity profiles and (b) streamwise rms velocity fluctuations for WSIM at $Re_\tau \approx 2000$ ($\square$), 4200 ($\circ$), 8000 ($\triangledown$), and $20,000$ ($\Diamond$) for grid G1. DNS for $Re_\tau \approx 4200$ (- - - ·).

zero due to the excess of wall stress, reverting the boundary condition to no-slip. Although this is consistent with the fact that $\tau_{12}^{\mathrm{SGS}} > u_\tau^2$, it also implies that the correct stress at the wall can never be obtained through the slip boundary condition with a single slip length in this case. It was shown in section 4.3 that the slip lengths in the wall-normal direction must be larger than the wall-parallel ones in order to drain the excess of stress supplied by the SGS model. This suggests that WSIM should be generalized to a formulation with a different slip length in each spatial direction to overcome this limitation. It also remains to study the near-wall behavior of various SGS models in the wall-modeled grid limits in more detail.

4.6.3 Three-dimensional transient channel flow

The performance of WSIM in non-equilibrium scenarios is assessed in a three-dimensional transient channel flow [105]. Note that in general RANS-based wall models cannot be assumed to be effective at transferring information from the inner to the outer layer in non-equilibrium flows. Hence, the current flow set up, characterized by a spanwise boundary layer growing from the wall due to viscous effects, is expected to be problematic for wall-modeled LES. A plane channel flow was modified to incorporate a lateral (transverse) pressure gradient 10 times that of the streamwise pressure gradient. The details of the simulations were given in section 4.6.1.

The wall models explored are WSIM and EQWM. A case with the no-slip boundary condition is used for control, and the figure of merit is the evolution of the streamwise and spanwise wall stress as a function of time (Figure 4.20). Note that the temporal increment of the wall stress magnitude involves an increase of the Reynolds number from $Re_\tau \approx 932$ at $t = 0$ to $Re_\tau \approx 2600$ at $t = 10\delta/u_{\tau 0}$. The results show that the performance of WSIM is similar to the EQWM despite its parameter-free nature. The streamwise and spanwise mean velocity profiles at various time instances are given in Figure 4.21, which show that both WSIM and EQWM predict similar time evolution. testing the capabilities of WSIM in transient flows. Although there is no reference DNS available for comparison for the full time span of our simulations, in the limited time range from $t = 0$ to $1\delta/u_{\tau 0}$, Giometto

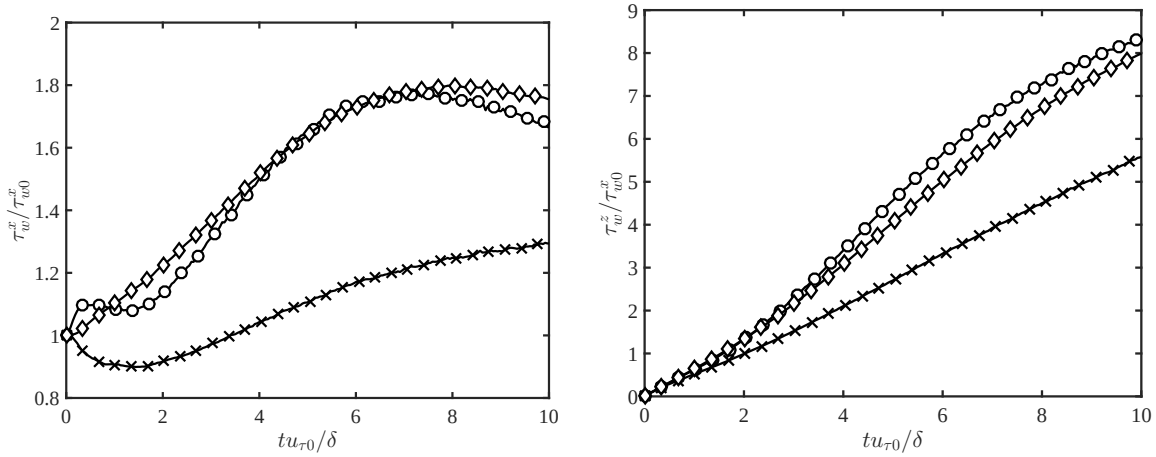

Figure 4.20: Wall stress in (a) streamwise and (b) spanwise directions as a function of time for WSIM (○), EQWM (◊), and NS (×).

et al. [47] showed that the EQWM predicts the evolution with less than 10% deviation in the spanwise wall stress prediction from DNS, and thus the results from WSIM are also expected to exhibit a similar error. Both the EQWM and WSIM entail a quantitative correction to the prediction provide by the no-slip boundary condition. Consequently, the computational simplicity and absence of a secondary mesh makes WSIM an appealing approach at the cost of a moderate attenuation of the predictive capabilities compared to more sophisticated wall models.

4.6.4 Zero-pressure-gradient flat-plate turbulent boundary layer

Finally, the performance of WSIM is assessed in a flat-plate turbulent boundary layer. The friction coefficient is shown in Figure 4.22 from $Re_\theta = 1000$ to 10,000. Note that the recycling scheme of Lund et al. [86] imposes an artificial boundary condition at the inlet, requiring an initial development region for the flow to fully adapt to the slip boundary condition, which is the reason for the discrepancy in C_f near the inlet. Consistent with previous test cases, the results show that WSIM predicts the friction coefficient well within 4% error for $Re_\theta > 6000$. The mean streamwise velocity profile at $Re_\theta \approx 6500$ and 8000 and

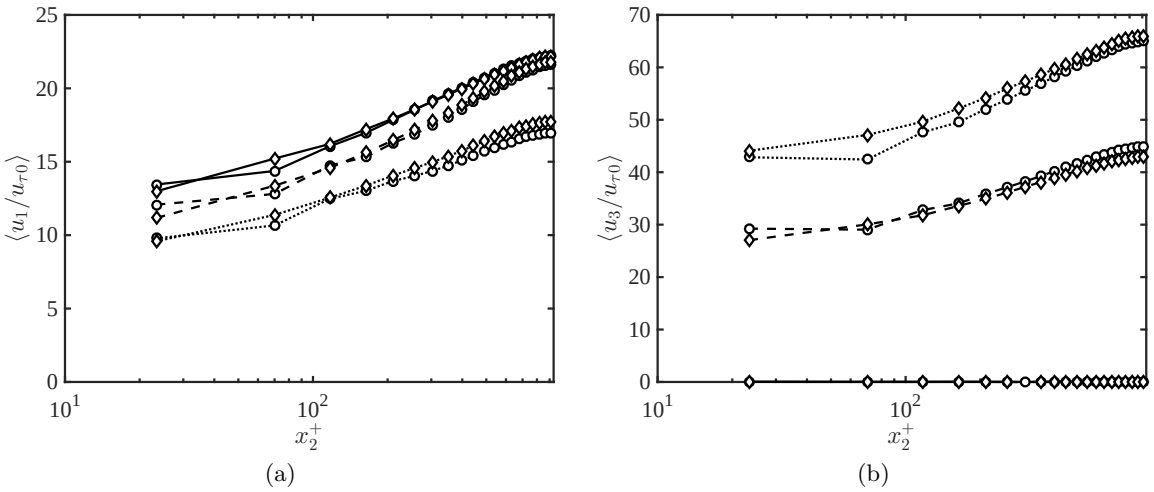

Figure 4.21: Mean (a) streamwise and (b) spanwise velocity profile as a function of x_2/δ at $tu_{\tau 0}/\delta = 0$ (——), 4.5 (- - - ·), and 9 (·····) for WSIM (○) and EQWM (◊).

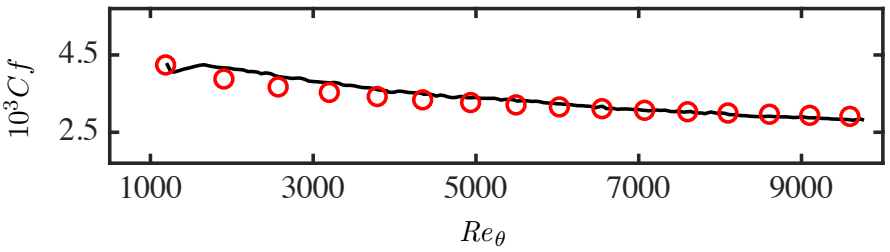

Figure 4.22: Friction coefficient from WSIM (——) and the empirical friction coefficient from White and Corfield [173] (○).

the rms velocity fluctuations at $Re_\theta \approx 6500$ are also well predicted as reported in Figure 4.23.

4.7 Summary

Due to the scaling of grid resolution requirements in DNS and wall-resolved LES, wall-modeled LES stands as the most viable approach for most engineering applications. In most existing wall-models, the Dirichlet no-slip boundary condition at the wall is replaced by a Neumann and no-transpiration conditions in the wall-parallel and wall-normal directions,

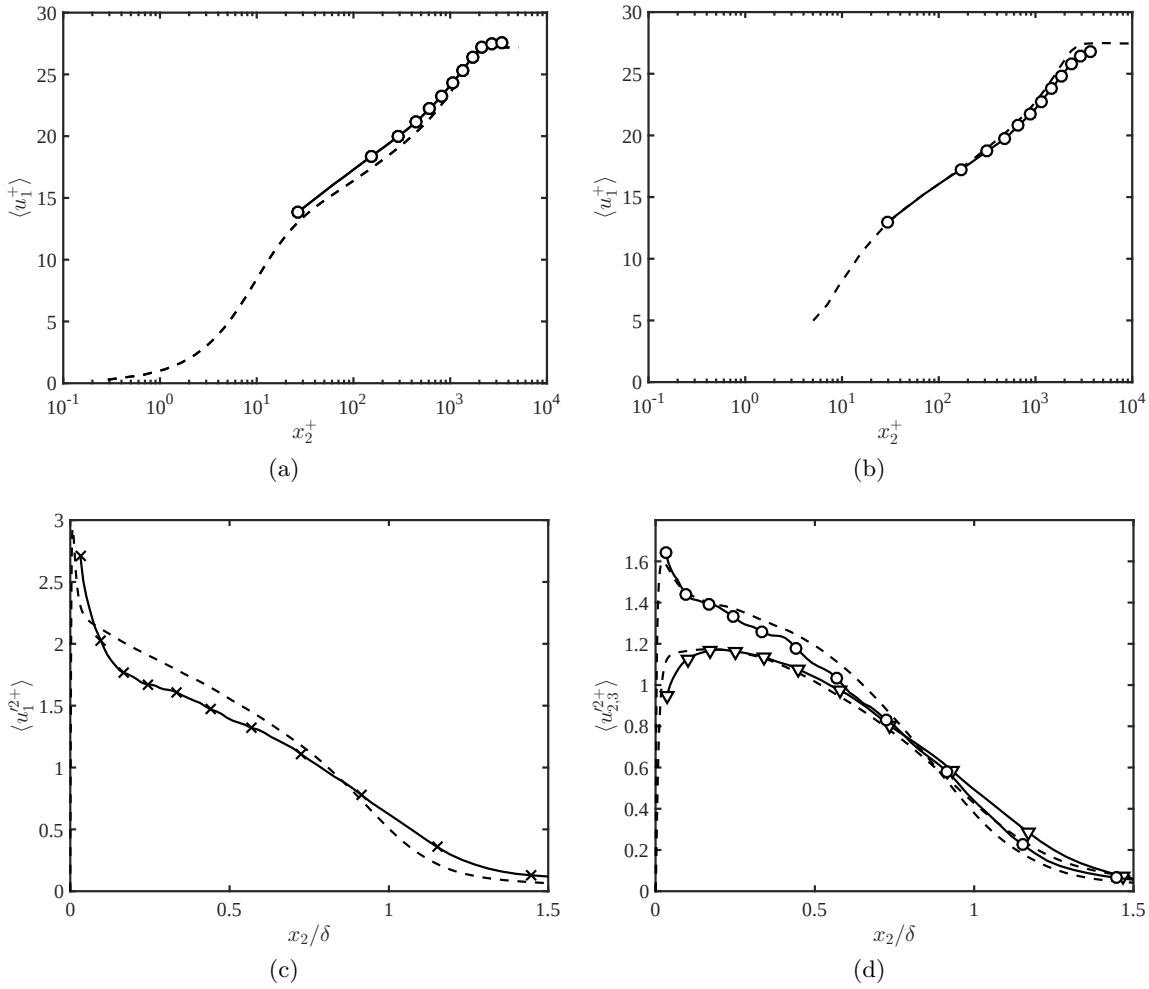

Figure 4.23: Mean streamwise velocity profile for (a) $Re_\theta \approx 6500$ and (b) $Re_\theta \approx 8000$, and the rms (c) streamwise ($\times$), (d) spanwise ($\bigcirc$), and wall-normal ($\bigtriangledown$) fluctuation profiles at $Re_\theta \approx 6500$. WSIM (symbols) and DNS [141] or experiment [111] (- - - -).

respectively. In this study, we have investigated the efficacy of the Robin (slip) boundary condition, where the velocities at the wall are characterized by the slip lengths and slip velocities. One novel aspect of this boundary condition is the non-zero instantaneous wall-normal velocity at the wall, i.e., transpiration, that opens a new avenue to model near-wall turbulence in LES. We have also presented a new dynamic slip wall model, WSIM, that is free from *a priori* tunable RANS parameters, which most traditional wall models for LES rely on. The model is based on the invariance of the wall stress under test filtering and is effectively applied through the slip boundary condition.

We have provided theoretical support for the use of the slip condition in wall-modeled LES instead of the widely applied Neumann boundary condition with no-transpiration. *A priori* testing was performed to assess the validity of the slip condition in the context of filtered DNS data.

The slip boundary condition was implemented in LES of channel flow in order to gain a better insight into its capabilities and shortcomings. One of the key properties, made possible by transpiration, is that the correct wall stress can always be achieved by an appropriate combination of slip lengths. This property is crucial when the grid resolution in the near-wall region does not capture the buffer and logarithmic layer dynamics, which may result in an under- or over-prediction of the wall stress. We have derived the consistency conditions for coupling the wall stress with the slip boundary condition in channel flows and flat-plate boundary layers and showed that such constraints are sufficient to guarantee the correct wall stress. Another advantage emanates from the non-zero Reynolds stress at the wall. This is not only consistent with the filtered velocity fields but also alleviates the well-known problem of wall-stress under-estimation by commonly used SGS models. We have also assessed the sensitivities of one-point statistics to grid refinements, changes in Re_τ, and different SGS models. The role of imposing zero mean mass flow through the wall by proper calculation of the slip parameters has also been shown to be a key component of the model.

Finally, we have tested the performance of WSIM in a plane turbulent channel flow at various Reynolds numbers and grid resolutions. WSIM was able to correctly capture

the overall behavior of the optimal slip length for a wide range of grid resolutions and Reynolds numbers. The results have been compared with those from the EQWM and the no-slip boundary condition. In all cases, WSIM performed substantially better than the no-slip, and the predictive error in the mean velocity profile was found to be below 10% for $Re_\tau < 20{,}000$ and all grid resolutions investigated. The model was also tested for a three-dimensional transient channel flow, where the performance was similar to that of the EQWM, and for a zero-pressure-gradient flat-plate turbulent boundary layer at Re_θ up to 10,000, where the error in the friction coefficient was less than 4%. However, due to the sensitivity of the model to SGS models and numerical filtering operations, additional advancements are required to formulate a robust dynamic wall model that is consistent with different numerical methods and SGS models.

Chapter 5

Concluding remarks

For large-eddy simulation (LES) to be used as a predictive tool in practical applications, accurate and efficient subgrid-scale (SGS) models are required. Once an SGS model is developed, rigorous procedures to assess the performance of the proposed SGS model are essential. Finally, for the near-wall region of turbulent boundary layers, where SGS models are known to under-perform, effective wall models that compensate for the missing stresses are necessary. This work attempts to address the three necessary requirements for practical use of LES highlighted here.

First, an SGS model based on first principles to remove the pile-up of energy in the smallest resolved scales has been formulated, implemented and validated in various flow configurations. The anisotropic minimum-dissipation (AMD) model dynamically estimates the required eddy viscosity without the need of test-filtering, which reduces the computational cost compared to the widely used dynamic Smagorinsky model (DSM). It is evaluated locally without the need for averaging in the homogeneous directions, which has practical advantages over the DSM for complex geometries. The AMD model is parameter-free, as the Poincaré constant is a physical constant with only modifications necessary depending on the discretization of the Navier-Stokes equations. A new method of computing the Poincaré constant for different numerical discretizations have been introduced. The AMD model was validated in decaying isotropic turbulence, turbulent mixing layer, and turbulent channel

flow. The SGS model was extended to scalar transport equations, and the scalar model was tested in a high-Reynolds number rough-wall boundary layer.

Secondly, two benchmark cases to assess the performance of SGS models in high-Reynolds-number wall-bounded flows without the additional burden of resolving the near-wall region have been introduced: the slip-wall and the exact-wall-stress channel flow. The proposed cases bypass the viscous effects by either supplying the correct mean wall stress or applying a permeable wall to damp the viscous effects. This allows the SGS models to be tested in the outer-region of wall-bounded flows without the grid refinement in all three spatial dimensions, which is required for wall-resolved LES. The proposed model problems provide good platforms to test SGS models away from the wall. The theoretical and numerical error convergence for the mean velocity profile, turbulence intensities, and spectra are given. The relevant length scale to measure LES performance has also been proposed. The results highlighted show that existing SGS models such as the AMD model proposed in Chapter 2 or the DSM perform well in the outer-region.

Finally, a dynamic slip wall model based on the invariance of wall stress under test filtering has been proposed. The efficacy of the slip boundary condition was first examined using theoretical arguments and *a priori* study using direct numerical simulation (DNS) data. The effect of the slip boundary condition on one-point statistics was studied using LES of channel flow. A compatibility condition for the slip boundary condition to recover the correct wall stress was derived. We also show that the over-prediction of streamwise turbulence intensities that is prevalent in under-resolved LES can be alleviated using the slip boundary condition. The dynamic slip wall model is then tested in different flow configurations, for a wide range of Reynolds numbers, and with various grid resolutions. Predictions of the mean velocity profile and turbulence intensities are in good agreement with DNS and experimental data at moderate Reynolds numbers.

Bibliography

[1] M. Abkar, H. J. Bae, and P. Moin. Minimum-dissipation scalar transport model for large-eddy simulation of turbulent flows. *Phys. Rev. Fluids*, 1(4):041701, 2016.

[2] W. Anderson and C. Meneveau. Dynamic roughness model for large-eddy simulation of turbulent flow over multiscale, fractal-like rough surfaces. *J. Fluid Mech.*, 679: 288–314, 2011.

[3] A. Andren, A. R. Brown, P. J. Mason, J. Graf, U. Schumann, C.-H. Moeng, and F. T. M. Nieuwstadt. Large-eddy simulation of a neutrally stratified boundary layer: A comparison of four computer codes. *Q. J. Royal Meteorol. Soc.*, 120(520):1457–1484, 1994.

[4] R. A. Antonia, L. Fulachier, L. V. Krishnamoorthy, T. Benabid, and F. Anselmet. Influence of wall suction on the organized motion in a turbulent boundary layer. *J. Fluid Mech.*, 190:217–240, 1988.

[5] M. Antonopoulos-Domis. Large-eddy simulation of a passive scalar in isotropic turbulence. *J. Fluid Mech.*, 104:55–79, 1981.

[6] H. J. Bae, A. Lozano-Durán, S. T. Bose, and P. Moin. Turbulence intensities in large-eddy simulation of wall-bounded flows. *Phys. Rev. Fluids*, 3:014610, 2018.

[7] H. J. Bae, A. Lozano-Durán, S. T. Bose, and P. Moin. Dynamic slip wall model for large-eddy simulation. *J. Fluid Mech.*, submitted, 2018.

[8] J. S. Baggett. On the feasibility of merging LES with RANS for the near-wall region of attached turbulent flows. In *Annual Research Briefs*, pages 267–277. Center for Turbulence Research, Stanford University, 1998.

[9] O. M. Bakken, P. Å. Krogstad, A. Ashrafian, and H. I. Andersson. Reynolds number effects in the outer layer of the turbulent flow in a channel with rough walls. *Phys. Fluids*, 17(6):065101, 2005.

[10] E. Balaras, C. Benocci, and U. Piomelli. Two-layer approximate boundary conditions for large-eddy simulations. *AIAA J.*, 34(6):1111–1119, 1996.

[11] J. Bonnet, R. Moser, and W. Rodi. A selection of test cases for the validation of large eddy simulations of turbulent flows. *AGARD advisory report*, 345:1–35, 1998.

[12] S. T. Bose. *Explicitly filtered large-eddy simulation: with application to grid adaptation and wall modeling.* PhD thesis, Stanford University, 2012.

[13] S. T. Bose and P. Moin. A dynamic slip boundary condition for wall-modeled large-eddy simulation. *Phys. Fluids*, 26(1):015104, 2014.

[14] S. T. Bose and G. I. Park. Wall-modeled les for complex turbulent flows. *Ann. Rev. Fluid Mech.*, 50(1):535–561, 2018.

[15] S. T. Bose, P. Moin, and D. You. Grid-independent large-eddy simulation using explicit filtering. *Phys. Fluids*, 22(10):105103, 2010.

[16] E. Bou-Zeid, C. Meneveau, and M. B. Parlange. Large-eddy simulation of neutral atmospheric boundary layer flow over heterogeneous surfaces: Blending height and effective surface roughness. *Water Resour. Res.*, 40(2), 2004.

[17] E. Bou-Zeid, C. Meneveau, and M. Parlange. A scale-dependent lagrangian dynamic model for large eddy simulation of complex turbulent flows. *Phys. Fluids*, 17(2): 025105, 2005.

[18] J. A. Businger, J. C Wyngaard, Y. Izumi, and E. F. Bradley. Flux-profile relationships in the atmospheric surface layer. *J. Atmos. Sci.*, 28(2):181–189, 1971.

[19] W. H. Cabot and P. Moin. Approximate wall boundary conditions in the large-eddy simulation of high Reynolds number flow. *Flow Turbul. Combust.*, 63:269–291, 2000.

[20] M. Calaf, M. B. Parlange, and C. Meneveau. Large eddy simulation study of scalar transport in fully developed wind-turbine array boundary layers. *Phys. Fluids*, 23 (12):126603, 2011.

[21] C. Canuto, M. Y. Hussaini, A. Quarteroni, and A. Thomas Jr. *Spectral methods in fluid dynamics*. Springer Science & Business Media, 2012.

[22] D. Carati, G. S. Winckelmans, and H. Jeanmart. On the modelling of the subgrid-scale and filtered-scale stress tensors in large-eddy simulation. *J. Fluid Mech.*, 441: 119–138, 2001.

[23] I. Celik, M. Klein, and J. Janicka. Assessment measures for engineering les applications. *J. Fluids Eng.*, 131(3):031102–031102–10, 2009.

[24] D. Chandran, R. Baidya, J. P. Monty, and I. Marusic. Two-dimensional energy spectra in high-reynolds-number turbulent boundary layers. *J. Fluid Mech.*, 826:R1, 2017.

[25] D. R. Chapman. Computational aerodynamics development and outlook. *AIAA J.*, 17(12):1293–1313, 1979.

[26] H. Choi and P. Moin. Grid-point requirements for large eddy simulation: Chapman's estimates revisited. *Phys. Fluids*, 24(1):011702, 2012.

[27] F. K. Chow and P. Moin. A further study of numerical errors in large-eddy simulations. *J. Comp. Phys.*, 184(2):366–380, 2003.

[28] D. Chung and B. J. McKeon. Large-eddy simulation of large-scale structures in long channel flow. *J. Fluid Mech.*, 661:341–364, 2010.

[29] D. Chung and D. I. Pullin. Large-eddy simulation and wall modelling of turbulent channel flow. *J. Fluid Mech.*, 631:281–309, 2009.

[30] D. Chung, J. P. Monty, and A. Ooi. An idealised assessment of townsends outer-layer similarity hypothesis for wall turbulence. *J. Fluid Mech.*, 742, 2014.

[31] Y. M. Chung and H. J. Sung. Initial relaxation of spatially evolving turbulent channel flow with blowing and suction. *AIAA J.*, 39(11):2091–2099, 2001.

[32] R. A. Clark, J. H. Ferziger, and W. C. Reynolds. Evaluation of subgrid-scale models using an accurately simulated turbulent flow. *J. Fluid Mech.*, 91:1–16, 1979.

[33] G. Comte-Bellot and S. Corrsin. Simple Eulerian time correlation of full- and narrow-band velocity signals in grid-generated, 'isotropic' turbulence. *J. Fluid Mech.*, 48(2): 273–337, 1971.

[34] J. W. Deardorff. A numerical study of three-dimensional turbulent channel flow at large Reynolds numbers. *J. Fluid Mech.*, 41(1970):453–480, 1970.

[35] J. W. Deardorff. On the magnitude of the subgrid scale eddy coefficient. *J. Comp. Phys.*, 7(1):120–133, 1971.

[36] J. C. Del Álamo, J. Jiménez, P. Zandonade, and R. D. Moser. Scaling of the energy spectra of turbulent channels. *J. Fluid Mech.*, 500:135–144, 2004.

[37] J. C. Del Álamo, J. Jiménez, P. Zandonade, and R. D. Moser. Self-similar vortex clusters in the turbulent logarithmic region. *J. Fluid Mech.*, 561:329–358, 2006.

[38] S. Dong, A. Lozano-Durán, A. Sekimoto, and J. Jiménez. Coherent structures in homogeneous shear turbulence compared with those in channels. *J. Fluid Mech.*, 816: 167–208, 2017.

[39] O. Flores and J. Jiménez. Effect of wall-boundary disturbances on turbulent channel flows. *J. Fluid Mech.*, 566:357–376, 2006.

[40] O. Flores, J. Jiménez, and J. C. del Álamo. Vorticity organization in the outer layer of turbulent channels with disturbed walls. *J. Fluid Mech.*, 591:145–154, 2007.

[41] M. Freitag and M. Klein. An improved method to assess the quality of large eddy simulations in the context of implicit filtering. *J. Turbul.*, 7:N40, 2006.

[42] M. Germano, U. Piomelli, P. Moin, and W. H. Cabot. A dynamic subgrid-scale eddy viscosity model. *Phys. Fluids A*, 3(7):1760, 1991.

[43] B. J. Geurts and J. Fröhlich. A framework for predicting accuracy limitations in large-eddy simulation. *Phys. Fluids*, 14(6):L41–L44, 2002.

[44] S. Ghosal. An analysis of numerical errors in large-eddy simulations of turbulence. *J. Comp. Phys.*, 125(1):187–206, 1996.

[45] S. Ghosal and P. Moin. The basic equations for the large eddy simulation of turbulent flows in complex geometry. *J. Comp. Phys.*, 118(1):24 – 37, 1995.

[46] S. Ghosal and M. M. Rogers. A numerical study of self-similarity in a turbulent plane wake using large-eddy simulation. *Phys. Fluids*, 9:1729–1739, 1997.

[47] B. M. Giometto, A. Lozano-Durán, G. I. Park, and P. Moin. Three-dimensional transient channel flow at moderate Reynolds numbers: analysis and wall modeling. In *Annual Research Briefs*, pages 193–205. Center for Turbulence Research, Stanford University, 2017.

[48] S. Hoyas and J. Jiménez. Scaling of the velocity fluctuations in turbulent channels up to Re_τ =2003. *Phys. Fluids*, 18(1):011702, 2006.

[49] M. Hultmark, M. Vallikivi, S. C. C. Bailey, and A. J. Smits. Turbulent pipe flow at extreme reynolds numbers. *Phys. Rev. Lett.*, 108:094501, 2012.

[50] J. Jiménez. Turbulent flows over rough walls. *Ann. Rev. Fluid Mech.*, 36(1):173–196, 2004.

[51] J. Jiménez. Cascades in wall-bounded turbulence. *Ann. Rev. Fluid Mech.*, 44, 2012.

[52] J. Jiménez. Near-wall turbulence. *Phys. Fluids*, 25(10):101302, 2013.

[53] J. Jiménez and S. Hoyas. Turbulent fluctuations above the buffer layer of wall-bounded flows. *J. Fluid Mech.*, 611:215–236, 2008.

[54] J. Jiménez and R. D. Moser. Large-eddy simulations: Where are we and what can we expect? *AIAA J.*, 38(4):605–612, 2000.

[55] J. Jiménez and A. Pinelli. The autonomous cycle of near-wall turbulence. *J. Fluid Mech.*, 389:335–359, 1999.

[56] J. Jiménez, S. Hoyas, M. P. Simens, and Y. Mizuno. Turbulent boundary layers and channels at moderate reynolds numbers. *J. Fluid Mech.*, 657:335–360, 2010.

[57] B. A. Kader and A. M. Yaglom. Spectra and correlation functions of surface layer atmospheric turbulence in unstable thermal stratification. In *Turbulence and Coherent Structures*, pages 387–412. Springer, 1991.

[58] H. S. Kang, S. Chester, and C. Meneveau. Decaying turbulence in an active-grid-generated flow and comparisons with large-eddy simulation. *J. Fluid Mech.*, 480: 129–160, 2003.

[59] G. G. Katul, C. R. Chu, M. B. Parlange, J. D. Albertson, and T. A. Ortenburger. Low-wavenumber spectral characteristics of velocity and temperature in the atmospheric surface layer. *J. Geophys. Res.: Atmos.*, 100(D7):14243–14255, 1995.

[60] S. Kawai and J. Larsson. Wall-modeling in large eddy simulation: Length scales, grid resolution, and accuracy. *Phys. Fluids*, 24(1):015105, 2012.

[61] S. Kawai and J. Larsson. Dynamic non-equilibrium wall-modeling for large eddy simulation at high reynolds numbers. *Phys. Fluids*, 25(1):015105, 2013.

[62] J. Kim and P. Moin. Application of a fractional-step method to incompressible Navier-Stokes equations. *J. Comp. Phys.*, 59:308–323, 1985.

[63] M. Klein. An attempt to assess the quality of large eddy simulations in the context of implicit filtering. *Flow Turb. Comb.*, 75(1):131–147, 2005.

[64] S. J. Kline, W. C. Reynolds, F. A. Schraub, and P. W. Runstadler. The structure of turbulent boundary layers. *J. Fluid Mech.*, 30(4):741–773, 1967.

[65] H. Kobayashi and Y. Shimomura. The performance of dynamic subgrid-scale models in the large eddy simulation of rotating homogeneous turbulence. *Phys. Fluids*, 13 (8):2350–2360, 2001.

[66] J. C. Kok. A high-order low-dispersion symmetry-preserving finite-volume method for compressible flow on curvilinear grids. *J. Comput. Phys.*, 228(18):6811–6832, 2009.

[67] A. N. Kolmogorov. The Local Structure of Turbulence in Incompressible Viscous Fluid for Very Large Reynolds' Numbers. In *Dokl. Akad. Nauk SSSR*, volume 30, pages 301–305, 1941.

[68] R. H. Kraichnan. The structure of isotropic turbulence at very high reynolds numbers. *J. Fluid Mech.*, 5(4):497–543, 1959.

[69] A. G. Kravchenko and P. Moin. On the effect of numerical errors in large eddy simulations of turbulent flows. *J. Comp. Phys.*, 131(2):310–322, 1997.

[70] A. G. Kravchenko, P. Moin, and K. Shariff. B-spline method and zonal grids for simulations of complex turbulent flows. *J. Comp. Phys.*, 151(2):757–789, 1999.

[71] J. Larsson, S. Kawai, J. Bodart, and I. Bermejo-Moreno. Large eddy simulation with modeled wall-stress: recent progress and future directions. *Mech. Eng. Rev.*, 3(1): 15–00418, 2016.

[72] J. Lee, M. Cho, and H. Choi. Large eddy simulations of turbulent channel and boundary layer flows at high reynolds number with mean wall shear stress boundary condition. *Phys. Fluids*, 25(11):110808, 2013.

[73] M. Lee and R. D. Moser. Direct numerical simulation of turbulent channel flow up to $Re_\tau \approx 5200$. *J. Fluid Mech.*, 774:395–415, 2015.

[74] O. Lehmkuhl, G. I. Park, and P. Moin. LES of flow over the NASA Common Research Model with near-wall modeling. In *Proceedings of the Summer Program*, pages 335–341. Center for Turbulence Research, Stanford University, 2016.

[75] O. Lehmkuhl, G. I. Park, and P. Moin. Wall-modeled large-eddy simulation of massively separated aircraft wake. In *Proceedings of the Summer Program*. Center for Turbulence Research, Stanford University, 2018 in press.

[76] A. Leonard. Energy cascade in large-eddy simulations of turbulent fluid flows. *Adv. Geophys.*, 18:237–248, 1975.

[77] D. K. Lilly. A proposed modification of the Germano subgrid-scale closure method. *Phys. Fluids A*, 4(3):633–635, 1992.

[78] A. Lozano-Durán and H. J. Bae. Convergence of large-eddy simulation in the outer region of wall-bounded turbulence. *Center for Turbulence Research - Annual Research Briefs*, pages 257–270.

[79] A. Lozano-Durán and H. J. Bae. Error scaling of large-eddy simulation in the outer region of wall-bounded turbulence. *J. Comp. Phys.*, submitted, 2018.

[80] A. Lozano-Durán and J. Jiménez. Effect of the computational domain on direct simulations of turbulent channels up to $Re_\tau = 4200$. *Phys. Fluids*, 26(1):011702, 2014.

[81] A. Lozano-Durán and J. Jiménez. Time-resolved evolution of coherent structures in turbulent channels: characterization of eddies and cascades. *J. Fluid Mech.*, 759: 432–471, 2014.

[82] H. Lu and F. Porté-Agel. A modulated gradient model for scalar transport in large-eddy simulation of the atmospheric boundary layer. *Phys. Fluids*, 25(1):015110, 2013.

[83] P. Luchini. Universality of the turbulent velocity profile. *Phys. Rev. Lett.*, 118:224501, 2017.

[84] T. S. Lund. The use of explicit filters in large eddy simulation. *Comput. Math. App.*, 46(4):603–616, 2003.

[85] T. S. Lund and H. J. Kaltenbach. Experiments with explicit filtering for les using a finite-difference method. In *Annual Research Briefs*, pages 91–105. Center for Turbulence Research, Stanford University, 1995.

[86] T. S. Lund, X. Wu, and K. D. Squires. Generation of turbulent inflow data for spatially-developing boundary layer simulations. *J. Comp. Phys.*, 140(2):233–258, 1998.

[87] N. N. Mansour, P. Moin, W. C. Reynolds, and J. H. Ferziger. Improved methods for large eddy simulations of turbulence. In *Turbulent Shear Flows 1*, pages 386–401. Springer-Verlag, 1979.

[88] A. L. Marsden, O. V. Vasilyev, and P. Moin. Construction of commutative filters for les on unstructured meshes. *J. Comp. Phys.*, 175(2):584–603, 2002.

[89] I. Marusic, J. P. Monty, M. Hultmark, and A. J. Smits. On the logarithmic region in wall turbulence. *J. Fluid Mech.*, 716:R3, 2013.

[90] P. J. Mason and D. J. Thomson. Stochastic backscatter in large-eddy simulations of boundary layers. *J. Fluid Mech.*, 242:51–78, 1992.

[91] O. J. McMillan and J. H. Ferziger. Direct testing of subgrid-scale models. *AIAA J.*, 17(12):1340–1346, 1979.

[92] C. Meneveau and J. Katz. Scale-invariance and turbulence models for large-eddy simulation. *Ann. Rev. Fluid Mech.*, 32:1–32, 2000.

[93] C. Meneveau and T. S. Lund. The dynamic smagorinsky model and scale-dependent coefficients in the viscous range of turbulence. *Phys. Fluids*, 9:3932–3934, 1997.

[94] O. Métais and M. Lesieur. Spectral large-eddy simulation of isotropic and stably stratified turbulence. *J. Fluid Mech.*, 239:157–194, 1992.

[95] J. Meyers. Error-landscape assessment of large-eddy simulations: A review of the methodology. *J. Sci. Comp.*, 49(1):65–77, 2011.

[96] J. Meyers and P. Sagaut. Is plane-channel flow a friendly case for the testing of large-eddy simulation subgrid-scale models? *Phys. Fluids*, 19(4):048105, 2007.

[97] J. Meyers, B. J. Geurts, and M. Baelmans. Database analysis of errors in large-eddy simulation. *Phys. Fluids*, 15(9):2740–2755, 2003.

[98] J. Meyers, B. J. Geurts, and P. Sagaut. A computational error-assessment of central finite-volume discretizations in large-eddy simulation using a smagorinsky model. *J. Comp. Phys.*, 227(1):156 – 173, 2007.

[99] C. M. Millikan. A critical discussion of turbulent flows in channels and circular tubes. In *Proceedings of the Fifth International Congress for Applied Mathematics, Harvard and MIT*, 1938.

[100] Y. Mizuno. Spectra of energy transport in turbulent channel flows for moderate Reynolds numbers. *J. Fluid Mech.*, 805:171–187, 2016.

[101] Y. Mizuno and J. Jiménez. Mean velocity and length-scales in the overlap region of wall-bounded turbulent flows. *Phys. Fluids*, 23(8):085112, 2011.

[102] Y. Mizuno and J. Jiménez. Wall turbulence without walls. *J. Fluid Mech.*, 723: 429–455, 2013.

[103] C.-H. Moeng. A large-eddy-simulation model for the study of planetary boundary-layer turbulence. *J. Atmos. Sci.*, 41(13):2052–2062, 1984.

[104] P. Moin and J. Kim. Numerical investigation of turbulent channel flow. *J. Fluid Mech.*, 118:341–377, 1982.

[105] P. Moin, T. H. Shih, D. Driver, and N. N. Mansour. Direct numerical simulation of a threedimensional turbulent boundary layer. *Phys. Fluids A*, 2(10):1846–1853, 1990.

[106] P. Moin, K. Squires, W. Cabot, and S. Lee. A dynamic subgrid-scale model for compressible turbulence and scalar transport. *Phys. Fluids A*, 3(11):2746–2757, 1991.

[107] G. Nastac, J. W. Labahn, L. Magri, and M. Ihme. Lyapunov exponent as a metric for assessing the dynamic content and predictability of large-eddy simulations. *Phys. Rev. Fluids*, 2:094606, 2017.

[108] F. Nicoud, H. B. Toda, O. Cabrit, S. T. Bose, and J. Lee. Using singular values to build a subgrid-scale model for large eddy simulations. *Phys. Fluids*, 23:085106, 2011.

[109] N. Nikitin. Spatial periodicity of spatially evolving turbulent flow caused by inflow boundary condition. *Phys. Fluids*, 19(9):091703, 2007.

[110] P. Orlandi. *Fluid Flow Phenomena: A Numerical Toolkit*. Springer, 2000.

[111] J. M. Österlund. *Experimental studies of zero pressure-gradient turbulent boundary layer flow*. PhD thesis, Mekanik, 1999.

[112] R. L. Panton. Overview of the self-sustaining mechanisms of wall turbulence. *Prog. Aerosp. Sci.*, 37(4):341–383, 2001.

[113] G. I. Park and P. Moin. An improved dynamic non-equilibrium wall-model for large eddy simulation. *Phys. Fluids*, 26(1):015108, 2014.

[114] L. L. Pauley, P. Moin, and W. C. Reynolds. The structure of two-dimensional separation. *J. Fluid Mech.*, 220:397–411, 1990.

[115] L. Payne and H. F. Weinberger. An optimal poincaré inequality for convex domains. *Arch. Ration. Mech. Anal.*, 5:286–292, 1960.

[116] B. Perot and P. Moin. Shear-free turbulent boundary layers. Part 1. Physical insights into near-wall turbulence. *J. Fluid Mech.*, 295:199227, 1995.

[117] A. E. Perry and C. J. Abell. Asymptotic similarity of turbulence structures in smooth and rough-walled pipes. *J. Fluid Mech.*, 79:785 – 799, 1977.

[118] A. E. Perry, S. Henbest, and M. S. Chong. A theoretical and experimental study of wall turbulence. *J. Fluid Mech.*, 165:163–199, 1986.

[119] U. Piomelli. High reynolds number calculations using the dynamic subgridscale stress model. *Phys. Fluids A*, 5(6):1484–1490, 1973.

[120] U. Piomelli and E. Balaras. Wall-layer models for large-eddy simulations. *Annu. Rev. Fluid Mech.*, 34:349–374, 2002.

[121] U. Piomelli and T. A. Zang. Large-eddy simulation of transitional channel flow. *Comput. Phys. Commun.*, 65(1-3):224–230, 1991.

[122] U. Piomelli, P. Moin, and J. H. Ferziger. Model consistency in large eddy simulation of turbulent channel flows. *Phys. fluids*, 31(7):1884–1891, 1988.

[123] U. Piomelli, J. Ferziger, P. Moin, and J. Kim. New approximate boundary conditions for large eddy simulations of wall-bounded flows. *Phys. Fluids A*, 1(6):1061–1068, 1989.

[124] U. Piomelli, E. Balaras, H. Pasinato, K. D. Squires, and P. R. Spalart. The inner–outer layer interface in large-eddy simulations with wall-layer models. *Int. J. Heat and Fluid Flow*, 24(4):538–550, 2003.

[125] S. B. Pope. *Turbulent Flows*. Cambridge Univ Press, 2000.

[126] S. B. Pope. Ten questions concerning the large-eddy simulation of turbulent flows. *New J. Phys.*, 6(1):35, 2004.

[127] F. Porté-Agel. A scale-dependent dynamic model for scalar transport in large-eddy simulations of the atmospheric boundary layer. *Bound.-Layer Meteorol.*, 112(1):81–105, 2004.

[128] F. Porté-Agel, C. Meneveau, and M. B. Parlange. A scale-dependent dynamic model for large-eddy simulation: application to a neutral atmospheric boundary layer. *J. Fluid Mech.*, 415:261–284, 2000.

[129] L. Prandtl. Bericht über Untersuchungen zur ausgebildeten Turbulenz. *Z. Angew. Math. Mech.*, 5:136–139, 1925.

[130] A. Rasam, G. Brethouwer, P. Schlatter, Q. Li, and A. V. Johansson. Effects of modelling, resolution and anisotropy of subgrid-scales on large eddy simulations of channel flow. *J. Turbul.*, 12(10):1–20, 2011.

[131] S. K. Robinson. Coherent motions in the turbulent boundary layer. *Ann. Rev. Fluid Mech.*, 23(1):601–639, 1991.

[132] R. S. Rogallo and P. Moin. Numerical simulation of turbulent flows. *Ann. Rev. Fluid Mech.*, 16(1):99–137, 1984.

[133] M. M. Rogers and R. D. Moser. Direct simulation of a self-similar turbulent mixing layer. *Phys. Fluids*, 6:903–923, 1994.

[134] W. Rozema. *Low-dissipation methods and models for the simulation of turbulent subsonic flow: Theory and applications*. PhD thesis, University of Groningen, 2015.

[135] W. Rozema, J. C. Kok, R. W. C. P. Verstappen, and A. E. P. Veldman. A symmetry-preserving discretisation and regularisation model for compressible flow with application to turbulent channel flow. *J. Turbul.*, 15(6):386–410, 2014.

[136] W. Rozema, H. J. Bae, P. Moin, and R. W. C. P. Verstappen. Minimum-dissipation models for large-eddy simulation. *Phys. Fluids*, 27(8):085107, 2015.

[137] S. G. Saddoughi and S. V. Veeravalli. Local isotropy in turbulent boundary layers at high reynolds number. *J. Fluid Mech.*, 268:333–372, 1994.

[138] P. Schlatter and R. Örlü. Assessment of direct numerical simulation data of turbulent boundary layers. *J. Fluid Mech.*, 659:116, 2010.

[139] U. Schumann. Subgrid scale model for finite difference simulations of turbulent flows in plane channels and annuli. *J. Comp. Phys.*, 18:376–404, 1975.

[140] A. Scotti, C. Meneveau, and D. K. Lilly. Generalized smagorinsky model for anisotropic grids. *Phys. Fluids*, 5(9):2306–2308, 1993.

[141] J. A. Sillero, J. Jiménez, and R. D. Moser. One-point statistics for turbulent wall-bounded flows at reynolds numbers up to $\delta^+ \approx 2000$. *Phys. Fluids*, 25(10):105102, 2013.

[142] M. H. Silvis, F. X. Trias, M. Abkar, H. J. Bae, A. Lozano-Durán, and R. W. C. P. Verstappen. Exploring nonlinear subgrid-scale models and new characteristic length scales for large-eddy simulation. In *Proceedings of the Summer Program*, pages 265–274. Center for Turbulence Research, Stanford University, 2016.

[143] M. P. Simens, J. Jiménez, S. Hoyas, and Y. Mizuno. A high-resolution code for turbulent boundary layers. *J. Comp. Phys.*, 228(11):4218–4231, 2009.

[144] R. L. Simpson, R. J. Moffat, and W. M. Kays. The turbulent boundary layer on a porous plate: experimental skin friction with variable injection and suction. *Int. J. Heat Mass Tran.*, 12(7):771–789, 1969.

[145] J. Slotnick, A. Khodadoust, J. Alonso, D. Darmofal, W. Gropp, E. Lurie, and D. Mavriplis. *CFD Vision 2030 Study: A Path to Revolutionary Computational Aerosciences*. Tech. Rep. CR–2014-218178, NASA. 2014.

[146] J. Smagorinsky. General circulation experiments with the primitive equations. *Mon. Weather Rev.*, 91(3):99–164, 1963.

[147] P. R. Spalart. Strategies for turbulence modelling and simulations. *Int. J. Heat Fluid Fl.*, 21(3):252–263, 2000.

[148] P. R. Spalart. Detached-eddy simulation. *Annu. Rev. Fluid Mech.*, 41:181–202, 2009.

[149] P. R. Spalart, W. H. Jou, M. Strelets, and S. R. Allmaras. Comments on the feasibility of LES for wings, and on a hybrid RANS/LES approach. *Advances in DNS/LES*, 1: 4–8, 1997.

[150] K. R. Sreenivasan. The passive scalar spectrum and the obukhov–corrsin constant. *Phys. Fluids*, 8(1):189–196, 1996.

[151] R. J. A. M. Stevens, M. Wilczek, and C. Meneveau. Large-eddy simulation study of the logarithmic law for second- and higher-order moments in turbulent wall-bounded flow. *J. Fluid Mech.*, 757:888–907, 2014.

[152] Sir G. G. Stokes et al. *Mathematical and physical papers*. 1901.

[153] R. Stoll and F. Porté-Agel. Dynamic subgrid-scale models for momentum and scalar fluxes in large-eddy simulations of neutrally stratified atmospheric boundary layers over heterogeneous terrain. *Water Resour. Res.*, 42(1), 2006.

[154] R. B. Stull. *An introduction to boundary layer meteorology*, volume 13. Springer Science & Business Media, 2012.

[155] P. P. Sullivan and E. G. Patton. The effect of mesh resolution on convective boundary layer statistics and structures generated by large-eddy simulation. *J. Atmos. Sci.*, 68 (10):2395–2415, 2011.

[156] P. P. Sullivan, J. C. McWilliams, and C.-H. Moeng. A subgrid-scale model for large-eddy simulation of planetary boundary-layer flows. *Bound.-Layer Meteorol.*, 71(3): 247–276, 1994.

[157] P. P. Sullivan, J. C. McWilliams, and C.-H. Moeng. A grid nesting method for large-eddy simulation of planetary boundary-layer flows. *Bound.-Layer Meteorol.*, 80(1-2): 167–202, 1996.

[158] H. L. Tennekes and J. L. Lumley. *A First Course in Turbulence*. MIT Press, 1972.

[159] H. B. Toda, O. Cabrit, K. Truffin, G. Bruneaux, and F. Nicoud. Assessment of subgrid-scale models with a large-eddy simulation-dedicated experimental database: The pulsatile impinging jet in turbulent cross-flow. *Phys. Fluids*, 26(7):075108, 2014.

[160] A. A. Townsend. *The structure of turbulent shear flow*. Cambridge Univ Press, 1976.

[161] F. X. Trias, A. Gorobets, M. H. Silvis, R. W. C. P. Verstappen, and A. Oliva. A new subgrid characteristic length for turbulence simulations on anisotropic grids. *Phys. Fluids*, 29(11):115109, 2017.

[162] R. W. C. P. Verstappen. When does eddy viscosity damp subfilter scales sufficiently? *J. Sci. Comput.*, 49(1):94–110, 2011.

[163] R. W. C. P. Verstappen, S. T. Bose, J. Lee, H. Choi, and P. Moin. A dynamic eddy-viscosity model based on the invariants of the rate-of-strain. In *Proceedings of the Summer Program*, pages 183–192. Center for Turbulence Research, Stanford University, 2010.

[164] R. W. C. P. Verstappen, W. Rozema, and H. J. Bae. Numerical scale separation in large-eddy simulation. In *Proceedings of the Summer Program*, pages 417–426. Center for Turbulence Research, Stanford University, 2014.

[165] A. W. Vreman. *Direct and large-eddy simulation of the compressible turbulent mixing layer*. PhD thesis, Universiteit Twente, 1995.

[166] A. W. Vreman. An eddy-viscosity subgrid-scale model for turbulent shear flow: Algebraic theory and applications. *Phys. Fluids*, 16(10):3670–3681, 2004.

[167] B. Vreman, B. Geurts, and H. Kuerten. Large-eddy simulation of the temporal mixing layer using the clark model. *Theor. Comp. Fluid Dyn.*, 8(4):309–324, 1996.

[168] B. Vreman, B. Geurts, and H. Kuerten. Large-eddy simulation of the turbulent mixing layer. *J. Fluid Mech.*, 339:357–390, 1997.

[169] F. Waleffe, J. Kim, and J. M. Hamilton. On the origin of streaks in turbulent shear flows. In *Turbulent Shear Flows 8*, pages 37–49. Springer, 1993.

[170] M. J. Walsh. Riblets as a viscous drag reduction technique. *AIAA J.*, 21(4):485–486, 1983.

[171] M. Wang and P. Moin. Dynamic wall modeling for large-eddy simulation of complex turbulent flows. *Phys. Fluids*, 14(7):2043–2051, 2002.

[172] J. Weatheritt, R. Sandberg, and A. Lozano-Durán. Reynolds stress structures in the hybrid rans/les of a planar channel. *J. Phys.: Conf. Ser.*, 708(1):012008, 2016.

[173] F. M. White and I. Corfield. *Viscous fluid flow*, volume 3. McGraw-Hill New York, 2006.

[174] G. S. Winckelmans, A. A. Wray, O. V. Vasilyev, and H. Jeanmart. Explicit-filtering large-eddy simulation using the tensor-diffusivity model supplemented by a dynamic Smagorinsky term. *Phys. Fluids*, 13(5):1385–1403, 2001.

[175] G. S. Winckelmans, H. Jeanmart, and D. Carati. On the comparison of turbulence intensities from large-eddy simulation with those from experiment or direct numerical simulation. *Phys. Fluids*, 14(5):1809–1811, 2002.

[176] A. A. Wray. Minimal-storage time advancement schemes for spectral methods. Technical report, NASA Ames Research Center, 1990.

[177] Y. Yamamoto and Y. Tsuji. Numerical evidence of logarithmic regions in channel flow at $\mathrm{Re}_\tau = 8000$. *Phys. Rev. Fluids*, 3:012602, 2018.

[178] X. I. A. Yang, J. Sadique, R. Mittal, and C. Meneveau. Integral wall model for large eddy simulations of wall-bounded turbulent flows. *Phys. Fluids*, 27(2):025112, 2015.

[179] X. I. A. Yang, G. I. Park, and P. Moin. Log-layer mismatch and modeling of the fluctuating wall stress in wall-modeled large-eddy simulations. *Phys. Rev. Fluids*, 2: 104601, 2017.

[180] W. K. Yeo and K. W. Bedford. Closure-free turbulence modeling based upon a conjuctive higher order averaging procedure. *Computational Methods in Flow Analysis*, pages 844–851, 1988.

[181] S. Yoshioka and P. H. Alfredsson. *Control of turbulent boundary layers by uniform wall suction and blowing*, pages 437–442. Springer Netherlands, Dordrecht, 2006.